Politecnico di Torino

Master's degree thesis.
Master's Degree Program in
Civil Engineering

Thermal activation of tunnel infrastructures: insights from three Italian case studies

Franz Lester Servin Vega

Supervisor(s):
Prof. M. Barla Supervisor
Dr. A. Insana Co-Supervisor

Politecnico di Torino
October 21st, 2024

Abstract

Half of the energy consumption of the European Union is comprised by heating and cooling, which are largely dependent on energy fossil fuels. In contrast, renewable energies only represent 18% of the heating and cooling production. This Thesis focuses on the integration of energy geostructures, namely tunnels, as renewable sources for heating and cooling applications.

The research explores the concept of energy tunnels which are characterized by both thermal and structural behaviors and the harnessing of the ground temperature. In particular, the study addresses the thermal activation of tunnel linings, where heat exchanger pipes are embedded to capture and conduct the geothermal energy in an efficient way. The present Thesis provides an insight to the current state of the art, which involves several projects around the world such as the Turin Metro Line 1 and 2, the Lainzer tunnel in Vienna, the Stuttgart-Fasenhoff Tunnel, amongst others.

The Thesis focuses on the study of three different projects in Italy such as the Subport Tunnel in Genova, the Trento ring road tunnel and the Cortina d'Ampezzo tunnel. For each project, a brief description of the works is provided as well as their geotechnical, geothermal and hydrogeological frameworks. Based on the geothermal characterization of each site, homogeneous sections with similar geothermal properties along the chainage of the tunnels are identified with the purpose of estimating the total geothermal potential along the chainage. For this purpose, nomograms derived from the literature that provide the geothermal potential with respect to the ground temperature and the groundwater velocity are consulted.

Finally, the work includes the creation of the 3D finite element model for the case study of the Subport Tunnel of Genova. The model is created in the finite element software "Finite Element subsurface FLOW simulation system" (FEFLOW) in order to have a better understanding of the role of the seawater temperature on the evaluation of the geothermal potential. Following a sensitivity analysis, the outputs of the numerical model are thoroughly discussed and motivated.

Acknowledgment

As the conclusion of my master's degree approaches, I would like to acknowledge everyone who has given me their support throughout this journey.

In particular, I would like to thank my professors for allowing me to be their thesis student. Firstly, I want to thank Prof. Barla for his guidance, his mentorship, his availability, and his professionalism. In addition, I want to express my gratitude to Dr. Insana, for the knowledge she shared with me, her assistance and advice while working on the software, and her expertise. They have taught me to be the best version of myself in the field of the geotechnical engineering.

I want to thank God for giving me health, strength and the skills to fulfill this important chapter in my life. I would like to thank my parents, Franz and Laura, to whom I owe my life. Without their support, love and care I would not be the person I am today. To my sister, Hannia, thank you for always being by my side and for your love. I am extremely proud of the woman you are. In this special day I know we are thousands of kilometers away, but I keep you close in my heart always. To my godparents José Luis and Carmen, my aunt Lupe, my cousins Any, Karen, thank you for your support and for helping me pay for my flight to go to Mexico one year ago and see all of you. To my grandparents, Rosa, Héctor, Antonio and Leonides, I hope you are proud of your grandson wherever you are.

To my favorite person in this world, the woman I want to spend the rest of my life with, Ira: thank you for making me a better person, for always pushing my limits and for loving me. Not even the 38762 words in this Thesis are enough to say how much I love you. Thank you for always being by my side and I hope to share many more of these special moments and grow together in all aspects.

To my childhood and still best friends from Mexico, Angie, Jorge, Johan, Josué, Paco, Yan Carlo, Everardo, Diego, Luis Ángel thank you for your unconditional friendship and for all the moments we spent together growing up. To my best friends in Turin, namely Martín, Samuel, Enzo, Juliana, Manuel, Julián, Juanjo, Luciano, thank you for your support, kindness and for making these two years something unforgivable after all the laughs, tears, worries shared together. To the best flatmates, Ona, Ame, and Stiven thank you for the "chiacchiere", your kindness, and for your company.

Contents

List of Figures

List of Tables

Chapter 1

Introduction

1.1 Framework

Throughout the years, several renewable energies to supply heating and cooling to buildings and to the industry have been implemented. One of the main purposes is to reduce the reliance on fossil fuels while meeting the thermal needs of the aforementioned structures and thus, contribute to the sustainability of the planet and its decarbonization. Such renewable energies are namely the hydrothermal, aerothermal and geothermal energy, being the latter the focus of study of this thesis.

In this matter, all geotechnical structures can be modified to become energy geostructures. Absorber pipes are filled with a heat carrier fluid and are installed within conventional structural elements such as diaphragm walls, piles, walls or tunnel linings in order to exploit geothermal energy. The soil temperature is used as a heat source for heating in winter and as a heat sink for cooling in summer. One of the key features and advantages of the energy geostructures relies on the fact that no additional elements have to be installed below surface other than the absorber pipes.

The present Thesis explores the thermal activation of underground structures, specifically focusing on energy tunnels as innovative geotechnical solutions. In this research, the design, implementation and optimization of these energy geostructures to be used in civil engineering projects inside Italy, is discussed, where energy efficiency and environmental sustainability can be greatly improved through the use of such systems.

1.2 Problem statement

Integrated geothermal energy systems pose several technical and economic challenges. Even though energy tunnels offer promising advantages, such as reduced energy costs and lower environmental impact, their practical application demands a thorough consideration of several factors namely the thermal and structural properties of tunnel linings, the ground-structure interaction, and the economic feasibility of large-scale implementation.

In this Thesis, the focus is on maximizing energy efficiency in tunnels without compromising structural integrity through optimizing thermal activation in tunnel linings. In order to achieve this, advanced modeling techniques and the use of specific nomograms need to be employed to predict and enhance the performance of different projects, such as the Genoa, Trento, and Cortina tunnels.

Most of the research that has been conducted regarding energy tunnels has been focused on urban and mountainous environments, which are characteristic environments of the Trento and Cortina D'Ampezzo tunnels, respectively. Nevertheless, with respect to marine environments, as in the case of the Tunnel subportuale in Genova, there is little to non-existent available information related to the quantification of the geothermal energy along the chainage of the tunnel. Therefore, the present Thesis aims to set the foundations for the geothermal analysis of energy tunnels in marine conditions.

1.3 Thesis scope and objectives

As part of this Thesis, the feasibility and evaluation of geothermal energy in the selected case studies is carried out. Reference is made to the principal features of each project, such as their geotechnical, geothermal and hydrogeological frameworks derived from several technical reports.

The geothermal energy is quantified with the use of the nomograms proposed by the authors Barla and Insana (2020) for the three projects. In addition, a hydro-thermal analysis on a finite-element doftware was carried out for the tunnel located in Genova. A 3D finite element model was developed for comparison purposes with the results obtained with the nomograms.

Analysis and synthesis of the results obtained will allow to decide whether it is feasible to convert these three structures into energy geo-structures. Moreover, the

results and procedure described in the following chapters might work as a guideline for further similar studies.

1.4 Organization of thesis

The Thesis is divided into 5 chapters and one appendix. The present chapter gives an overview of the work carried out. *Chapter two* cites existing literature on geothermal energy, energy geostructures, and energy tunnels. A brief historical background of geothermal applications, the principles behind thermally activated structures, and the challenges associated with their implementation are discussed in this section.

Chapter three outlines detailed descriptions of the selected case studies: the Tunnel Subportuale in Genoa, Trento ring road tunnel, and Cortina D'Ampezzo tunnel. Each case study contains a general picture of the project, geotechnical characterization, and analysis of the geothermal and hydrogeological frameworks.

Chapter four is dedicated to the evaluation of the geothermal energy for each of the three case studies. Several asumptions and hypotheses made regarding the identification of the homogeneous sections and final calculations are listed in this section. In addition, numerical results derived from the nomograms are highlighted and illustrated.

Chapter five is devoted to the numerical simulation of the Genova case study. The procedure to build the finite element model of the tunnel is thoroughly described as well as the results obtained.

Chapter 2

State of the art

2.1 Introduction

The use of geothermal energy for heating and cooling in buildings and infrastructure is discussed in this chapter. The chapter focuses on covering two main topics: direct use of geothermal energy and energy geostructures centered on energy tunnels.

First, the historical use and the growth of geothermal energy in Italy for heating and cooling purposes is reviewed. Then, the chapter addresses the use of geotechnical structures, such as piles, diaphragm walls, basement slabs or walls, or tunnel linings and anchors in tunnels or in retaining structures, as energy geo-structures to exploit geothermal energy, with great economic and environmental benefit. The challenges in promoting the development of thermoactive geostructures are briefly mentioned in this chapter, such as demonstrating direct applicability and economic convenience, and the need for advanced numerical modelling and large-scale site experiments to reliably quantify the heat that can be exchanged with the ground.

In this context, the thermal activation of tunnel concrete linings, the design aspects to be considered and the integration with the district heating networks are tackled in this section. Additionally, examples of previous cases of study of energy tunnels are provided such as the Metro Line 1 and 2 of Torino, Lainzer tunnel in Vienna, Stuttgart-Fasanenhof Tunnel, Linchang Tunnel, and the Crossrail tunnels.

2.2 Geothermal energy

Heating and cooling consume half of the EU's energy and much of it is wasted. The lion's share of heating and cooling is still generated from fossil fuels, mainly natural gas, while only 18% is generated from renewable energy. In order to fulfil the EU's climate and energy goals, the heating and cooling sector must therefore sharply reduce its energy consumption and cut its use of fossil fuels (European

Union, 2016). In this context, aerothermal, geothermal and hydrothermal heat energy captured by heat pumps is established as one of the mainstream options to meet the thermal needs of buildings and industry for heating and cooling.

According to Lund & Boyd (2015), utilization of geothermal resources in Italy for direct application dates back to prehistoric times and developed intensively during the Roman Antiquity (3rd B.C.–5th A.D.). In this period of over 3000 years, the most intensive development of geothermal direct-use was for thermal balneology during the Roman period and from 1850 to 1920 for the exploitation of hydrothermal materials.

From 1950 through 2000, almost 325 MWt of direct uses were installed in Italy with spa use and thermal balneology as the major applications. After 2000, other direct uses, especially ground-source heat pumps, started to grow. Today, not considering geothermal heat pumps, space heating is the main direct-use application counting for about 42% of the energy use. This is followed by bathing and swimming at 33% and aqua culture at 17%. Heat pumps will continue to be the main growth for direct-use.

2.2 Energy geostructures

Shallow geothermal systems can play an important role in providing domestic heating and cooling, and their growth potential should be explored. Currently, closed- or open-loop systems are the most common applications. In the closed-loop borehole systems the heat exchange occurs between the ground and a heat carrier fluid flowing in the circuit installed in vertical or horizontal loops, whereas for the latter, the heat exchange takes place with the groundwater itself through extraction and reinjection wells (Barla & Insana, 2022). However, all geotechnical structures, such as piles, diaphragm walls, basement slabs or walls, or tunnel linings and anchors in tunnels or in retaining structures, can be instrumented to become energy geo-structures and exploit geothermal energy, with great economic and environmental benefit (Barla & Di Donna, 2016). They combine the role of the structural support with the role of the thermal energy carrier in a unique technology to serve all types of buildings and infrastructure (Alvi, Barla, & Insana, Thermal performance assessment of an energy lining for the Lyon-Turin base tunnel, 2022).

Absorber pipes filled with a heat carrier fluid are installed within conventional structural elements (piles, barrettes, diaphragm walls, basement slabs or walls, tunnel linings), forming the primary circuit of a geothermal energy system. The

natural ground temperature is used as a heat source for heating in winter and as a heat sink for cooling in summer. Hence no additional elements have to be installed below surface. The primary circuit is then connected via a heat pump to a secondary circuit within the building (Brandl, 2006).

Thermal activation of structural elements is done through the arrangement of a high-density polyethylene pipe closed loop where the heat carrier fluid circulates. The main advantage of this type of structures lies in the reduction of geothermal plant building costs as the concrete elements are already required for structural reasons, thus, no need for excavation or drillings. Additionally, it can be said that they are convenient because they are economical, the structural and energy needs are condensed into one single element, and the concrete is a material characterized by a good thermal conductivity and heat capacity (Barla & Insana, 2022).

On the other hand, the challenges that need to be faced to foster the development of thermoactive geostructures are still diverse. Demonstrating direct applicability and economic convenience is the key factor to promote the application of the technology to stakeholders and city planners. To this end, the ability to reliably quantify the heat that can be exchanged with the ground represents a key issue. This calls for the study of hydro–thermal interaction between the ground and the thermo-active structural elements by advanced numerical modelling as well as for large-scale site experiments. This is particularly relevant for those geostructures where limited experience is still available (almost all other than piles).

2.3 Energy tunnels

Energy tunnels are characterised by completely different structural features as well as by a markedly larger heat transfer potential compared to the current, most widely applied type of energy geostructures; energy piles. The first feature relates to the different shape and structural role that characterises tunnels compared to piles. The second feature is related to the wider surface that characterises tunnels compared to piles, and to the peculiarity of having an interface with air in the underground built environment in addition to the interface with the ground that entirely characterises energy piles. The presence of one interface between energy tunnels and air, and another interface with porous materials such as soil or rock, allows the harvesting of both aerothermal and shallow geothermal energies through this technology. This feature makes the energy exploitation achievable through energy tunnels particularly flexible yet challenging, because different heat sources can be employed but a multitude of coupled phenomena govern the thermo-

hydraulic behaviour and the energy performance of such technology (Cousin et al., 2019).

The heat exchanged by the lining with the surrounding ground has different purposes:

- heating and cooling of subway stations and substations (Bidarmaghz et al., 2023).
- buildings near the tunnel (Nicholson et al., 2014)
- heating the lining itself (Zhang et al., 2014)
- deicing of bridge decks, rails and routes strengthening both safety and durability (Islam et al., 2006; Baralis et al., 2020).

2.3.1 Thermal activation of a tunnel lining

By taking advantage of the nearly constant temperature of the ground up to approximately 50 m, the tunnel lining can be turned into a ground heat exchanger by including heat exchange pipes to form a close loop, as in standard low enthalpy geothermal applications such as vertical or horizontal borehole heat exchangers (BHE). The construction cost is significantly lower as no boreholes need to be drilled for this specific purpose. It is an interesting alternative to conventional shallow geothermal systems, especially in central, densely populated urban areas where possible end users are in the immediate vicinity and their heating and cooling demand can be easily met (Insana, 2020).

The system consists of a primary geothermal circuit, a secondary circuit and a water-source heat pump unit coupled with the ground heat exchangers collectors and/or a cooling machine (Figure 1). A heat carrier fluid (water, water with anti-freeze as glycol or saline solution that can work down to -20°C) is circulated by a hydraulic pump in the loop, extracting heat in winter (Insana, 2020). The warmed fluid is then further heated thanks to the heat pump to increase its energy level, typically from 10-15°C to 25-35°C as stated by Brandl (2006) and a distribution pipes network delivers the heat to the final users through the secondary circuit. In summer, excess heat is withdrawn from the building via air- or water-cooling systems embedded in floors, walls and ceilings and dissipated/stored into the soil via the absorber pipes. In this case the heat pump reduces fluid temperature below that in the conditioning system, thus improving reinjection effectiveness.

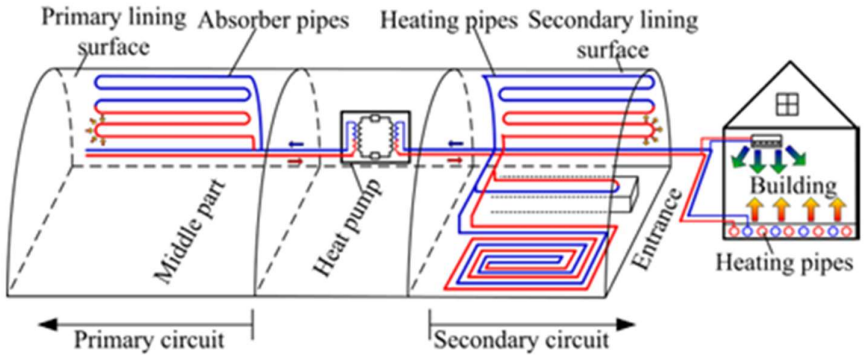

Figure 1. Basic work principle of tunnel linings GHEs (Zhang et al., 2014)

2.3.1.1 Principle of a heat pump

As previously described, there are two types of geothermal heat pump systems: closed-loop GSHP (Ground Source Heat Pump) and open-loop GWHP (Groundwater heat pump). According to Brandl (2013), the principle of a heat pump is similar to that of a reverse refrigerator. In the case of the heat pump, however, both the heat absorption in the evaporator and the heat emission in the condenser occur at a higher temperature, whereby the heating and not the cooling effect is utilised. The coefficient of performance, COP, of a heat pump is a device parameter and defined by Eq. 1.

$$COP = \frac{energy\ output\ after\ heating\ pump\ [kW]}{energy\ input\ for\ operation\ [kW]} \qquad Eq.\ 1$$

This is typically used for heating operation, while for cooling the energy efficiency ratio, EER, (Insana, 2020) Eq. 2 is used:

$$EER = \frac{cooling\ \ capacity\ of\ the\ evaporator\ [W]}{power\ input\ of\ the\ compressor} \qquad Eq.\ 2$$

The seasonal performance factor (SPF) or seasonal COP (SCOP) is defined as:

$$SCOP = \frac{annual\ heat\ demand\ [kWh]}{annual\ electricity\ consumption\ for\ heating\ [kWh]} \qquad Eq.\ 3$$

and includes all the energy-consuming components, such as circulation pumps. Standard electric pumps allow to reach SPF values in the range 3.8-4.3 (Insana, 2020). For cooling the seasonal EER (SEER) is used:

$$SEER = \frac{annual\ cooling\ demand\ [kWh]}{annual\ electricity\ consumption\ for\ cooling\ [kWh]} \qquad Eq.\ 4$$

The efficiency of a heat pump is strongly influenced by the difference between extracted and actually used temperature. A high user temperature and a low extraction temperature in the heat exchanger (primary circuit) reduce its efficiency. For economic reasons a value of COP ≥ 4 should be achieved. Therefore, the usable temperature in the secondary circuit should not exceed 35–45°C, and the extraction temperature in the absorber pipes should not fall below 0–5°C.

If only heating or only cooling is performed, high-permeability ground and groundwater with a high hydraulic gradient are of advantage. However, the most economical and environmentally friendly operation mode is a seasonal operation with an energy balance throughout the year, hence heating in winter (i.e. heat extraction from the ground) and cooling in summer (i.e. heat sinking/recharging into the ground). In this case low-permeability ground and groundwater with only low hydraulic gradients are favourable (Brandl, 2013).

The operational scheme of a compression heat pump is exemplified in Figure 2. A working fluid, called refrigerant, is used. The refrigerant is a substance able to evaporate at low temperatures and to condensate at high ones. Heat exchange from the primary circuit to the refrigerant fluid occurs in the evaporator, while heat exchange from the refrigerant fluid to the secondary circuit takes place in the condenser. The basic principle is that when a fluid evaporates into a gas it absorbs heat, while the gas gives it off when condensing back to a liquid. This circular closed-loop process is the vapour compression cycle or refrigerant evaporation cycle (Insana, Thermal and Structural Performance of Energy Tunnels, 2020).

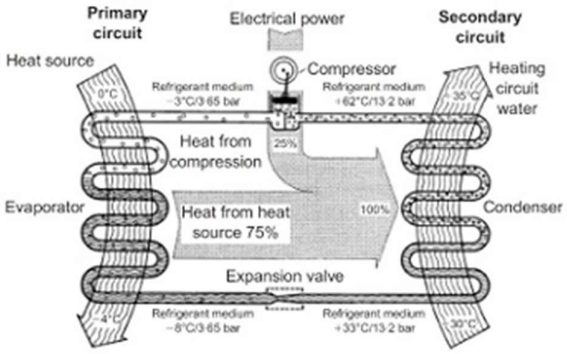

Figure 2. Scheme of operation of a compression heat pump (Brandl, 2006)

The main heat pump components are the compressor, the evaporator, the condenser, the expansion valve, the reversing valve and the control system. The evaporator is a coil where the refrigerant (initially liquid or gas/liquid mixture) absorbs heat from the heat source and boils becoming a low-temperature vapour. The compressor is the step that requires power, provided by an electrically driven engine, increases pressure and temperature of the refrigerant. As the evaporator, the condenser is a coil where the refrigerant (initially high-temperature superheated vapour) gives off heat to the heat sink and becomes a gas/liquid mixture or subcooled liquid. The expansion valve reduces the pressure that was created in the compressor, as a consequence temperature drops, and the refrigerant becomes a low-temperature liquid or gas/liquid mixture (Insana, Thermal and Structural Performance of Energy Tunnels, 2020).

2.3.2 Previous cases of study

2.3.2.1 Lainzer tunnel in Vienna

A first documented real-scale example of this innovative application is related to the Lainzer tunnel in Vienna (Adam & Markiewicz, 2009). The LT24 testing plant was the first application in the world where existing absorber technology, already successfully used for the foundations of buildings, was applied to bored piles of a cut-and-cover tunnel and allowed an extensive investigation. The piles are equipped with absorber pipes that are connected to a service room. The absorber pipes are connected to collection pipes, which lead to six heat pump units provided to heat an adjacent school building.

In construction lot LT22 of the Lainzer tunnel a completely new technology was developed for thermal activation of the concrete lining. Absorber pipes were first attached to non-woven geosynthetics off site, and then placed between the primary and secondary lining of the tunnel (Figure 3). This technology makes prefabrication possible, and provides for easier in situ installation. Similar to the testing plant LT24, sophisticated measurement instrumentation (temperature sensors, heat carrier flow measurement, etc.) was installed for detailed investigation. The initial operation of the energy plant started in February 2004 with the first heat extraction. However, the testing plant can be run in both heating and cooling operation.

Figure 3. Detail of the four absorber loops with collection pipe (Adam & Markiewicz, 2009)

2.3.2.2 Stuttgart-Fasanenhof Tunnel

During the construction of the Stuttgart-Fasanenhof urban rail link (U6) by the Stuttgarter Straßenbahnen AG a geothermal test section was set up on the basis of a heat exchange system in a tunnel section excavated using the New Austrian Tunnelling Method (NATM). The tunnel was extensively provided with temperature measuring points for the subsurface, concrete and tunnel air. A lab programme was undertaken to establish the geothermal soil parameters heat conductivity and heat capacity (Moormann & Schneider, 2010).

2.3.2.3 Linchang Tunnel

The paper by Zhang et al. (2014) is dedicated to studying the tunnel lining Ground Heat Exchangers (GHE) that extract geothermal energy from the surrounding rock by absorber pipes embedded in the tunnel lining for heating purposes, based on a field experiment at Linchang Tunnel in Inner Mongolia. The

experiment investigated the heat transfer performance of tunnel lining GHEs and its impact factors, including the flow rate, inlet water temperature and pipe distance.

A new line heat source model and its analytical solution were developed for the heat conduction of tunnel lining GHEs and consider both composite medium and time-dependent boundary conditions which will be very helpful for optimizing the design of tunnel lining GHEs. Addiotionally, an attempt to investigate the heat transfer performance of tunnel lining GHEs based on a thermal response test with a constant inlet temperature was made by the authors.

2.3.2.4 Katzenbergtunnel tunnel

Investigations carried out by Franzius and Pralle (2011) introduced a new system which allows segmentally lined tunnels to be turned into sources of renewable heat energy for the buildings above them.

For tunnels built by mechanized tunnelling, the final lining is made of precast concrete segments mounted by the TBM within the shield protection. Precast segments are assembled to shape a ring, 1–2 m long. Typically every ring is made of 6–7 segments. In 2009 the first energy segments ring was tested in Katzenbergtunnel, before tunnel opening, where 5 segments were thermally activated for a total surface of 60 m^2 and a heat flux of around 10–20 W/m^2.

2.3.2.5 Jenbach railway tunnel

The energy segments developed by Rehau AG & Co and Ed. Züblin AG (Frodl, Franzius, & Bartl, 2010) for the exploitation of geothermal energy in mechanically bored tunnels were put into use in a pilot scheme 54 m long in the Jenbach Tunnel (Austria) to supply heat to a building on the surface. The project was equipped with comprehensive monitoring system, which allows the measurement of the temperature of the segments and also the feed and return pipes (Frodl et al., 2010).

2.3.2.6 Seocheon tunnel

The geothermal energy from a tunnel structure is extracted through a textile-type ground heat exchanger named "Energy Textile" that is fabricated between a shotcrete layer and guided drainage geotextile. To evaluate the thermal performance of the energy textile, a test bed was constructed in an abandoned railway tunnel located in Seocheon, South Korea. The thermal conductivity of shotcrete and lining samples and the overall performance of the energy textile were evaluated. In addition, a 3-D finite volume analysis (FLUENT) was adopted to simulate the

operation of the ground heat exchanger being encased in the energy textile with the consideration of the shotcrete and lining thermal conductivity, fluid circulation rate, the existence of groundwater and the arrangement of circulation pipes (Lee, et al., 2012).

2.3.2.7 Crossrail tunnels

Nicholson et al. (2015) provided an overview of a TES system for Crossrail where heat is generated by the trains in the tunnels all year round. The system uses an embedded closed-loop water-filled pipework in tunnel segments to extract this heat. In this way it both cools the tunnels and provides heat for adjacent buildings. The water temperature supplied to the heat pumps is relatively high, enabling the system to operate at a higher COP compared with conventional ground source heating systems. The project did not go ahead because of time constraints and high mould modification costs. Nevertheless, the development of this technology on Crossrail has provided a vital building block in understanding the benefits of the system such that it can be implemented at scale on future projects.

2.3.2.8 Grand Paris tunnels

The investigation carried out by Cousin et al. (2019) focuses on the analysis of the thermo-hydraulic behaviour of tunnel energy segmental linings for a twofold purpose: (i) to address the energy performance of the considered technology for a variation of design solutions including the pipe configuration, the flow rate of the heat carrier fluid circulating in the pipes, and the pipe embedment from the tunnel intrados; and (ii) to assess the economic attractiveness and profitability of thermal power plants resorting to energy segmental linings depending on the considered design solutions, in addition to the thermally active tunnel length. To achieve the previous goals, this study is based on three-dimensional (3-D) thermo-hydraulic finite element analyses of a real case study referring to the project 'Grand Paris Express', as well as on the economic analysis and profitability assessment of the considered energy network.

2.3.2.9 The Enertun technology

An innovative energy segment for tunnel lining was patented by Politecnico di Torino in 2016, called Enertun (Italian patent number: 102016000020821, European patent number: 16834047.9), and tested in an experimental site installed in the tunnel of Turin Metro Line 1. Data were collected between 2017 and 2018 to form the basis of the performance assessment of the technology. Promising outcomes encouraged the authors to collaborate in this direction over the project of

Turin Metro Line 2 to propose a methodology for assessing the thermal energy potentially exploitable by an underground infrastructure (Barla, et al., 2019).

Thanks to an innovative layout of the geothermal probes, the Enertun energy segment reduces head losses by 20–30% in each ring and increases its energy efficiency up to 10%. The same segment can be used to cool down the tunnel environment. There are three different configurations of the segment, according to the pipes mesh positioning, that is close to the extrados (Ground), close to the intrados (Air, Figure 4) or it can include two circuits, one per each of the previous locations (Ground&Air). In the first case the heat exchange with the ground is predominating, while it mainly involves air in the second case. In the third case, heat exchange can occur in both directions (Barla & Insana, 2022).

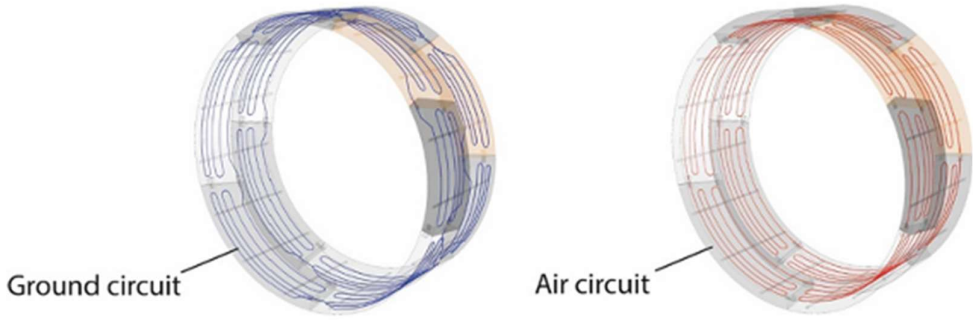

Figure 4. Ground and Air Enertun configurations, which can be eventually combined together (Barla & Insana, 2022)

2.3.3 Design aspects of thermal activation

In recent years, increasing studies have investigated the thermo-hydraulic behavior of energy tunnels, as this aspect governs their energy performance. In contrast, the thermo-mechanical behavior of energy tunnels has remained marginally explored, despite its crucial role for the geotechnical and structural performance of such structures (Rotta Loria et al., 2022).

Investigations have shown that thermal loads, applied alone or in conjunction with mechanical loads, can significantly affect the geotechnical and structural performance of energy geostructures such as energy piles and for this reason must be considered in their design at serviceability limit states (Rotta Loria, 2019). Therefore, understanding the influence of thermal loads on the mechanics of energy tunnels appears paramount. On the one hand, this knowledge can expand the current

understanding of thermally induced effects on the geotechnical and structural performance of energy tunnels, highlighting the physical conditions where the mechanics of energy tunnels is likely to be most affected by such effects. On the other hand, this knowledge can unravel the necessity of considering thermally induced effects in future designs of energy tunnels (Rotta Loria et al., 2022).

Having said this, thermal activation of energy linings entails at least two technical aspects that need to be taken into account during the project stages. An energy optimization analysis, aimed at maximizing the performance under the same costs and evaluating the thermo- hydraulic interaction with the ground, is run first (thermal design). This is followed by the structural design, that identifies the mechanical effects in the structural elements following the thermal loading, assessed from previous stage, so that long-term integrity can be guaranteed. These aspects can be tackled through thermo-mechanical (TM) and thermo-hydraulic (TH) numerical modelling respectively. Fully coupled thermo-hydro-mechanical (THM) simulations can be, initially, avoided as in most cases the computational effort and the increase in calculation time are not reflected in a more accurate result (Barla & Insana, 2022).

2.3.3.1 Thermal design

If structural design can be reasonably deepened later in the design stages, it is the thermal design that has to be addressed as early as the tunnel concept (Barla & Insana, 2022). In the thermal design the intention is never to define the geometric restraints of the structure based on the geothermal requirement, but to determine the amount of thermal energy that could be provided by the energy tunnel. To this aim, literature values for initial ground thermal properties, such as temperature, thermal conductivity and heat capacity, are often used instead of collecting site-specific geotechnical input through laboratory and in-situ testing, and monthly thermal loads are used in lieu of appropriate timestepping and realistic analyses (Insana, Thermal and Structural Performance of Energy Tunnels, 2020).

First of all, following the flow chart in Figure 5, supplementary investigations should be carried out, whose level of detail will depend on the design stage, aimed at assessing the ground thermo-hydro-geological characteristics that can influence the heat transfer processes (Vieira et al., 2022). The material parameters that have to be assessed are shown in Figure 6.

Among in situ testing techniques, the Thermal Response Test (TRT), very common for BHE and energy piles, is useful to evaluate ground thermal

conductivity, heat exchanger thermal resistance and undisturbed ground temperature. Laboratory testing can be classified into steady-state methods (e.g. hot guarded plate) and transient methods (e.g. needle probe, transient plane source) that allow assessing thermal conductivity, thermal diffusivity and volumetric heat capacity (ASTM, 2014). However, laboratory measurements do not take into account site-specific conditions such as groundwater flow, spatial heterogeneity and scale effects that directly affect real thermal properties (Vieira, et al., 2017).

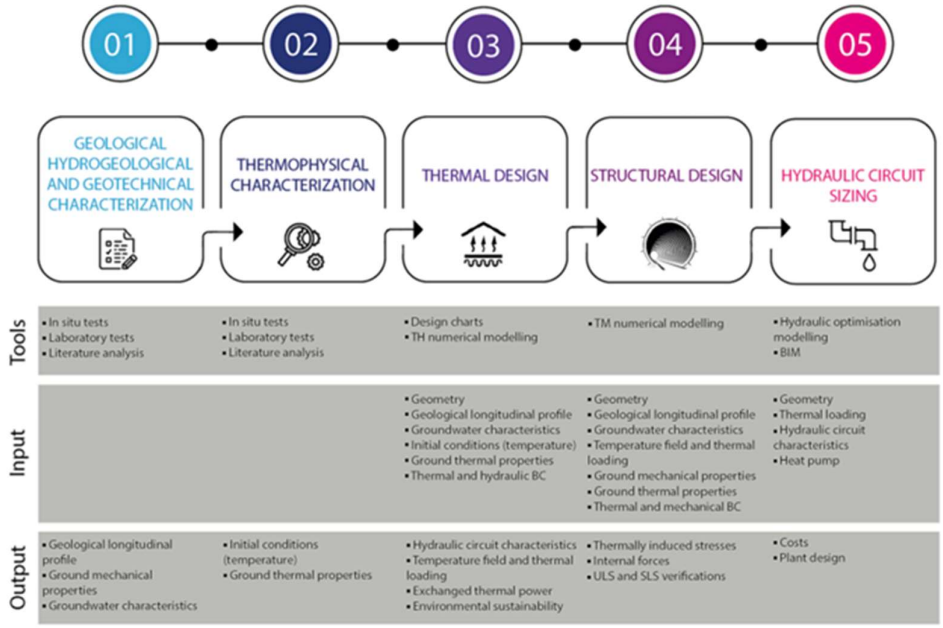

Figure 5. Design flow for an energy tunnel (Barla & Insana, 2022)

Properties	Investigations
Thermal conductivity, λ [W/mK]	TRT, needle probe, transient plane source
Thermal specific capacity, S_c [J/kgK]	Transient plane source
Undisturbed temperature, T_0 [°C]	TRT, measures at different depths with level probe with temperature sensor
Effective porosity, n_e	Classification laboratory testing
Horizontal and vertical permeability, k_h, k_v [m/s]	Pumping tests, slug test
Groundwater flow velocity, v [m/s]	Level probe, existing groundwater maps
Groundwater depth, f [m]	Level probe, existing groundwater maps
Groundwater flow direction, df	Level probe, existing groundwater maps

Figure 6. Ground and structural elements properties to be determined for thermal design of an energy tunnel (Barla & Insana, 2022)

Furthermore, if the thermal parameters and loads are misestimated, it could lead to short- and long-term failures that should not be seen as outright collapses but as the equivalent of a serviceability limit state in geotechnical design (Insana, 2020). These assumptions are in accordance with the conclusions from Preene and Powrie (2008), who stated that while it appears unlikely that the ground element of a ground energy system could fail in a way that would be analogous to outright collapse, there are several ways in which a serviceability limit state could be reached. Reflecting the fact that ground energy systems receive a dynamic thermal load over a long period of time, these might be grouped as follows:

1. Short term failure: This might be viewed as the nearest analogy to an ultimate limit state in that it would be obvious and relatively immediate. It will generally occur within one annual cycle and will manifest in the ground energy system being unable to deliver the peak heating or cooling load – the system therefore fails to meet the thermal load applied to it.
2. Long term failure: The ground energy system can meet the building thermal load requirement, but the heat flow does not balance sufficiently well over an annual cycle resulting in a gradual increase or decrease in the ground temperature and a gradual reduction in system efficiency, and eventually its capacity. Thermally, the ground is overstressed. Typically the system will work, but less and less effectively resulting in increased energy costs and increased carbon dioxide emissions. It will not deliver the promised thermal, economic and environmental performance, and is thus analogous to a serviceability limit state.
3. Failure to meet regulatory standards: Some forms of ground energy system are subject to formal regulation which governs the way they operate (e.g. abstraction licensing of open loop systems). Systems which are deficient in aspects of design and/or operation may breach their regulatory requirements, in either the short or the long term.

2.3.3.1.1 Calculation of exploitable heat

To quantify the geothermal potential, a 3D thermo-hydraulic numerical model able to reproduce a portion of the thermally active lining has to be built. In the case of energy segments, a limited number of tunnel rings equipped with heat exchangers can be reproduced. In general, it is possible to refer to finite elements or finite difference codes (Barla & Insana, 2022).

To build the numerical model the correct case study geometry has to be accurately reproduced, including the layout and the geometry of the geothermal circuit and the ground thermal and hydrogeological conditions. After setting initial conditions, the analysis is carried out by fixing inlet temperature and inlet/outlet velocity in the circuits and monitoring outlet temperature, function of the heat transfer which is reproduced numerically during the simulation. By changing inlet temperature, the analysis can simulate the system behavior during the different thermal activation seasons. For instance, 24 to 28 °C, summer operation is simulated, when excess heat is dispersed in the ground. Between 3 and 6 °C, it is possible to simulate winter operation, characterized by heat extraction from the ground (Barla & Insana, 2022).

To investigate the thermal feasibility of energy geostructures, when the pipes are explicitly modelled, the exchanged heat can be computed from the results of the numerical analysis using the equation below:

$$Q = mc(T_{out} - T_{in}) \qquad \textit{Eq. 5}$$

where Q (in Watt) is the exploitable heat of the site, m (in kg/s) is the mass flow rate, (in $J \cdot kg^{-1} \cdot °C^{-1}$) is the heat capacity of the circulating fluid at constant pressure, T_{in} (in °C) is the inlet temperature and T_{out} (in °C) is the outlet temperature of the heat carrier fluid running in the pipes (Alvi et al., 2022). The power per tunnel lining unit area in W/m^2 is obtained by dividing by the ring outer (or inner, as in Cousin et al., 2019) surface (Insana, 2020):

$$q = \frac{Q}{L\pi D} \qquad \textit{Eq. 6}$$

where L and D are the ring thickness and external diameter. In the study by Tinti et al. (2017), it can be noted that maximum temperatures and maximum power occur under different conditions, as high temperatures are associated with low flow rates, which decreases power, and vice versa.

2.3.3.1.2 Sensitivity studies

An energy tunnel consists of three main parts, namely the heat carrier fluid in the pipes, the surrounding soil or rock mass, and the air inside the tunnel (Tinti, et al., 2017). Their thermal performance is affected by a number of factors, among which arrangement of the pipes, thermo-hydraulic properties of the ground,

presence and velocity of the groundwater flow, tunnel air temperature, far field ground temperature and thermal load curve (Insana, 2020). In this context, Zhang et al., (2014) investigated the heat transfer performance of tunnel lining GHEs and its impact factors, including the flow rate, inlet water temperature and pipe distance. The following conclusions in the investigation were reached:

- The bigger the pipe spacing is, the faster the ground temperature recovery. This is caused by temperature superposition effect during the system operation. The temperature superposition effect is determined by pipe distance, that the bigger the pipe distance is, the less significant temperature superposition. It can be concluded that the intermittent operation is of advantage to the ground temperature recovery.
- During heat injection, the heat exchange rate presents a linear variation as the inlet temperature of the heat carrier liquid increases; the higher the inlet temperature of carrier liquid is, the larger the heat exchange rate is.
- The heat exchange rate of absorber pipe decreases with extension of running time, as also that the greater the flow velocity, the greater the heat transfer.
- The heat exchange rate gradually decreases with an increase in the operating time. The variable flow rate can affect the heat exchange rate.
- Analyzing the relationship between the geothermal energy output and pipe distance which does not consider the effect of groundwater, it can be said that the greater the pipe distance is, the higher the heat exchange rate of heat exchanger pipes is, and the lower the geothermal energy output from surrounding rock is.

Soussi et al. (2016) argue that the influence of the groundwater on the system increases with its flow velocity. In summer, it prevents heat storage in the rock near the tunnel so it can evacuate more heat and thus cool the building more efficiently. In winter, the flow renews the temperature therefore the exchanger extracts more heat from the rock.

The effects of some key parameters, such as groundwater flow, ground temperature, and ground thermal conductivity, were studied by Di Donna and Barla (2016), using a parametric analysis. According to the specific site conditions, design charts were developed to assess system energy efficiency in order to save time and avoid complete numerical modeling. The design charts were updated later by Insana and Barla (2020) to take into account Enertun's favorable configuration.

The latter charts are more comprehensive since the groundwater flow orientation around the tunnel axis is also taken into account along with the heat carrier fluid inlet temperature, thanks to a formula that corrects the exchanged heat obtained from the charts. These design charts are shown in Figure 7 for winter and summer operations, as well as for three different groundwater flow directions. The specific heat power in W/m^2 is obtained from a triplet of data, that is groundwater flow velocity (x-axis), ground initial temperature (y-axis) and total thermal conductivity. They can be used for a preliminary assessment of the heat exchanged.

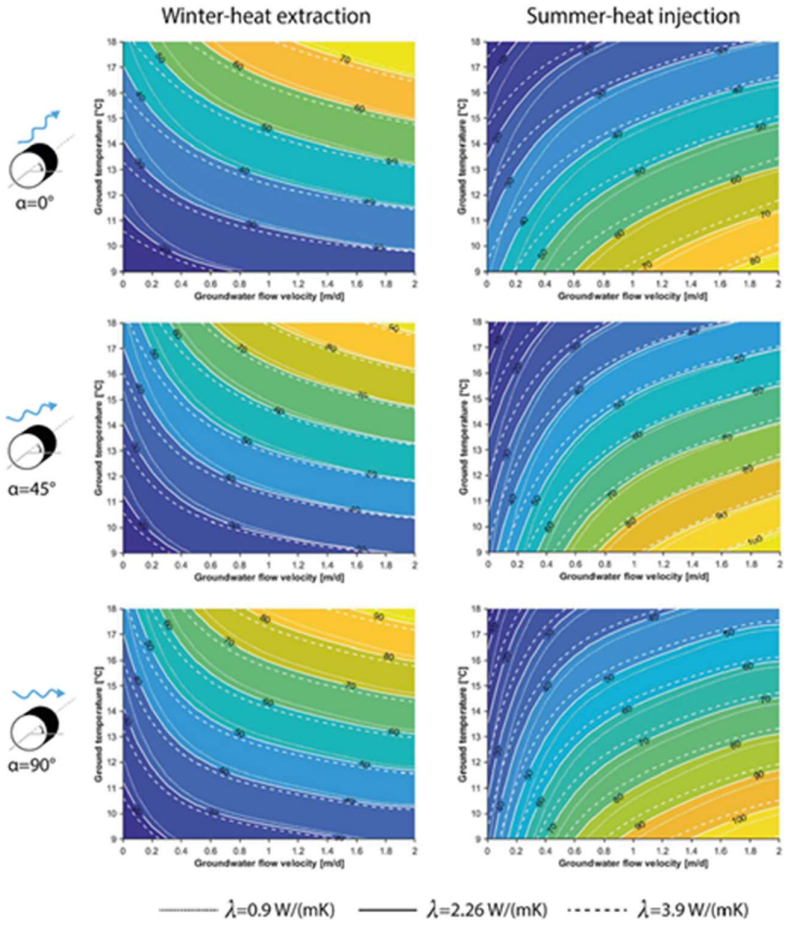

Figure 7. Example of design charts for the definition of geothermal potential in W/m^2 (Insana & Barla, 2020) in winter and summer for multiple groundwater flow directions (0°, 45° and 90°)

Barla and Insana (2022) noted a few relevant aspects regarding the design charts. Firstly, no matter the flow direction, the highest performance is obtained with maximum ground thermal conductivity, maximum groundwater flow, due to

the thermal recharge mechanism that allows the ground to return more rapidly to its undisturbed temperature, and with maximum ground temperature in winter and viceversa in summer. As groundwater flow velocity decreases, thermal conductivity starts playing a role. By observing the effect of groundwater flow, it is inferred that the performance is significantly increased when the flow is perpendicular to the tunnel axis as compared to an orientation of 0°.

During design another aspect to consider is the configuration of the rings, whether in series or in parallel and how many rings to connect in each subcircuit (Insana, 2020). Barla et al. (2016) carried out an optimization study considering a number of layouts and concluded that the solution with rings connected in parallel is the best one, as the temperature gradient of the heat carrier fluid decreases along its path. Therefore, connecting the rings in series means that the efficiency is progressively reduced, as the increase in temperature difference between inlet and outlet is not comparable to the increase in exchange area.

Another interesting aspect that can influence thermal performance is the operation mode (Insana, 2020). Ogunleye et al. (2020) investigated the operation of an energy tunnel for heat extraction in intermittent modes under varying tunnel air temperature and concluded that running the system intermittently increases the thermal output. Intermittent operations are characterised by a lower ground temperature drop and a higher recovery rate compared to a continuous operation, resulting in a more efficient system. In addition, the temperature time history of the air inside the tunnel also affects the heat exchange process, and it is important to include this when estimating the geothermal potential of an energy tunnel.

2.3.3.1.3 Governing equations

Given the physical processes involved in energy tunnels-related problems, including thermal, hydraulic and mechanical aspects (Figure 8), coupled approaches are needed to study the problem in a holistic way. In particular, the thermo-hydraulic problem mathematical formulation is ruled by the following equations governing fluid flow and heat transport coupling (Insana, 2020):

- Mass conservation equation (continuity equation)
- Darcy's law
- Energy conservation equation

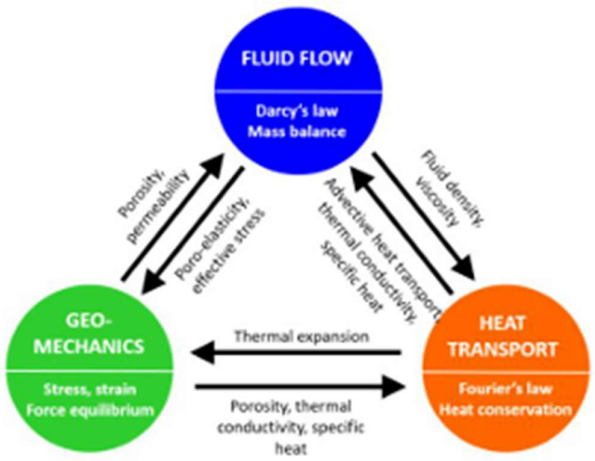

Figure 8. THM problem couplings (Insana, 2020)

To solve the coupled problem, appropriate boundary conditions, both thermal and hydraulic, need to be set. Temperature boundary conditions can be of three types:

- Dirichlet-type or temperature boundary condition, T=constant (°C);
- Neumann-type or heat flux boundary conditions, q=constant (W/m^2);
- Cauchy-type or heat-transfer boundary condition, where a reference temperature is given together with a heat transfer parameter h (W/m^2 °C).

2.3.3.1.4 Design parameters

Thermal conductivity: it is the parameter characteristic of conductive heat transfer measuring how well a material conducts heat, accordingly to hydraulic conductivity and electrical conductance. It is the constant of proportionality in 1D Fourier's law, the basic law of conduction, that applies at steady state and describes the relationship existing between the heat transfer rate and the profile of temperature (Insana, 2020):

$$\frac{Q}{A} = -\lambda \frac{dT}{dx} \qquad \textit{Eq. 7}$$

where Q is the heat flow rate along x (W), A is the area normal to x (m^2), dT/dx is the temperature gradient (K/m). Its determination can derive both from national databases including laboratory and field measurements or from correlations based on phase proportions. Its value has a strong impact on ground energy design and

system size in case of absence of groundwater flow and it is directly related to the thermal performance and to the ground recover capacity. For concrete the thermal conductivity ranges between 1 to 4 W/(mK), based on mix design, water content, aggregate lithology and volume ratio (Insana, 2020). Ground with higher thermal conductivity not only yields larger heat transfer rates but also recuperates more rapidly from thermal depletions and thermal build-ups (Vieira, et al., 2017).

Volumetric heat capacity: it is defined as the amount of heat that is needed to increase the unit mass temperature by one degree. As for thermal conductivity (Eq. 9 and Eq. 10), volumetric heat capacity can be expressed by weighting the relative phase proportions (Insana, 2020):

$$S_{cv} = (1-n)S_{cv,s} + nS_rS_{cv,w} + (1-S_r)nS_{cv,a} \qquad \textit{Eq. 8}$$

Upper bound:

$$\lambda_{eff(max)} = (1-n)\lambda_s + nS_r\lambda_w + (1-S_r)n\lambda_a \qquad \textit{Eq. 9}$$

Lower bound:

$$\frac{1}{\lambda_{eff(min)}} = \frac{1-n}{\lambda_s} + \frac{nS_r}{\lambda_w} + \frac{1-S_r}{\lambda_a} \qquad \textit{Eq. 10}$$

where n is the porosity, S_r the degree of saturation, λ_s, λ_w, λ_a are the soil, water and air thermal conductivity.

Undisturbed temperature: it is a key thermo-geological parameter needed for the assessment of the geothermal potential of an area. The temperature difference between the undisturbed ground temperature and the mean heat carrier fluid temperature circulating in the heat exchanger leads directly to the heat transfer between the ground heat exchanger and the surrounding ground.

Thermal resistance: The thermal resistance of the GHE is the effective thermal resistance between the heat carrier fluid circulating in the pipes and the edge of the geostructure in contact with the surrounding ground. A low value of thermal

resistance means enhanced heat transfer inside the GHE, which, in turn, means a GHE with a smaller size and lower installation costs (Vieira, et al., 2022). It is given by:

$$R = \frac{T_1 - T_2}{q} \qquad \textit{Eq. 11}$$

where T_1-T_2 is the difference between the heat exchangers fluid temperature and the temperature at the geostructure boundary and q is the heat transfer rate applied in W/m (Insana, 2020).

Thermal diffusivity: Soil thermal diffusivity is a measure of how quickly heat can move through soil. It is defined as the ratio of the soil's thermal conductivity to its volumetric heat capacity (Jong van Lier & Durigon, 2013):

$$\alpha = \frac{\lambda}{\rho \cdot c_\rho} \qquad \textit{Eq. 12}$$

where λ is the thermal conductivity (W/(m·K)), ρ is the density (kg/m3) and c_ρ is the specific heat capacity (J/(kg·K)).

2.3.3.2 Structural design

The goal of structural design for energy tunnels is to examine the effects that thermal activation involves on the stress state in the lining, illustrating additionally the implications on structural dimensioning, if any. This is consequent to the change in internal actions caused by the change in the state of stress. In particular the key aspect is the quantification of the effect that thermal change, due to the fluid circulation within pipes in the lining, induces in terms of stresses. Once this is done, the influence on internal actions can be ascertained and the lining structural design can be updated, accounting for the loading scenario associated with the operation of the geothermal heat exchanger (Barla & Insana, 2022).

Insana (2020) conducted a detailed study on the assessment of the additional thermal stress and/or strain state for tunnel concrete linings, using experimental data and numerical analyses to understand how stresses and strains vary in the concrete lining in different directions and the order of magnitudes. The experimental campaign was conducted at the Turin Metro Line 1 full-scale test site under both natural and thermally activated conditions. Based on such findings with reference

to a coarse-grained soil, upon cooling (winter heating mode), a decrease in lining temperature of 4–6 °C is observed in the conditions studied, resulting in hoop contraction strains of some tens of microstrains and a decrease in compressive stresses of several MPa. In contrast, expansive strains and a rise in compressive stresses are observed upon heating (summer cooling mode), although experimental data indicate an order of magnitude of some MPa in this case.

The problem can be investigated into more detail by resorting to numerical modeling. To analyze the energy lining working condition, a numerical model with thermomechanical formulation is needed, that allows to couple the mechanical and thermal aspects. The numerical model will be such as to reproduce the different construction phases of the tunnel until commissioning, adding the heat exchange pipes, and an appropriate law of variation in temperature that reproduces the functioning of the system both in winter and in summer. In particular, referring to a geothermal system with the double role of heating and conditioning, the structure will be prone to temperature variations during the several seasonal cycles that can trigger internal stress state changes. Such changes can give rise to a stress reduction, that is a compression, or to a stress increase in tension (Barla & Insana, 2022).

2.3.3.2.1 Design parameters

Thermal expansion coefficient: the thermo-mechanical volumetric behavior of soil is complex due to its highly non-linear and irreversible stress-strain behavior and to its multiphase constitution (Vieira, et al., 2022). It is not possible to define a simple thermal volumetric soil thermal expansion coefficient (Mitchell, 1993) as it depends on several aspects related to the soil constitution, to the in-situ conditions (effective stresses, pore water pressure, permeability and drainage conditions) and the imposed thermal loads. However, due to the difficulty in assessing this parameter, and for simplification, a constant value is generally considered. Typical values for solid grains range from 1×10^{-5} to 3.4×10^{-5} [°C^{-1}] (Delage, 2013), whilst the thermal expansion coefficient of water is 27×10^{-5} [°C^{-1}]. It is expressed as the constant of proportionality between the temperature rate and the volumetric strain rate and can be determined by performing non-isothermal drained isotropic tests in OC specimens. On the other hand, for different types of rock specimens values from 1.11×10^{-5} [°C^{-1}] up to 5.8×10^{-5} [°C^{-1}] depending on their mineralogy can be found in the literature (Insana, 2020):

$$\dot{\varepsilon}_v = -\beta\dot{T}$$

Eq. 13

2.3.3.3 Hydraulic network sizing and preliminary cost analysis

As part of the design process, the hydraulic network that circulates the heat carrier fluid and is connected to the heat pump must be appropriately sized. Research carried out at Politecnico di Torino (Rosso et al., 2021) showed that the most cost-effective layout is obtained by balancing the primary circuit installation cost, increasing with circuitry cross-section, and pumping costs, decreasing with circuitry cross- section. Such balance is highly affected by economic factors (e.g. pipes installation costs, energy cost), thermal comfort (e.g. utilization rate of the heat exchanger) and plant-related factors (e.g. pipes length and heat carrier fluid temperature changes). Hence, optimization of the hydraulic network has to be defined according to the specific application, based on a cost-benefit analysis accounting for the above-mentioned technological aspects, site geometry and potential customers identification.

Costs evaluation comes down to assessing the extra costs (both materials and workmanship) needed for thermal activation beyond those for building the geostructure. As for workmanship, the process introduces some additional activities, such as pipes embedment in the precast segments. This task takes place in the precast concrete plant with a slightly higher burden of the workforce for laying pipes inside reinforcement and arranging pockets for linking segments to one another. After tunnel excavation and rings erection, the segments of each ring will be connected to set up a closed hydraulic loop and header pipes will be installed for ensuring the flow (Barla & Insana, 2022).

The result of an optimization analysis carried out by Barla and Insana (2022) at the experimental site in Turin Metro Line 1 tunnel accounting for the above-mentioned costs is shown in Figure 9, where the revenue to costs ratio for variable parameters can be observed. Revenues were obtained by means of thermo-hydraulic analyses that allowed to get the outlet-inlet temperature difference and, hence, the exploitable heat power for the Torino case study (Rosso et al., 2021). The hydraulic optimisation analysis considered the costs of the circuitry components and the costs for pumping the heat carrier fluid through the primary circuit. It calculated installation costs, head losses and hydraulic power, based on which the pumping energy cost was estimated. The revenue to costs ratio was obtained by dividing the economic benefits and the hydraulic costs. From Figure 9 it turns out that all-in-parallel rings (red line) is the best case up to 450 m. As tunnel length increases, the highest revenue is obtained with two rings in series (Barla & Insana, 2022).

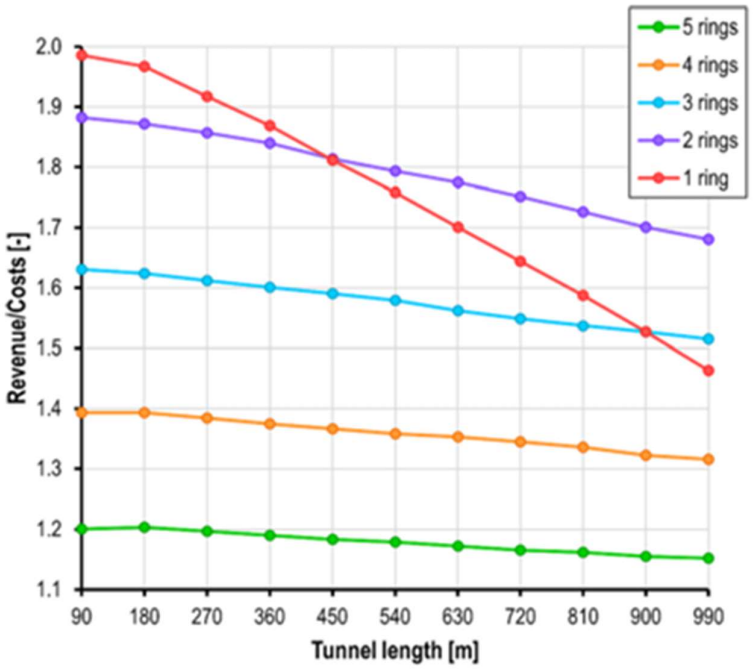

Figure 9. Revenue to costs ratio for different configurations and tunnel lengths (operation over 180 days, 12 h per day) (Barla & Insana, 2022).

2.3.4 Integration with district heating networks

If the extracted heat can be used directly for the line stations or with reference to specific receivers identified among the surface buildings, an interesting possibility which was investigated in the study by Barla and Insana (2023) iis to integrate the energy tunnel system within the district heating network. In this case, a scheme like the one shown in Figure 10 can be assumed. The tunnel (Geothermal Ring) plays the role of thermal source for the low-temperature ring (Primary ring) through the use of a heat pump (Primary heat pump). The geothermal loop is then the source, evaporator side, for the heat pump which raises the temperature from the tunnel operation levels (4–10 °C) to around 45 °C. The primary network can thus serve directly the newly built volumes and, in general, the users characterized by low specific consumption and equipped with low-temperature thermal plants (Barla & Insana, 2022).

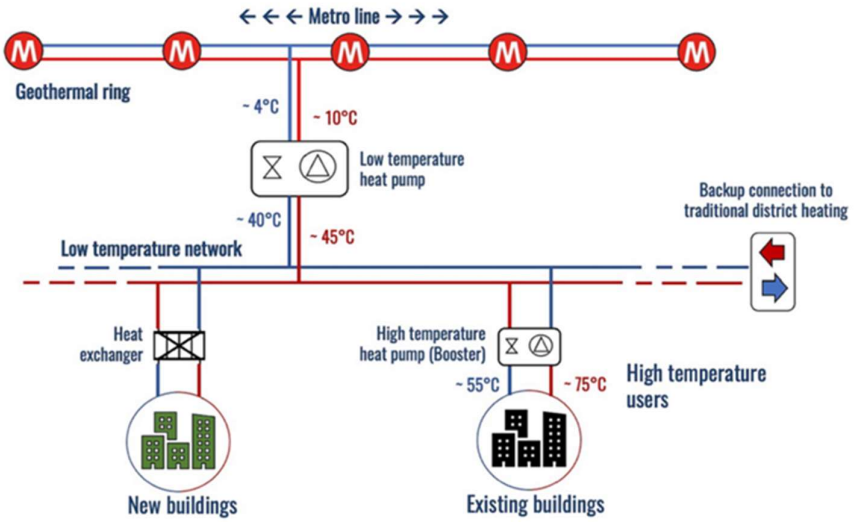

Figure 10. Conceptual scheme of the geothermal system (Barla & Insana, 2022)

In the study carried out by Meibodi and Loveridge (2022) the capability and feasibility of the integration of energy geostructures with district heating and cooling systems is evaluated. They state that the connection of energy geostructures to the heat network, operating at different temperature levels, is a feasible solution in the framework of the fifth generation thermal energy network's schematic concept (Barla & Insana, 2022; Meibodi & Loveridge, 2022).

In this context, end-users' substations are essential components of all thermal networks due to their significant role in satisfying the thermal energy demands of buildings. However, their roles in fifth generation networks are even more critical, as each substation connected to the fifth-generation networks operates both as a consumer and producer. The main concept of the 5GDHC network is depicted in Figure 11.

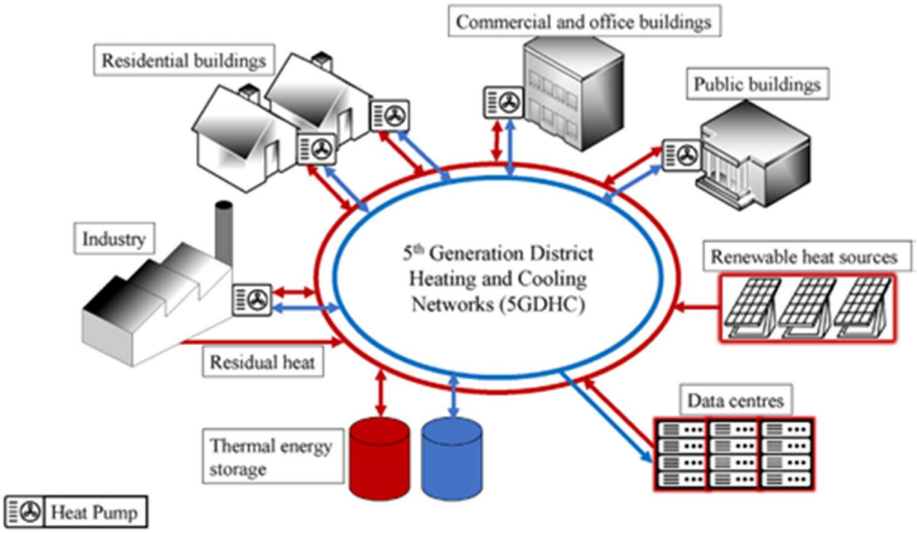

Figure 11. A representation of a typical fifth generation district heating and cooling network (Meibodi & Loveridge, 2022).

Chapter 3

Description of the case studies

3.1 Introduction

The present chapter provides insights into significant infrastructure projects in Italy, namely the Subport Tunnel in Genova, the Trento ring road tunnel and the Cortina D'Ampezzo bypass tunnel.

Firstly, the Subport Tunnel in Genova is a submarine tunnel project that aims to improve the efficiency of the fast road connection in the city, connecting the western road network to the eastern part of the city. Secondly, the Trento railway undergrounding project aims to bury the historic railway line in Trento in three phases, including the construction of a bypass line, burial of the historic line, and the development of a North-South connection. Finally, the Cortina d'Ampezzo bypass tunnel is evaluated as a deep tunnel in a mountain environment with the aim of creating a bypass to the town, currently crossed by both the S.S. 51 "di Alemagna" and the State Road 48 "delle Dolomiti" in light of the Winter Olympic Games Milano-Cortina 2026.

For each project the subsequent sections present i) the summary of the main works, ii) the geotechnical characterization of the site, iii) the geothermal and iv) hydrogeological frameworks. Although the geotechnical properties are documented for completeness, they are not employed in the quantification of the geothermal potential, which is described in Chapter 4 of this Thesis.

Part of the work presented in this Chapter comes from the technical reports developed by Autostrade per l'Italia, Rete Ferroviaria Italiana (RFI) and Anas Gruppo FS Italiane, for the Subport Tunnel in Genova, the Trento ring road tunel and the Cortina D'Ampezzo bypass tunnel, respectively.

3.2 Subport Tunnel in Genova

3.2.1 Description of the chosen project solution

This project concerns the road crossing of the internal basin of the Port of Genoa created via an underwater tunnel which will connect the city's western road network, near the San Benigno hub, to the Foce district, in the east of the city (see Figure 12). The project envisages that the tunnel will be equipped with ramps to connect with the central area of the city, in the Madre di Dio/Via Casaccie area.

The project is motivated by the need to improve the efficiency of the fast road connection crossing the city, currently made up of the elevated road built in the early 1960s and no longer able to satisfy the traffic characteristics, also as a result of the urban planning that affected the west, the ancient port and the historic centre, and those being implemented in the east. The current project, developed pursuant to the Agreement stipulated on 14 January 2021 by Autostrade per l'Italia with the Liguria Region, the Western Ligurian Sea Port System Authority and the Municipality of Genoa, resumes the project developed in 2003 and approved by CSLL.PP. in the meeting of 12/15/2005.

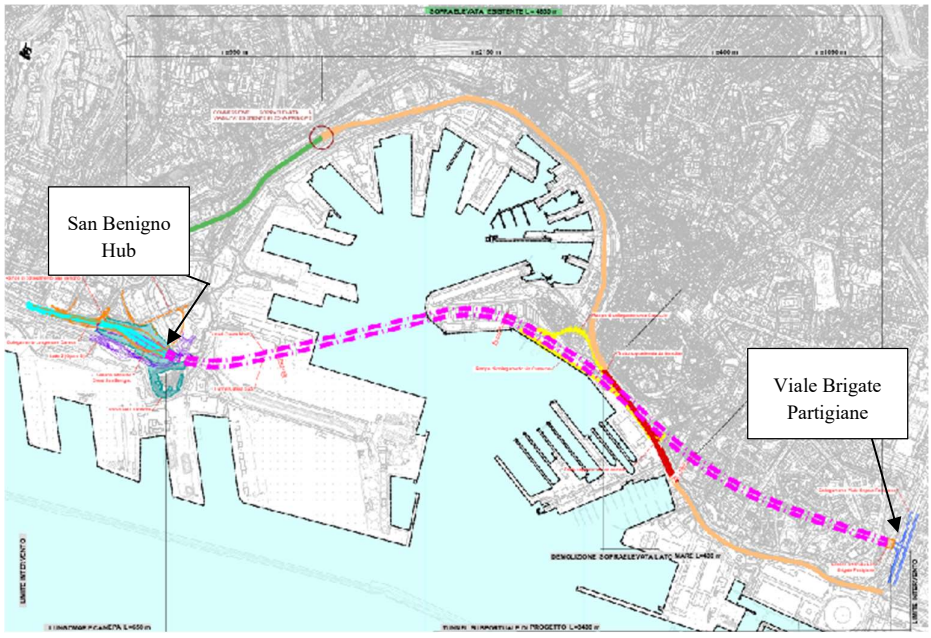

Figure 12. Plan view of the route (Autostrade per l'Italia, 2021)

The route, approximately 3.49 km long, will consist of two separate main tubes, one for each direction of travel, created by mechanized excavation using a TBM. The diameter of each tube is equal to 15.40 m (see Figure 14) including a tunnel lining with a thickness of 0.55 m and a jet grout with a thickness of 0.25 m. Modest sections in artificial tunnels and trenches are planned at the entrances to connect the new infrastructure to the existing road system. On the western side, the tunnel is connected to the Lungomare Canepa road network and, from this, through the Guido Rossa expressway, to the Genova Airport motorway toll booth (A10). The connection with the Genova Ovest toll booth (A7) is instead guaranteed through the road system of the new San Benigno junction. On the Eastern side, the connection to the city road network takes place on Viale Brigate Partigiane, Foce district, effectively following the connection currently guaranteed by the Aldo Moro elevated road. In the central area of the Old Port, the new route connects with a special junction with the road axis of Via Madre di Dio.

From the point of view of the works, most of the route is underground. As anticipated in the previous section, a tunnel will be built consisting of two separate main tubes, one for each direction of travel. More specifically, the central part of the work, between approximately pk 0+072 and pk 3+492, for a total length of 3420 m, will be carried out with a blind hole, by mechanized excavation, using a shielded TBM cutter, with integral attachment, with counter-pressure at the face with bentonite mud, such as Hydroshield, capable of tackling excavation in inconsistent or poorly coherent soils even in the presence of aquifer, with the ability to adapt to the variability imposed by the geotechnical context along the route and to the heterogeneity of the materials.

The total length of the twin tunnel, equal to 3420 m per tube, involves the construction of by-passes, seven in total, connecting the two tubes. The distance between the pedestrian by-passes (and between the first external by-passes and the entrances) is set at 500 m, in accordance with the reference regulations for the type of twin tunnels.

The two tubes will be excavated proceeding from the West entrance towards the East entrance. In the first phase, the South tube will be excavated, the machine will then be dismantled and recovered from the East entrance shaft and reassembled in the West shaft on the San Benigno side to proceed with the excavation of the North tube.

For the first 650 m approximately, the route passes under the western port area (Figure 13) and has variable intermediate overburdens which increase with advancement, up to a maximum of 30 m. For the next 400 m or so the route sinks below the seabed near the port basin. The overburdens are reduced to a minimum covering of 13 m and a hydraulic head of approximately 33 m of water. In the middle of the underwater section, an emergency pedestrian by-pass will be positioned. The excavation of this by-pass is critical in terms of controlling water inflows and stability. Therefore, in the feasibility project two solutions were proposed to create this structure using a natural excavation with the technology of freezing in brine of an annular area of land, or vice versa using a mechanized excavation by means of micro-TBM.

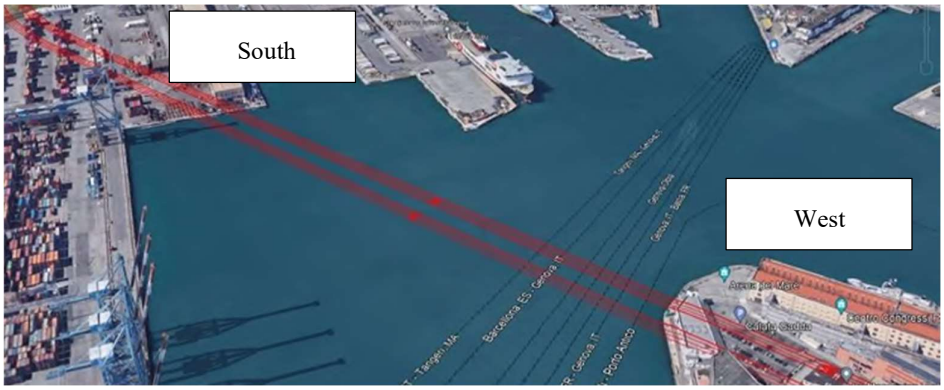

Figure 13. Main tunnels. View of the underwater section: km. 2+840 – 2+450 (starting from the South-West) (Autostrade per l'Italia, 2021)

In the next stretch, approximately 950 m long, the route passes beneath the Levante port area. The altitude of the ground level remains constant at approximately 3.5 m above sea level, as do the tunnel cover whichs stand at approximately 25-26 m, with a rock roof, Calcari del Monte Antola, of approximately 10-12 m. The two entrance halls are located in the middle of this section. In the remaining stretch of 1492 m, up to the eastern entrance of Viale Brigate Partigiane, the coverage remains rather high. Moreover, the route passes by the site of the future New Galliera Hospital; in this area the route was defined altimetrically in order to avoid interference with the foundations of the new building.

In summary, the overall length of the main tunnels is approximately 3420 m per tube. The section for traditional excavation aimed for the emergency pedestrian

by-pass will have a polycentric internal shape, while it will be circular in the case of mechanized excavation as illustrated in Figure 14.

With regard to the satisfaction of the technical requirements, the infrastructure is classified as an urban road (type D) with two separate carriageways, with a total width of 11.25 m, with two travel lanes and an emergency lane as regulated by Ministerial Decree 5/11/01. Each tube is in fact equipped with two lanes (3.25 m overtaking lane, 3.50 m driving lane), as well as a third lane, 3.50 m wide that becomes an emergency lane. The 0.50 m side shoulders are added to the lanes. The paved road platform, without prejudice to the widenings for visibility when cornering, is therefore 11.25 m for each carriageway. In accordance with the traffic components allowed to circulate in the tunnel, the platform does not include the insertion of sidewalks.

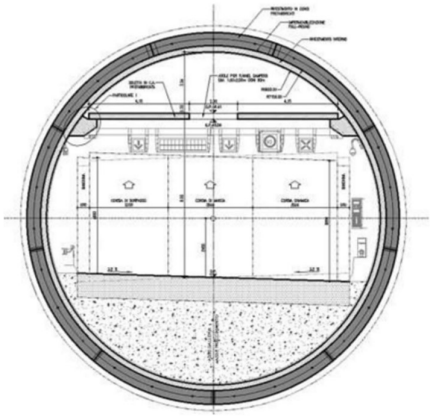

Figure 14. Cross section of the tunnel (Autostrade per l'Italia, 2021)

3.2.2 Geotechnical characterization

Within this section, the geotechnical characteristics and parameters of the geotechnical units interfering with the work in question are analysed. The geotechnical characterization was conducted by the designers on the basis of the results of the tests carried out both on site and in the laboratory as part of four investigation campaigns to which reference was made in the geotechnical report by Autostrade per l'Italia (2021). Additionally, they are a result of the designer's experience in similar contexts in neighboring areas.

The granular soils and lithoid limestone present in the area affected by the work have been divided into the lithostratigraphic units outlined in Table 1. It must be

remarked that only the geotechnical units that surround the tunnel lining as can be seen in Figure 15 are taken into account.

Table 1. Geotechnical Units – Genova Subport Tunnel

Geotechnical Unit Symbol	Geotechnical Unit Name	Description
MS	Marine sediments	Alternation of weakly thickened silty sands, clayey sands and sandy clays. With reference to the 2003 investigation campaign, the local presence of cemented lenses near the coastline was also found, particularly in the central area of the port arch, near the Principe railway station.
ORV	Ortovero Clays	Clayey marl with the presence of layers of compact, overconsolidated clayey-sandy silt and with the dispersed presence of sandy-gravelly levels
FAN	Monte Antola	Located on the roof of the pitched building outcropping in the area under consideration and is interpreted as an expression of the Ligurian - Piedmontese oceanic basin and its transition to the continental margin of the Adria plate. It is characterized by the presence of a compact limestone with occasional levels of calcareous argillite. Several meters at the top of the stratigraphic unit are altered and strongly fractured. In the gossans there are open joints with clay fill. The rock mass is characterized by the widespread presence of closed joints filled with calcite.

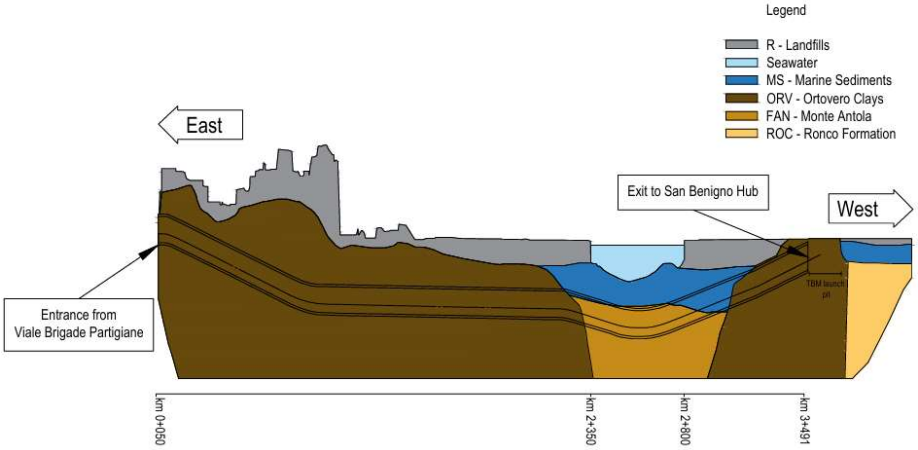

Figure 15. Geotechnical longitudinal profile of the natural tunnel (Autostrade per l'Italia, 2022)

Furthermore, the characteristic geotechnical parameters of the geotechnical units involved in the construction of the planned work are summarized in Table 2, which is the result of the analysis of the data collected during the survey campaigns considered in this work.

Table 2. Geotechnical parameters from previous investigations (Autostrade per l'Italia, 2021)

Geotechnical Unit	γ [kN/m^3]	e_0	OCR [-]	c_u [kPa]	c' [kPa]	ϕ' [°]	UCS [MPa]	E [MPa]	υ	k [m/s]
Marine sediments CL: clayey silts SM: Silty sands	19	-	CL: 2 SM: -	CL: 5+2.5*z SM: 0	CL: 10 SM: 0	CL: 26 SM: 35	-	CL: 10 SM: 40	0.15	10^{-5}-10^{-6} sandy fraction 10^{-6}-10^{-7} cohesive fraction
Ortovero Clays	19.5	0.67	2-4	250	10-15	30	-	40	0.4	10^{-7}-10^{-8}
Monte Antola Unit	26	-	-	-	86-280	43-57	27-40	1000-2000	0.25	10^{-6}-10^{-7}

Furthermore, the geomechanical parameters assumed corresponding to the characterization of the Monte Antola geotechnical unit is included in Table 3.

Table 3. Geomechanical parameters – Monte Antola Unit, FAN (Autostrade per l'Italia, 2021)

Geomechanical parameter	Intact rock	Fractured rock
γ [kN/m^3]	26-27	26-27
GSI [-]	40	40
σ_c [MPa]	30	30
m_i [-]	8	8
Disturbance D [-]	0.5	1
E (rock sample)	40	40
ϕ_{mass} [°]	60 for σ'_n = 50 kPa 55 for σ'_n = 100 kPa 50 for σ'_n = 200 kPa 45 for σ'_n = 300 kPa 40 for σ'_n = 100 kPa	45 for σ'_n = 50 kPa 45 for σ'_n = 100 kPa 40 for σ'_n = 200 kPa 35 for σ'_n = 300 kPa 30 for σ'_n = 100 kPa
c_{mass} [kPa]	70 for σ'_n = 50 kPa 80 for σ'_n = 100 kPa 100 for σ'_n = 200 kPa 130 for σ'_n = 300 kPa 145 for σ'_n = 100 kPa	35 for σ'_n = 50 kPa 40 for σ'_n = 100 kPa 60 for σ'_n = 200 kPa 75 for σ'_n = 300 kPa 85 for σ'_n = 100 kPa
E_{op} [MPa]	3000	1600

3.2.3 Geothermal framework

Similarly to the geotechnical characterization, the geothermal properties relating to the granular soils and rock formations present in the area affected by the work have been divided based on the main component of the engineering description of the lithostratigraphic units described in section 3.2.2. In this context, the literature was consulted in order to provide an order of magnitude for the properties described in Table 4 (Kumar, 2007; Zeng, et al., 2017; Tansel, 2023; Goto & Matsubayashi, 2009; Opreanu, 2003; LaRowe, et al., 2017; Eswara, et al., 2022; Robertson, 1988; Meng, et al., 2020; Dalla Santa, et al., 2020).

Table 4. Summary of the geothermal properties for each Geotechnical Unit of the Genova tunnel

Geotechnical Unit	Thermal conductivity, λ [W/mK]	Specific heat capacity, c_p [kJ/kgK]	Porosity [-]
MS - Marine sediments	CL: 0.25-1.52 SM: 1.2-2.25	CL: 0.69-0.97 SM: 1.30-1.93	0.3-0.75
ORV - Ortovero Clays	1.78-2.90	0.88-0.96	0.05-0.3
FAN - Monte Antola Unit: limestone	0.6-5.01	0.8-0.9	< 0.05

Furthermore, due to the geothermal activation of the tunnel the vertical profile of the seawater temperature in the port of Genova must be defined. For this purpose, the database of the Regional marine ecosystem monitoring network pursuant to Legislative Decree 152/06 was consulted. Figure 16 contains the location of the four stations that were taken into account for the data acquisition of the seawater temperatures and that are listed below.

- Genova - Antistante diga foranea aeroporto 980 m.
- Genova - Antistante foce t.varenna 1700 m.

- Genova - Punta vagno Levante foce Bisagno 1200 m.
- Genova - voltri antistante foce Leira 2100 m.

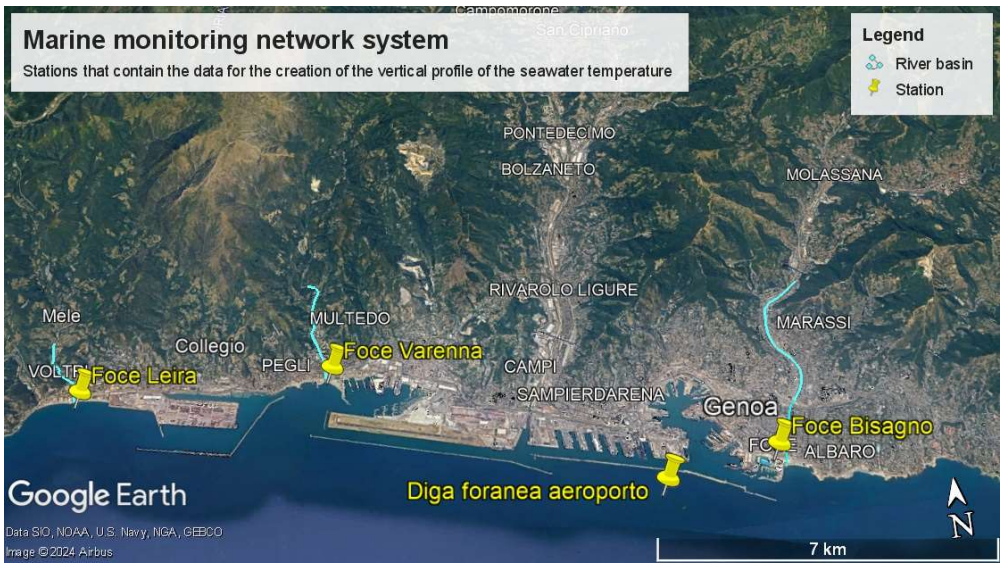

Figure 16. Geographical location of the marine monitoring network stations in the area of the port of Genova

The measurements were carried out in different months from the year 2023. Furthermore, the data from each station was processed with the aim of estimating the average seawater temperature every one meter of depth up to 50 m as shown in Figure 17, where each line represents a different month of the year.

Furthermore, the graph makes the distinction between two seasons of the year: winter and summer. Winter, which encompasses the month of January, March and December, is represented by different shades of blue. Conversely, summer, which involves the months of June, August and October, is depicted with different shades of red. It can be seen that the seawater temperature during the winter months of January and March is nearly constant through the total depth of 50 m with a value equal to 14 °C. For the month of December, temperatures slightly above 15 °C are observed, reaching nearly 17 °C at the maximum depth.

On the other hand, the evolution of the seawater temperature with depth during summer is characterized by an asymptotic shape as portrayed in Figure 17. Temperature at the surface ranges between 23 to 26 °C, arriving to a roughly constant temperature varying between 15 to 16 °C at a depth equal to 50 m.

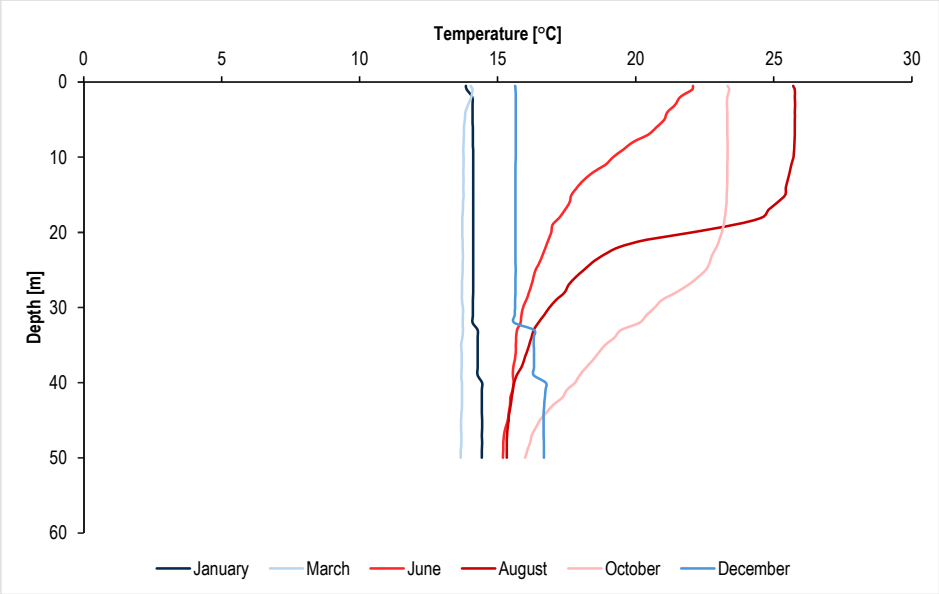

Figure 17. Vertical profile of the seawater temperature for different months of the year 2023.

Conversely, the annual average air temperature for the city of Genova was derived from the ARPA Liguria database. Specifically, the meteorological station "Genova – Centro Funzionale" was utilized due to its proximity to the project site, since it is located in the Foce district as shown in Figure 18. Another significant factor is the extensive dataset it provides, containing information from at least 2019 onwards concerning the average air temperature for the port of Genova. This is of utmost importance and will be further explained in Chapter 4 and 5 of this Thesis.

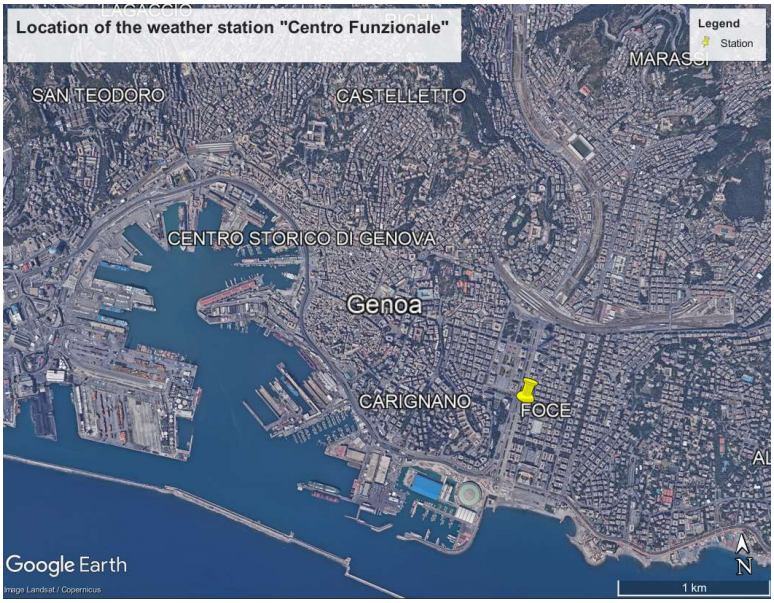

Figure 18. Satellital view of the location of the ''Genova - Centro Funzionale''

As a result, Figure 19 depicts the average air temperature in the city of Genova for the year 2023, resulting in an annual average of 18.3 °C was obtained. This data is crucial for determining the ground temperature, which is a key parameter for estimating the thermal power that can be extracted or injected.

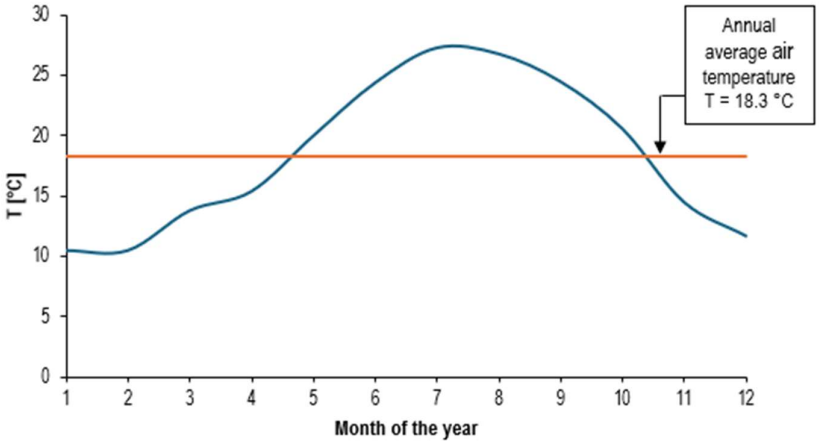

Figure 19. Average monthly temperature in Genova in 2023

3.2.4 Hydrogeological framework

The general structure assumed by the most present aquifer rocks (limestones of Mount Antola) in the sector underlying the intervention is homoclinal with dip towards the East (inclination value equal to approximately 50%). This structure produces, at a regional level, a flow of underground water towards the east (Autostrade per l'Italia, 2021). However, it is believed that in the intervention sector (Genoa amphitheatre) the flows and flow directions of underground water are mainly regulated by the local conditions imposed by the topography of the area whose high gradients establish a local flow regime controlled by the topography. The hydrographic basin underlying the intervention is therefore taken as a reference for underground water circulation. In the river basin there are:

- the clays of Ortovero, which can be considered, on a large scale, characterized by waterproof behaviour;
- the limestones of Mount Antola, permeable due to the presence of cracking and little karstification;
- the formation of Ronco, poorly permeable.

The tunnel construction directly involves the lithotypes described in chapter 3.2.2. The description of the types of permeability and the indicative values are shown in Table 5. However, it must be underlined that within the marly limestones there may be brecciated levels, especially in correspondence with the faulted area of contact with the Ortovero Clays, in which it is possible to find higher permeability values. Furthermore, for the Ortovero Clays it is highlighted that there is a significant difference in terms of permeability between large scale and local scale: in the latter case these can be considered almost impermeable, while in the former case the permeability is greater due to the local presence of permeable sandy and gravelly lenses.

Table 5. Summary of the hydrogeological characteristics

Geotechnical Unit Name	Classification	Type of permeability	Permeability [m/s]	Notes
Monte Antola	Rock	Cracking and mild karstism	10^{-6}-10^{-7}	In correspondence with fractured zones it can rise by several orders of magnitude
Ortovero Clays	OC clays	Practically impermeable	10^{-6}-10^{-8}	There are, especially at the base of the formation, thin permeable sandy and gravelly levels
Marine deposits	Loose sandy loamy soils	Porosity	~10^{-3}-10^{-5} (sandy levels) ~10^{-5}-10^{-7} (cohesive levels)	Mainly sandy clayey silts or silty sand; gravel levels present

3.3 Trento ring road tunnel

3.3.1 Description of the chosen project solution

The area covered by this case study is located in the territory of the Autonomous Province of Trento; more specifically, the railway route extends between the town of Mattarello (Acquaviva) and the north-western part of the city of Trento (Ex scalo Filzi area). The planned works partially concern the F. Adige valley floor (open-air sections and artificial tunnel) and largely concern, in the tunnel, the left hydrographic side of the Adige Valley. Figure 20 shows the geographical location of the project route.

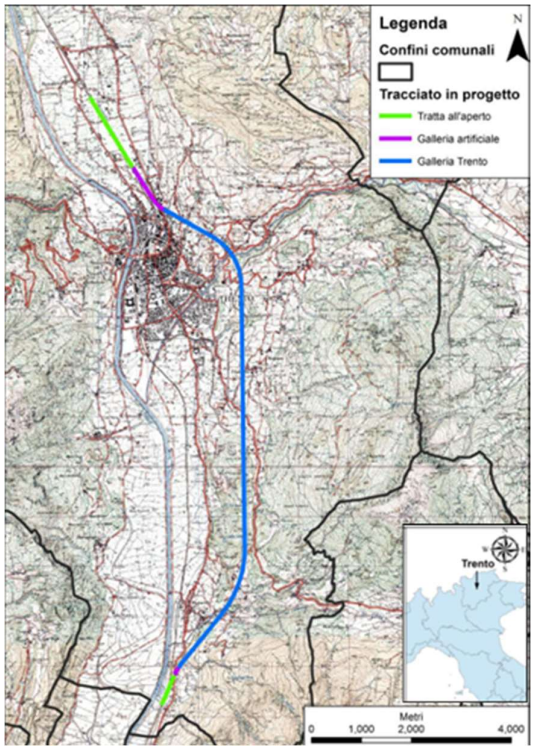

Figure 20. Geographical framework of the study area. (Rete Ferroviaria Italiana, 2021)

According to the Municipality of Trento (2021), the new Brenner base tunnel makes it necessary to upgrade the railway in the section between Verona and Fortezza.

There are four priority lots within this section, including lot 3 of the Trento ring road: this is a railway ring road dedicated to goods which will bypass the urban center in the tunnel under the eastern hill. RFI (Italian railway network), responsible for the design, has already developed various design hypotheses since 2003. In 2018 the signing of a memorandum of understanding between the Province, the Municipality of Trento and RFI gave a concrete impulse to the advancement of the studies.

The railway ring road opens up the possibility of thinking about an even more ambitious project for the city of Trento: it is an "integrated project" which includes, in addition to the freight bypass, the burial of the historic railway line for a stretch of 2.5 km in the urban centre, the simultaneous creation of a rapid connection system between the north and south of Trento and the underground station. The integrated project, still in the feasibility study phase, involves the tramway between

Trento north and the center (also necessary to make up for the interruption of the Trento Malè) and the NorduS project (as an upgrade of the Trento-Malé railway), which are being developed (Municipality of Trento, 2021).

3.2.1.1 Summary of the main works

In accordance with Rete Ferroviaria Italiana (2022), the integrated project with the burial of the historic line in Trento is planned to be implemented in three phases:

- Lot A: this phase includes the construction of the bypass line, which will allow the rerouting of freight traffic and reduce the impact on the city center.
- Lot B: this phase involves the burial of the historic line and the construction of a new underground station. This phase is considered a key aspect of the project, as it will allow for the redevelopment of the city center and the integration of the railway infrastructure with the urban fabric.
- Lot C: this phase includes the development of the North-South connection, which will improve the connection between the city and the surrounding areas.

The section of the ring road tunnel is the same as that adopted for the line tunnels of the project of lot 1 (Fortezza-Ponte Gardena). It is circular with a radius of 4.20 m and develops a free area of about 48.60 m^2 (Figure 21).

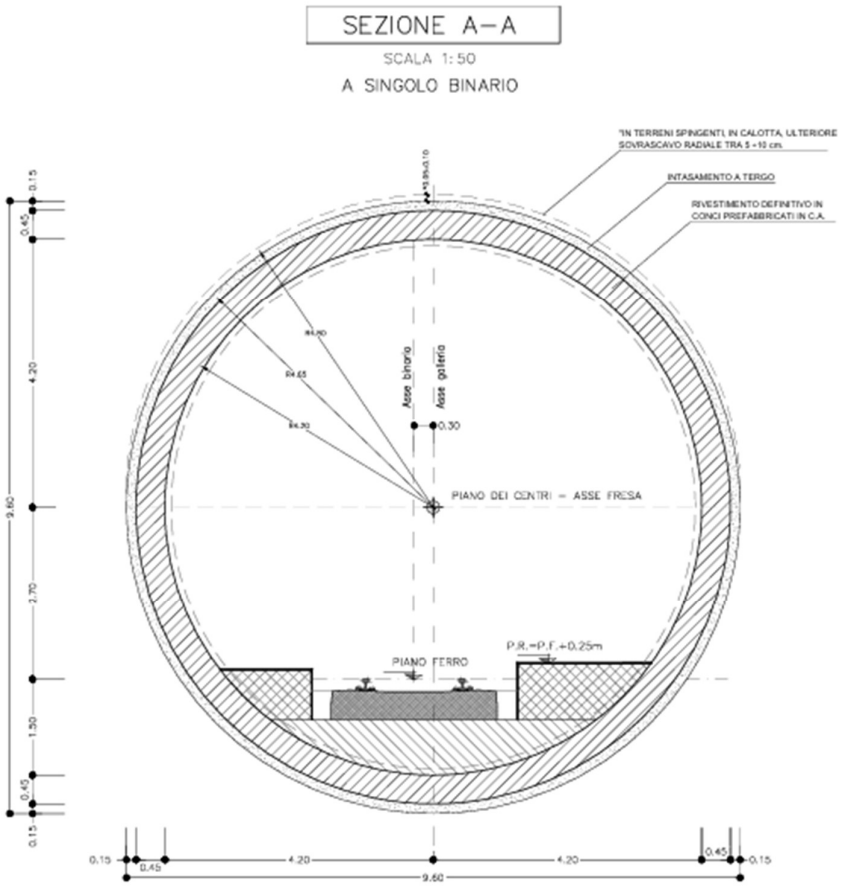

Figure 21. Cross section of the Trento ring road tunnel (Italferr, 2021)

Figure 22. Location of the project and route of the railway line (RFI S.p.a. Direzione investimenti Area Nord Est, 2022)

Starting from the south, the route of the Trento ring road originates in the Acquaviva area (Figure 22), shortly after the SS12 railway overpass, in the

municipality of Trento. The route runs along the current railway site for approximately 400 m and then continues in the tunnel at its intersection with Via Nazionale through an artificial tunnel built outdoors in reinforced concrete, from which the new natural railway tunnel will begin.

The central part of the route develops entirely in a tunnel for a total length of approximately 10.65 km. The tunnel consists of two separate tubes with a bypass every 500 m as required by the legislation on tunnel safety and a maximum separation of 40 m. To reduce execution times, the excavation will be carried out using four TBMs (Tunnel Boring Machines) that will work simultaneously.

At the end of the natural tunnel, the route re-emerges on the surface through the artificial tunnel in the Scalo Filzi area. The latter is crossed at the head by the new section of the Malvasia canal, by via del Brennero and by the new site of the Lavisotto canal. In this section, the construction of an artificial tunnel is planned which will pass under the Via Nassiryia railway overpass. The track height remains at a depth of approximately 10 m from ground level, until the line passes under the existing railway overpass; from here it proceeds in constant ascent for approximately 850 m, where it becomes coplanar with both the historical line and the Trento Malè.

3.3.2 Geotechnical characterization

The geotechnical profile and properties of the ground crossed by the Trento ring road are derived from the documentation provided by Rete Ferroviaria Italiana (2021). The tunnel crosses several lithostratigraphic units as portrayed in Figure 23. Those considered in the analysis and of interest are thoroughly described in Table 6.

The identification of the type of material, and therefore the choice of the interpretation method, was made mainly on the basis of the stratigraphic description of the boreholes and the indications extracted from the geological report by Rete Ferroviaria Italiana (RFI).

Table 6. Geotechnical Units – Trento ring road tunnel (Italferr, 2021)

Geotechnical Unit symbol	Geotechnical Unit name	Description

PTG	Post-glacial alpine system	Polygenic gravels with sand and sandy, locally silty
ZW	Zwischenbildungen Unit	It includes, indistinctly, the Dark Limestones of Margon, Marl of Val di Centa, Buchestein and Limestones of Val Vela. It includes dark bituminous limestone (at the base), densely stratified limestone and marl, and clay layers.
TVZ	Travenanzes Formation	Light grey, yellowish dolomite with a very fine grain, in decimetric layers, separated by thin intercalations of greenish marl.
DPR	Main Dolomite	Fossil-clear stromatolitic dolomites, oolitic doloarenites, in decimetric to metric layers.
GIV3	Giovo Formation	Layered greyish and whitish limestones and dolomites, interspersed with thin layers of grey pelites laminated with quartz and muscovite.
WER	Werfen Formation	Werfen indistinct formation, consisting of a succession of carbonate, terrigenous, and mixed sediments. Alternations of limestone, dolomite, siltstone sandstone and marl.
BEL	Bellerophon Formation	Silty grey-yellowish dolomites and dark grey silty limestones compact in predominantly nodular layers, alternating with sandstones and grey siltstones and marls with carbonaceous horizons.
GAR	Sandstone of Val Gardena	Red, grey, greenish and white sandstones poorly compacted, alternating with red, green or grey siltstones, marly siltstones and marls.
ICT	Castelliere Formation	Grey, grey-green and reddish-grey rhyodacitic tuff lapilli; frequent levels of fine laminated tuff (surge) and tuff breccia at abundant lythic and inclusion. Locally there are small domes of dacite lava (F. di Pinè) included in the banks.
ICTc	Castelliere Formation	Local presence of epilastites (ICTc) given by dacitic and rhyodacitic clast conglomerates.
LUB	Buss Formation	Highly hydrothermalized, black, gray-green or violet-gray porphyritic andesitic lavas; Massive and

		pseudostratified lavas, associated with lavas with rounded and angular blocks cemented together.
VFS	Quartz phylads and phyllites	Silver-grey fillads, locally with greenish streaks, quartz, sericite/muscovite, chlorite, albite ± biotite and ilmenite. Characterized by a very thin grain and a remarkable fissility parallel to the schistosity planes. White quartz nodules concordant with schistosity are frequent.
ARV	Red ammonite from Verona	At the base, micritic limestones, poorly stratified and with a nodular structure, generally white, pinkish and greenish in colour, sometimes dolomitised. In the intermediate part, well-stratified reddish limestones with frequent intercalations of red flint in beds and ashy levels. In the upper part, red and white nodular limestones with ammonites in very thick layers.
RTZ	Rotzo Formation	Light grey/white to brown bioclastic limestones arranged in sequences of metric to decametric thickness. Decimetric marl levels are present locally. The lower part of the succession contains locally dark laminated clays with very fine grain size.
SAA	Red scaglia	Densely stratified slab-like micritic limestones (red or brick red, flints in the lower part, with marly and marl interlayers.
CHI	Chiusole Formation	Well-stratified micritic limestones with very fine grain size, pinkish and whitish at the base

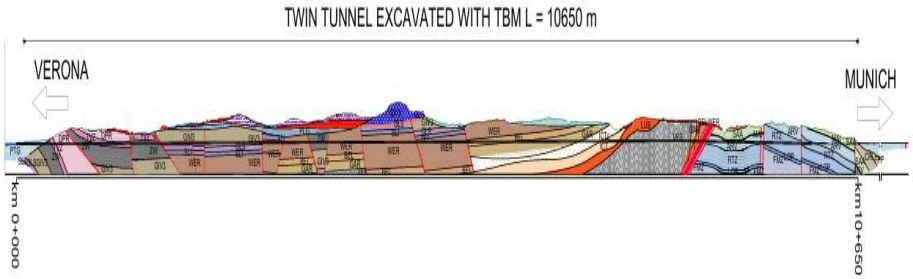

Figure 23. Geotechnical longitudinal profile of Trento ring road tunnel (Italferr, 2021)

In this context, Table 7 outlines the geotechnical parameters for each unit.

Table 7. Summary of the geotechnical parameters according to the geotechnical profile

Geotechnical Unit	γ [kN/m^3]	c' [kPa]	ϕ' [°]	m_i [-]	σ_{ci} [MPa]	GSI [-]
PTG	18	0	32-43	-	-	-
ZW, TVZ	26	-	-	8	30	30-45
DPR	29	-	-	10	90	40-50
GIV3	27	-	-	8	35	40-50
WER, BEL	24	-	-	8	35	40-50
GAR	25	-	-	13	35	30-40
ICT, ICTc	22	-	-	13	20	60-70
LUB	23	-	-	15	80	40-50
VFS	27	-	-	7	35	30-40
ARV	25	-	-	11	40	50-60
RTZ	25	-	-	10	80	50-60
SAA, CHI	24	-	-	8	30	15-20

3.3.3 Geothermal framework

A similar approach to the Genova tunnel was used to characterize the geothermal properties of the granular soils and rock formations present in the area affected by the project. For this purpose, the literature was consulted in order to provide an order of magnitude for the properties outlined in Table 8 (Dalla Santa, et al., 2020; Rao, et al., 2022; Heap et al., 2016; Karu, 2012; Shrestha, 2014). It must be remarked that average values of each geothermal property are computed for geotechnical units composed of more than one type of material. For this purpose, chapter 3.3.2 that highlights the lithological description of each geotechnical unit must be consulted.

Table 8. Summary of the geothermal properties for each G.U of the Trento tunnel

Geotechnical Unit symbol	Thermal conductivity, λ [W/mK]	Specific heat capacity, c_p [kJ/kgK]	Porosity [-]
PTG	0.18-3.00	0.84-1.84	0.21-0.32
ZW	1.19-3.96	0.8-0.9	0.04-0.31
TVZ	0.61-5.73	0.88	0.19-0.33
DPR	0.61-5.73	0.88	0.19-0.33
GIV3	0.61-5.36	0.88	0.13-0.45
WER	0.78-5.04	0.88-0.91	0.12-0.37
BEL	0.78-5.04	0.88-0.91	0.12-0.37
GAR	1.1-3.55	0.85-0.88	0.12-0.32
ICTc	2.0-3.91	0.97-1.0	0.19-0.32
ICT	2.0-3.91	0.97-1.0	0.19-0.32
LUB	0.64-4.86	0.81-0.88	0.08
VFS	1.5-3.33	0.51-0.69	0.01
ARV	0.6-5.01	0.8-0.9	0.07-0.56
RTZ	1.19-3.96	0.8-0.9	0.04-0.31
SAA	0.6-5.01	0.8-0.9	0.04-0.31
CHI	1.19-3.96	0.8-0.9	0.04-0.31

Regarding the monthly air average temperature in the city of Trento for the year 2023, the same approach was followed as for the Genova case study. Average

temperature values were obtained for each month from the Meteotrentino database. Figure 24 illustrates the temperature trend throughout the year, highlighting the annual average air temperature of 13.75 °C.

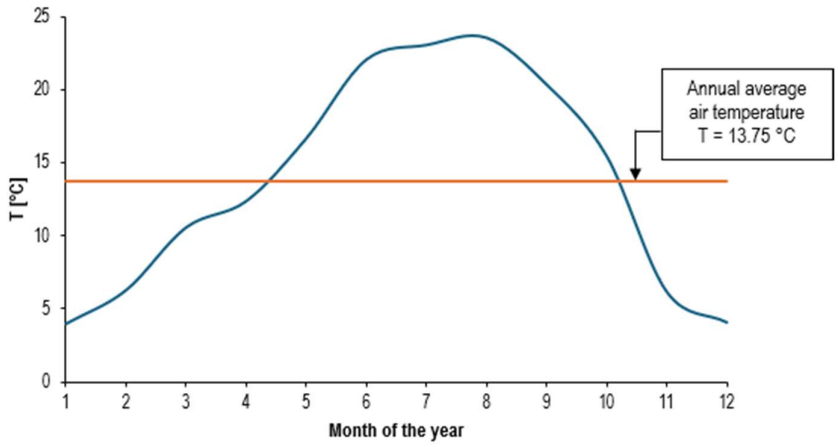

Figure 24. Monthly average air temperature in the city of Trento. 2023

3.4.3 Hydrogeological framework

The area under study is part of the geological context relating to the Southern Alpine Domain. The planned railway route is located in the reliefs on the left Adige and crosses, along its route, geological units made up of phylladic, volcanic metamorphic rocks (linked to Adige magmatism), and sedimentary rocks made up of both terrigenous and calcareous dolomites. In addition to the aforementioned units, the route crosses Quaternary alluvial and slope deposits in the Acquaviva and Trento areas.

The hydrogeological characteristics of the different units are linked to the lithology of the soils and rocks (Figure 25) induced by the tectonic phenomena that affected the study area. A further factor that can significantly influence the hydrogeological characteristics of the units is given by the karstification of the lithotypes. Karst phenomena are more conceivable, along the main faults, in the limestone successions (Grey Limestone group) and, subordinately, in the dolomitic successions (Main Dolomite). Terrigenous formations, which are more easily altered, tend to have lower mass permeability (fractures filled with fine materials).

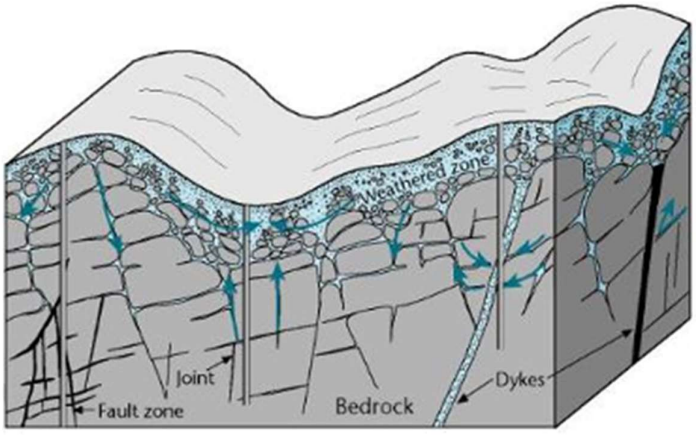

Figure 25. Conceptual diagram of a fractured rock mass (hard rock aquifer) (Rete Ferroviaria Italiana, 2021)

The hydrogeological map is reproduced in a synthetic and simplified form in Figure 26. It can be seen that the tunnel's chainage is surrounded by geological formations with medium to high permeability, represented with blue and turquoise respectively

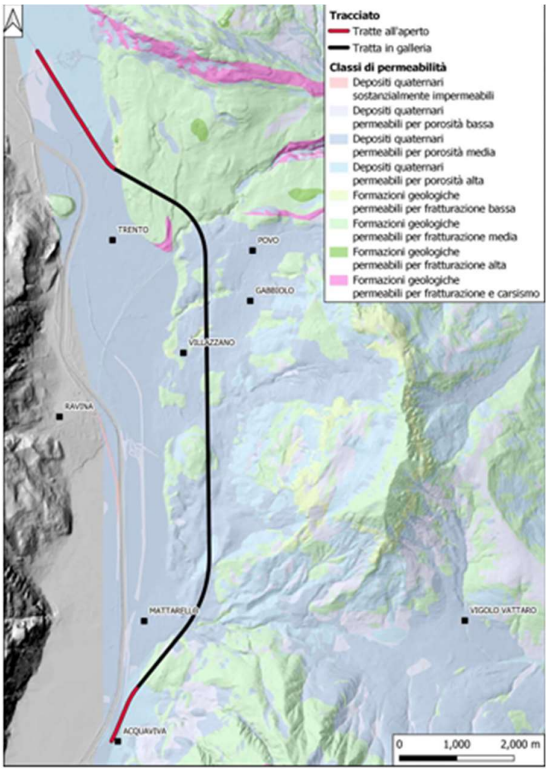

Figure 26. Simplified representation of the hydrogeological map with only the indication of permeability. (Rete Ferroviaria Italiana, 2021)

Moreover, Figure 27 illustrates the four river basins of interest from south to north:

- Valsorda-Marzola;
- Fersina Sud;
- Fersina Nord;
- Trento.

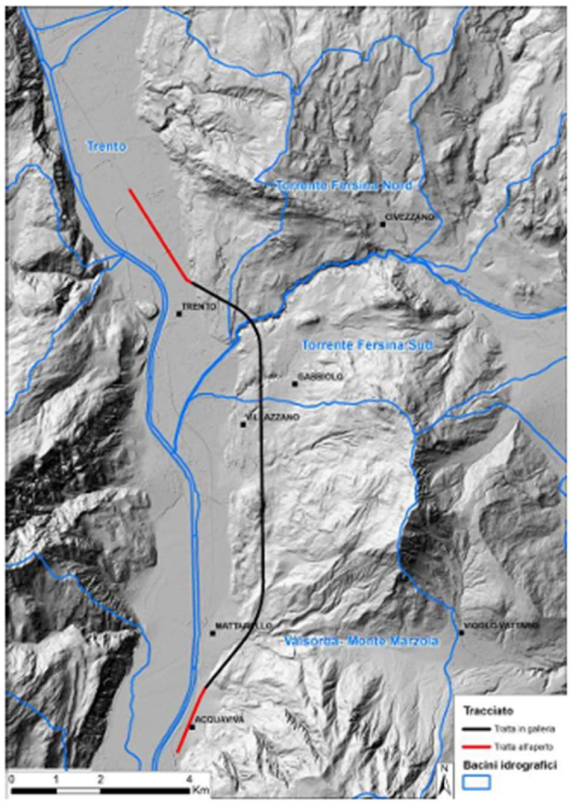

Figure 27. Definition of the main river basins present in the area

The description of the types of permeability and the indicative values for each geotechnical unit described in chapter 3.3.2 are shown in Table 9. It must be remarked that the values of the hydraulic conductivity of the materials that compose each lithological unit were derived from the literature and then averaged in order to obtain a representative value due to the heterogeneous composition of some geotechnical units. (Karu, 2012; Duffield, 2019).

Table 9. Hydraulic conductivity ranges for each geotechnical unit in the Trento tunnel

Geotechnical Unit symbol	k [m/s]
PTG	$9.4x10^{-4}$-$2.3x10^{-3}$
ZW	$5.47x10^{-8}$-$4.7x10^{-3}$

TVZ	$1x10\text{-}9^{-6}x10^{-6}$
DPR	$1x10\text{-}9^{-6}x10^{-6}$
GIV3	$5.2x10^{-9}$- $4.7x10^{-3}$
WER	$9.62x10^{-7}$- $1.93x10^{-3}$
BEL	$9.62x10^{-7}$- $1.93x10^{-3}$
GAR	$1.6x10^{-6}$- $7.67x10^{-5}$
ICT	$1x10^{-9}$-$1x10^{-11}$
ICTc	$1x10^{-9}$-$1x10^{-11}$
LUB	$1x10^{-10}$-$1x10^{-12}$
VFS	$1x10^{-9}$-$1x10^{-11}$
ARV	$9.4x10^{-9}$- $9.4x10^{-3}$
RTZ	$5.47x10^{-8}$- $4.7x10^{-3}$
SAA	$5.47x10^{-8}$- $4.7x10^{-3}$
CHI	$5.47x10^{-8}$- $4.7x10^{-3}$

3.4 Cortina D'Ampezzo tunnel

3.4.1 Description of the chosen project solution

The Cortina Variant is divided into 2 Lots); more specifically, the project includes a first phase which provides an infrastructure for the "improvement of the access road to the town of Cortina". The implementation of this intervention is planned in relation to the international event of the "Milan-Cortina 2026" Winter Olympic Games, which will be held in the famous Ampezzo resort, and which constitute an important opportunity for further tourism development in the area.

The second functional section, the so-called "by-pass of the town of Cortina", is the main and final part of the implementation of the entire intervention. Its objective is to create a bypass to the town, currently crossed by both the S.S. 51 "di Alemagna" and the S.S. 48 "delle Dolomiti" as seen in Figure 28.

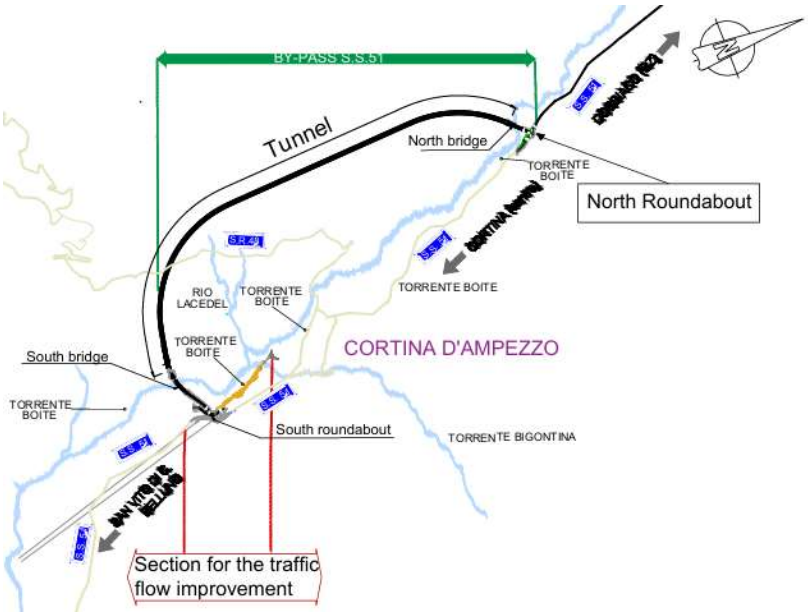

Figure 28. Framework of the intervention in the town of Cortina d'Ampezzo. Functional excerpts (Anas Gruppo FS Italiane, 2023)

The current configuration of the infrastructure of the S.S 51 involves considerable criticalities on the city's road network with situations of high congestion of vehicular traffic and consequent disturbances in terms of noise and air pollution, with impacts both for the resident population and for the tourism and service sector, which mainly contributes to the economic productivity of the entire

area. In this context, the issue of the crossing of the urban center by heavy vehicles is particularly critical, which, in large numbers, prefer the use of the S.S. 51 for the north-south routes between Italy and Austria.

3.4.1.1 Summary of the main works

The project intervention relating to Lot 1 involves the construction of a section for the traffic flow improvement whose route, 775 m long, starts from the intersection between the State Road 51 of Alemagna and Via Guide Alpine and ends at Via dei Campi (near the Cemetery) as illustrated in Figure 28. The new road axis develops mainly outdoors and for 275 m in an artificial tunnel.

The Cortina By-pass (second Functional Section) consists of a road axis, mainly in tunnels, with a length of nearly 5.5 km. The main work of the Lot is the tunnel consisting of two separate tubes with a total length of almost 4700 m and a diameter of 11.25 m (Figure 29). The tunnels are going to be excavated by means of a TBM and will be located at a variable depth with a maximum cover of about 250 m. The route starts at the south roundabout at the junction with the SS51 at Via delle Guide Alpine and ends in the north just beyond the locality of Cadin di sopra, with the North roundabout as illustrated in Figure 28.

For the standard section, an innovative solution is planned to be adopted that consists of one carriageway with a lane of 3.75 m with shoulders widened to 3.00 m on the right and an additional shoulder of 0.50 m on the overtaking side. These carriageways are generally flanked in the embankment/trench sections and separated by a jersey-type barrier, and then separate near the entrances to the tunnel where they proceed along two independent arches connected by by-passes.

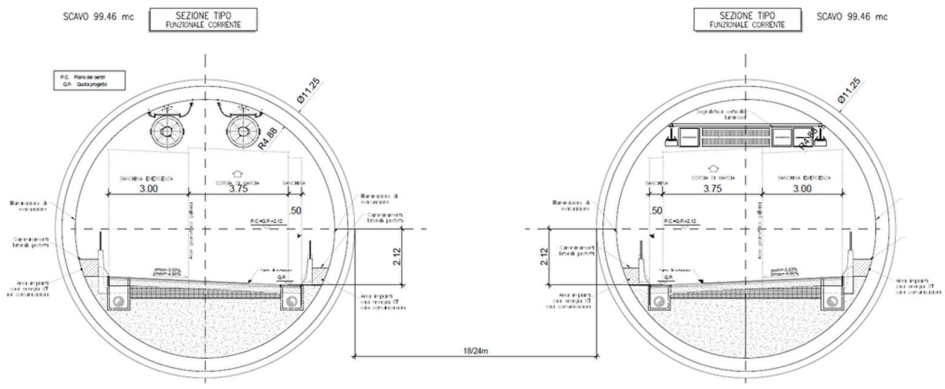

Figure 29. Section with double one-way arch and platform (Anas Gruppo FS Italiane, 2023)

3.4.2 Geotechnical characterization

The geotechnical characterization is based on the geotechnical report that refers to Lot 2 (second functional excerpt) of the larger intervention of the Cortina Variant present in document T02GE04CETRE01; more specifically, the so-called "by-pass of the town of Cortina" is described, which constitutes the main part, in terms of complexity, and conclusive of the implementation of the entire intervention.

The definition of the subsurface geotechnical model is shown in Figure 30, Figure 31, Figure 32 and Figure 33. This model has been defined with reference to the geological model included in the technical reports developed by Anas Gruppo FS Italiane (2023), considering the stratigraphic, structural, hydrogeological and geomorphological aspects identified. In addition, all the available data (geological survey, results of on-site and laboratory investigations, groundwater survey) was analyzed by the designers of the company for the definition of homogeneous units from a physical-mechanical point of view, of the regime of interstitial pressures and of the characteristic values of the geotechnical parameters. For the purpose of sizing the works, four geotechnical units can be identified which are illustrated in Figure 30 to Figure 33 and described in Table 10.

Table 10. Geotechnical Units – Cortina bypass tunnel (Anas Gruppo FS Italiane, 2023)

Geotechnical unit symbol	Geotechnical Unit name	Description
UG1a	Clayey silt	Represents the surface blanket consisting of landslide accumulations with indications of recent movements. This unit is mainly characterized by fine-grained silty clayey materials, with sometimes frequent inclusions of gravel, pebbles and blocks of dolomite and calcarenite nature.
UG1b	Lime with clay	Represents the surface blanket consisting of accumulations of landslides and complex landslides with no evidence of recent movements. This unit is mainly characterized by fine-grained silty clayey materials, with sometimes frequent gravel and sandy gravelly lenses.
UG2	Gravel with sand	Represents the surface blanket consisting of accumulations of complex landslides, debris flow deposits, glacial deposits and alluvial deposits. This unit is mainly characterized by coarse-grained materials, consisting of gravels, pebbles and blocks immersed in a sandy to silty matrix.

SC	San Cassiano	Highlighted in orange in the figures below. It is a bedrock unit that underlies many landslide-prone areas in the Dolomite region of northern Italy. is typically composed of plastic clays with inclusions of various sizes, including marls, dolomitic pebbles and cobbles (Frisia Bruni & Wenk, 1985; Bossi, 2015; Menegoni, Inama, Crozi, & Perotti, 2022).
H	Heiligkreuz	Represented in purple in the geotechnical profiles. It is a geological unit that was deposited in the Dolomite region of northern Italy during the Late Triassic period. It is composed of a mixed carbonate-siliciclastic succession, including shales, sandstones, and carbonates (Roghi, et al., 2014; Gattolin, Breda, & Preto, 2013)

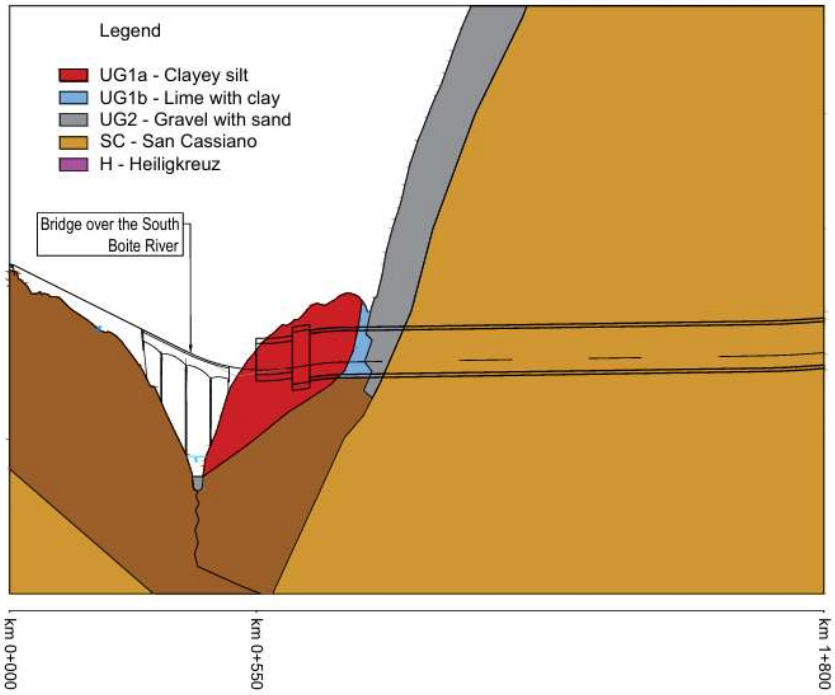

Figure 30. Geotechnical profile North direction 1 of 2 (Anas Gruppo FS Italiane, 2023)

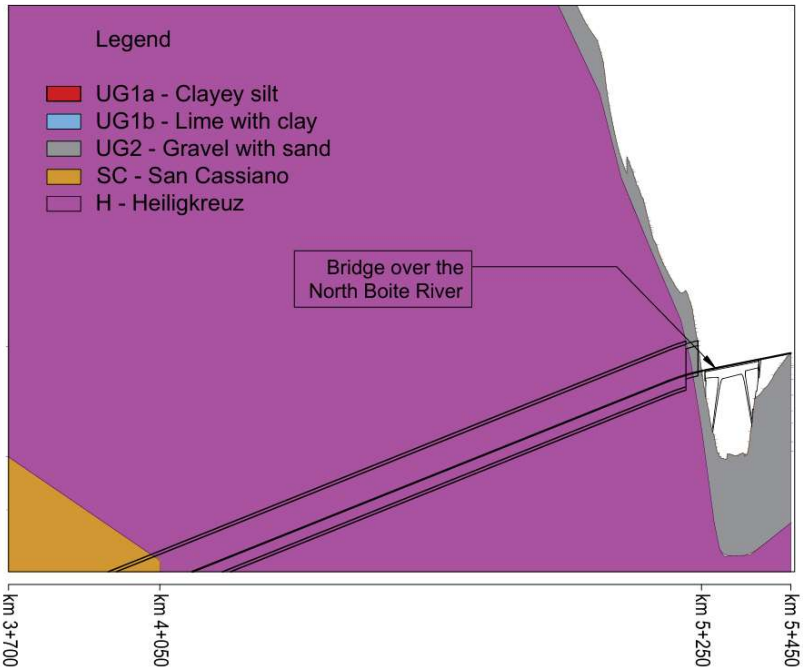

Figure 31. Geotechnical profile North direction 2 of 2 (Anas Gruppo FS Italiane, 2023)

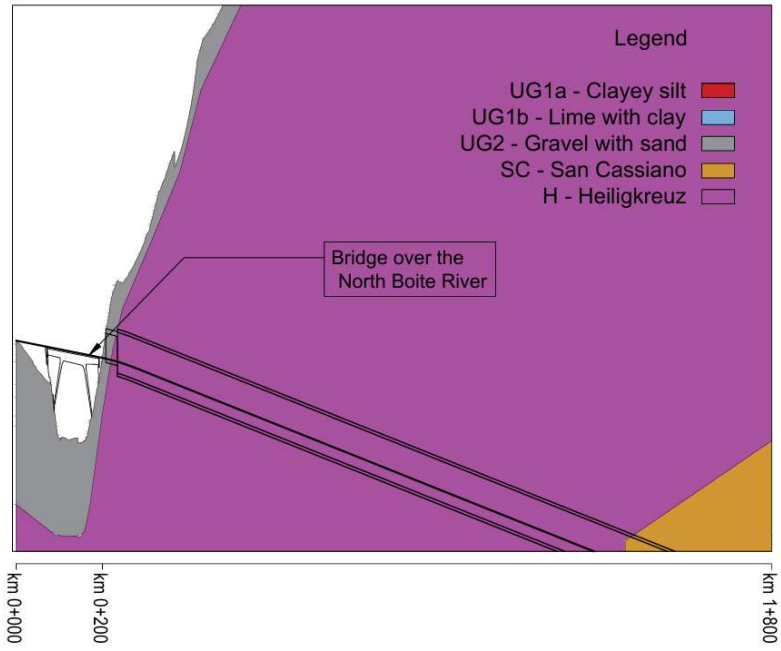

Figure 32. Geotechnical profile South direction 1 of 2 (Anas Gruppo FS Italiane, 2023)

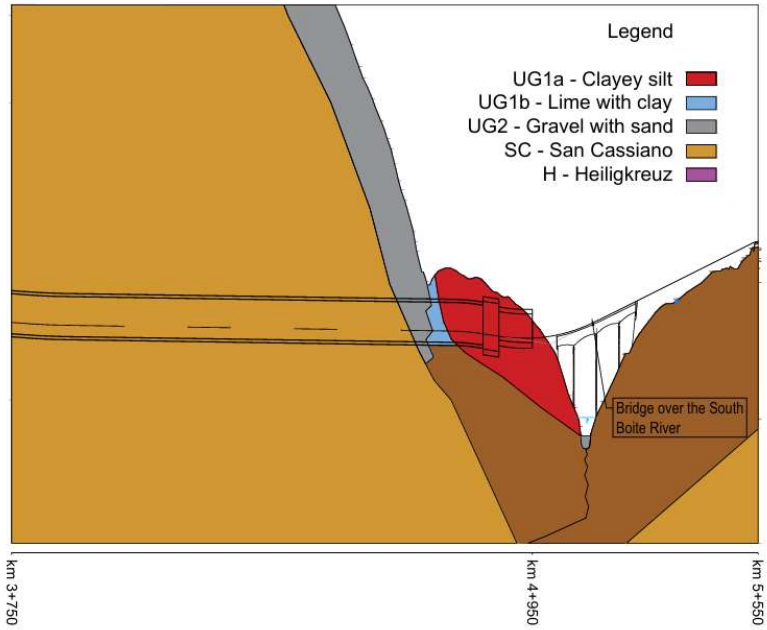

Figure 33. Geotechnical profile South direction 2 of 2 (Anas Gruppo FS Italiane, 2023)

With reference to the previously identified geotechnical units, the physical-mechanical characteristics were defined by the designers who combined the results of laboratory tests and on-site investigations carried out during the various survey campaigns, through correlations proposed in the literature and already widely verified on an experimental level. The characteristic values of the strength and deformability parameters defined for each geotechnical unit are summarized in Table 11.

Table 11. Characteristic geotechnical properties of UG 1a, UG 1b and UG2

Geotechnical Unit	Description	γ [kN/m^3]	c' [kPa]	c_u [kPa]	ϕ' [°]	E [MPa]
UG 1a	Clayey silt	18-20	10-20 0: residual	50-100 for z < 10m 100-200 for z ≥ 10m	22-24 [20-22]: residual	20-60
UG 1b	Silt with clay	18-19	5-10	50-150 for z < 10m 200-400 for z ≥ 10m	24-25	20-50 for z < 25m 50-100 for z ≥ 25m
UG2	Gravel with sand	19-20	0-5	-	30-34	20-50 for z < 10m 50-200 for z ≥ 10m

Furthermore, the geomechanical parameters for the San Cassiano and Heiligkreuz Geotechnical Units are outlined in Table 12.

Table 12. Geomechanical parameters of the San Cassiano and Heiligkreuz geotechnical units

Geotechnical Unit	Description	γ [kN/m^3]	UCS [MPa]	GSI
SC	San Cassiano	24-25	5-20	50
H	Heiligkreuz	24-25	100-150	30-65

3.4.3 Geothermal framework

The geothermal properties, including the thermal conductivity, the specific heat capacity and porosity, of the soil and rock formations present within the project area have been classified according to their engineering description outlined in Table 10. This classification aims to facilitate the identification of zones along the chainage that exhibit similar geothermal characteristics, thereby allowing for the determination of homogeneous sections for the quantification of the geothermal potential. In this context, the literature was consulted in order to provide an order of magnitude for the properties described in Table 13. (Hailemariam & Wuttke, 2022; Mingyi et al., 2018; Nidal, 2003; Geotechdata.info, 2013; You et al., 2021; Ponomaryov & Zakharov, 2021; Dalla Santa et al., 2017; Georgieva, 2016; Amiri et al., 2022; Gregg, 1987; Wisconsin Geological and Natural History Survey, 2024; Andújar Márquez et al., 2016).

Table 13. Summary of geothermal properties – Cortina tunnel

Geotechnical Unit	Thermal conductivity, λ [W/Mk]	Specific heat capacity, c_p [kJ/kgK]	Porosity [-]
UG 1a	0.82-2.60	1.0-1.4	0.72-0.92
UG 1b	0.82-2.60	1.0-1.4	0.72-0.92
UG 2	0.18-3.0	0.84-1.84	0.21-0.32
San Cassiano	1.78-2.90	0.88-0.96	< 0.07
Heiligkreuz	0.61-5.73	0.88	0.02-0.06

Moreover, Figure 34 illustrates the average air temperature at 2 m in the city of Cortina D'Ampezzo throughout the year 2023. For this purpose, the ARPA database of the Veneto region was consulted, where an annual average air temperature equal to 8°C was obtained. This data is critical for defining the ground temperature, which is essential for estimating the thermal power that can be extracted or injected.

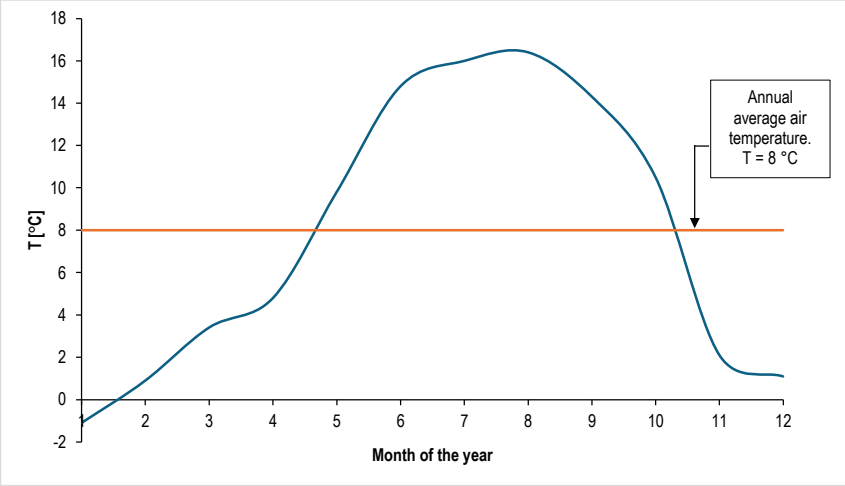

Figure 34. Average monthly temperature in Cortina d'Ampezzo in 2023

3.4.4 Hydrogeological framework

From a hydrographic point of view, the route in question crosses the valley of the Boite stream, which flows in a NS direction on the valley plain, intersecting the axis of the tunnel downstream of Donea at an altitude of 1155 m a.s.l. There are numerous tributaries on the right bank which, however, are concentrated in the localities of Campo di Sopra and Lacedel; these are mainly the Roncato River and the Torgo River, which flow into the Boite at an altitude of 1150 m a.s.l. without intersecting the axis of the route in question.

The shallow (and also deep) lithologies present in the area under examination are made up of predominantly cohesive soils or in any case with a silty and clayey matrix that is generally quite abundant, which makes these soils not very permeable. The presence of soils with poor or very poor permeability does not favour the infiltration of precipitation water, nor does it facilitate a free circulation of water in the subsoil such as to allow the formation of real "aquifers". This obviously does not mean that there is no water in the subsoil. On the contrary, the poor permeability associated with high plasticity makes these soils particularly susceptible to changes in their state of consistency in relation to variations in water content. This circumstance, as is well known, is among the predisposing causes of slow landslides.

Mainly in the initial stretch, near the locality of Donea, there is a further phenomenon that complicates the hydrogeological scheme of the area. In fact, the

presence of layers, lenses and bulky bodies of gravels (with blocks), even if immersed in a silty-clayey matrix, favors the circulation of water in relatively permeable bodies "confined" by poorly permeable materials. Since the supply of these confined "hydraulic bodies" takes place at very high altitudes, the presence of pressurized aquifers often occurs, with piezometric levels that can be even higher than those of the topographic surface, thus favoring gravitational movements. This circumstance is indicated by some piezometric data acquired in the surrounding areas. This situation is also one of the reasons for the presence of ephemeral springs, linked to the circulation of water within the relatively more permeable bodies, but also due to circumstances related to the movement of earth flows. During periods of greater meteoric precipitation, various water emergencies are reported in the landslide bodies.

In the area at the foot of the Pocol relief and in the northern portion of the route, between the Belvedere ridge and the Boite stream, the hydrogeological structure is very complex due to numerous factors. On the surface, the coarse deposits, which characterize this portion of the slope, prone to underground circulation along preferential routes. Upstream, the morphological location of the Ghedina Lakes and their wetlands make available a continuous supply of water to the underlying deposits, while the tectonic features present, the overthrust in the first place, represent a further element of disturbance and complication to the underground hydrogeological structure.

All these elements, however, do not allow us to determine whether the water inputs that can be recognized on the surface are linked to underground circulations within the deposits or whether they are linked to deeper circulations. The directions of the main tectonic lineaments potentially present may be able to convey large quantities of water downstream from the upstream rock basins.

The hydrogeological structure of the area, as previously mentioned, is largely conditioned by the lithologies present in the different areas involved in the project. The lithological units present in the area have been divided into 4 different types of materials based on the degree of permeability and are described in Table 14.

Table 14. Types of materials based on the degree of permeability. Cortina D'Ampezzo tunnel

Type of soil according to permeability	Description
Soils generally characterized by a low degree of permeability	They represent all the most cohesive lithotypes with abundant clayey silty matrix and scarce coarse inclusions. This group (blue color in Figure 34) includes the landslide accumulations that characterize the entire southern area of the route from km 0 to 800 and from 1260 to 3260. The presence of fine-grained materials, at least in the superficial portions, does not favor the presence of aquifers; However, the chaotic structure could facilitate the presence of water circulations inside lenses, even very large ones, of medium-coarse-grained materials that are moderately permeable.
Soils generally characterized by a medium-low degree of permeability	This class includes glacial deposits and eluvio-colluvial deposits (light purple color in Figure 34). Also in this case, the permeability is poor due to the presence of a silty-clayey-sandy matrix that limits water circulation. For this reason, the hydrogeological configuration is very similar to the one described above.
Soils generally characterized by a medium-high degree of permeability	This class includes the coarser soils with poor fine matrix (turquoise region in Figure 34). These are much more prone to the infiltration of rainwater and promote deep water circulation and the development of slope aquifers. Proof of this are the limited portions with difficult water flow. Seepage water tends to flow at the interface between the substrate rocks, which are impermeable or poorly permeable due to cracking, and the highly permeable overlying deposits.
Rocks generally low to medium permeable by cracking	They represent the rocks of the substrate, outcropping mainly in the Belvedere area (dark purple region in Figure 34). The rock, which is very impermeable, can become permeable due to cracking and fracturing and preferential routes of sliding and drainage can develop in depth, representing a possible interference with the work in question. It should be noted, however, that the permeability, even in conditions of intense fracturing, decreases in correspondence with the purely pelitic or marly

levels characteristic of both the formation of San Cassiano and the formation of Heilikgreuz.

In the formation of San Cassiano, the presence of a clayey-marly matrix does not allow the cluster to be defined as a hard rock aquifer but as an aquitard that, locally, can take on the characteristics of a modest aquifer. The permeability tests, carried out inside the boreholes that involved the deposits of this formation, showed practically zero absorption values, consequently the mass can be defined as an aquitard with low permeability and locally an aquifer with very low permeability. An active water circulation can develop only in the cracks, with the ability to sustain small and irregular sources. On a large scale, however, there remains a low-permeability aquitard, which often constitutes the impermeable substrate of extensive coarse debris accumulations of cover that are very permeable due to porosity, consequently conditioning the coming to light of springs.

In the formation of Heilikgreuz the underground water circulation is typical of a hard-rock aquifer, so it is limited only to the portions or bands affected by fracturing or is limited to the mantle of surface alteration, in which a good or fair circulation of water through the fractures present is possible.

Furthermore, the spatial distribution of permeability along the tunnel's chainage, as developed by Anas Gruppo FS Italiane is shown in Figure 35. Soils with low permeability are indicated in blue, with the initial section of the tunnel's chainage falling within this category. Soils exhibiting low to medium degree of permeability are depicted in light purple, whereas turquoise denotes soils ranging from medium to high permeability, mainly observed in the middle and final sections of the chainage. Additionally, dark purple highlights areas with a slight overlap with

the light purple, characterizing rock formations with generally from low to medium permeability due to cracking.

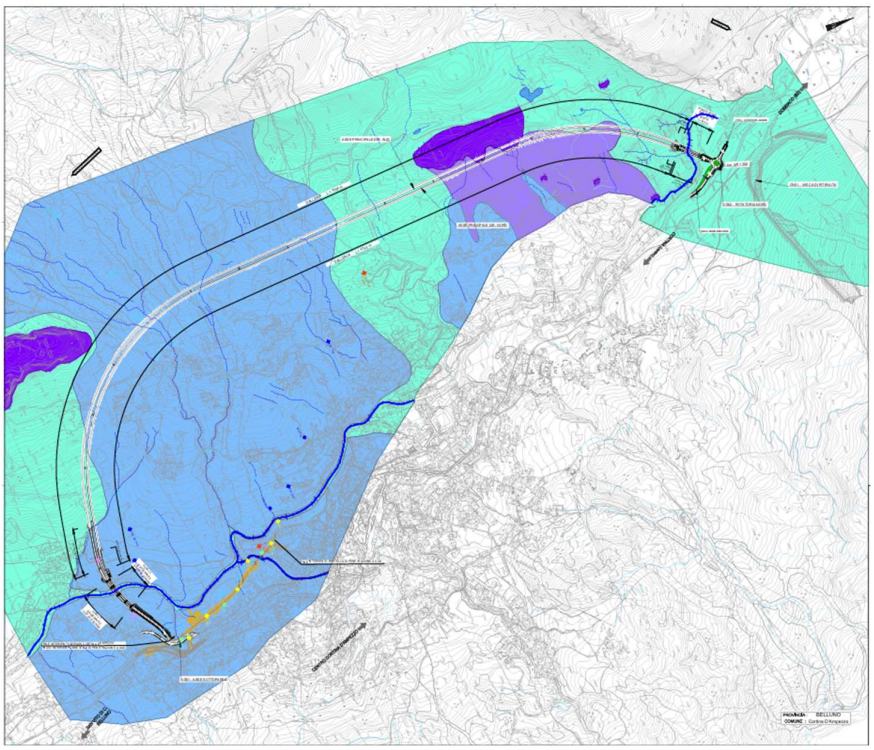

Figure 35. Hydrogeological map (Anas Gruppo FS Italiane, 2023)

Moreover, based on data available in the literature, the permeability values outlined in Table 15 can be considered (Bryant, 2003; Ozcoban et al., 2018; Geotechdata.info, 2013). It must be remarked that for the San Cassiano and Heiligkreuz units the principal component of each lithostratigraphic unit was considered since there is little or non-existent data regarding the characterization of these units.

Table 15. Permeability values of the geotechnical units

Geotechnical Unit	Description	k [m/s]
UG 1a	Clayey silt	$1.42x10^{-5}$-$1.42x10^{-6}$
UG 1b	Silt with clay	$1.1x10^{-7}$-$1.1x10^{-9}$
UG2	Gravel with sand	10^{-6}-10^{-8}
San Cassiano	Dolomite, limestone, arenaceous dolomite	$1.42x10^{-5}$-$1.42x10^{-6}$
Heiligkreuz	Mainly marl and clay	10^{-10}-10^{-5}

Chapter 4

Identification of the homogeneous sections and quantification of the geothermal potential

4.1 Introduction

The present chapter describes the preliminary phase to evaluate the geothermal potential of a tunnel lining, which consists in dividing the line chainage into homogeneous sections characterized by similar features such as the lithology around the tunnel, soil/rock temperature, groundwater velocity, and groundwater flow with respect to the tunnel axis. It must be remarked that the working methodology adopted in this chapter is based on the work carried out by Barla and Insana (2023) and Baralis et al., (2018), where the Turin Metro Line 2 was subjected to a thorough evaluation of the geothermal potential.

Primarily, the work methodology for each tunnel focuses on the creation of two matrices referring to the winter and summer seasons of 2023, as the gathered data from the ARPA databases reflect the annual average air temperatures for this year. The primary objective is to quantify the geothermal potential. In this framework, the geotechnical, hydrological and geothermal characterization discussed in previous chapters for each tunnel is of vital importance. Several assumptions were made regarding the soil temperature variation with depth as well as the groundwater due to the lack of information.

The onshore soil temperature for each project is assumed equal to the average air daily temperature for the first 40 meters of depth, whereas the offshore soil temperature, only applicable to the Genova case study due to the 500 m submerged section, is derived from the seawater temperature and its value depends on the cover of the tunnel. Moreover, based on experience on deep tunnels, a temperature gradient is applied for depths greater than 40 m, increasing the onshore soil

temperature by 3°C every 100 m. With respect to the groundwater table, further investigations are required in order to know the value of the groundwater velocity as well as the groundwater flow orientation with respect to the tunnel axis. Thus, for the sake of simplicity groundwater is assumed to be static leading to a value of groundwater velocity equal to 0.

Subsequently, the specific heat power, Q, for each homogeneous section is calculated with Eq. 14 that considers the surface area of the section as well as the geothermal potential. Eventually, a sum of the geothermal potential of each homogeneous section is performed in order to obtain the total geothermal potential along the tunnel lining.

$$Geothermal\ potential = \sum \pi \cdot D \cdot L \cdot q \qquad Eq.\ 14$$

where:

- D is the diameter of the tunnel expressed in [m].
- L is the length of the homogeneous section expressed in [m].
- q is the specific heat power of each homogeneous section expressed in [W/m^2] obtained with the use of the nomograms (see Figure 7).

It must be remarked that all three projects consist of twin tunnels, thus, the geothermal potential must be calculated by appropriately multiplying it by two. However, it is assumed that thermal interaction between the two tunnels is negligible for three primary reasons. First, the distance between the tunnels, which ranges between 18 and 40 m depending on the case study as described in Chapter 3. Second, due to the hypothesized absence of groundwater flow, which minimizes the potential for thermal interaction. Lastly, the charts used to estimate the geothermal potential were built for a specific tunnel diameter and their accuracy decreases when applied to significantly different diameters. As a result, verification of the geothermal potential through numerical modelling is necessary.

4.2 Subport Tunnel in Genova

The key feature of this project is the location of the tunnel, since approximately 450 m of the tunnel chainage are below the seawater level. Thus, seawater temperature must be accounted for in this section of the tunnel. In this context, the annual average seawater temperature was calculated for every meter of depth, up to 50 m, as shown in Figure 17. The offshore temperature surrounding the submerged tunnel lining is assumed to remain constant throughout the year, both in winter and summer, as a yearly average was employed. Linear interpolations were performed to estimate the seawater temperature at each depth of the tunnel cover, which ranges from 36.6 m to 43.4 m in the submerged section. As a result, seawater temperatures between 14.4 °C and 16.1 °C were determined.

Moreover, based on the average air temperature recordings derived from ARPA Liguria the soil temperature for the onshore tunnel section was estimated following the criteria discussed in chapter 4.1. It must be highlighted that, for the year 2023, an average air temperature value equal to 18.33 °C was found for the port of Genova and thus, it is considered representative of the onshore summer and winter temperatures.

Figure 36 presents a comparison of the onshore and offshore temperature profiles with respect to the depth. The submerged section of the tunnel is influenced by seawater temperatures, with seawater extending to a depth of approximately 30 m, while the onshore section reaches a maximum depth of nearly 90 m, In the onshore portion, the soil temperature remains constant within the first 40 m, beyond which a temperature gradient is applied, as detailed in Section 4., resulting in a maximum onshore temperature of approximately 20 °C. In contrast, as discussed earlier in this section, the offshore temperatures exhibit lower values, ranging from approximately 14 °C to 16 °C.

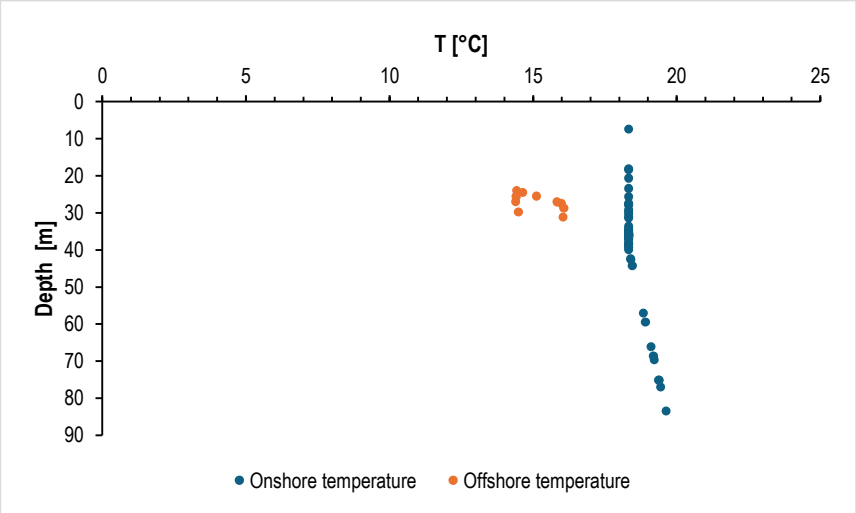

Figure 36. Evolution of the temperature with respect to the depth

Furthermore, different temperature classes were created as seen in Table 16 in order to compute the specific heat power. Additionally, Table 16 illustrates the different classes that were created in terms of the lithological description as well as the characteristic geothermal parameters for each lithology class, taken as the average values from the ranges listed in Table 4. It should be noted that the vertical hydraulic conductivity (k_v) was assumed to be one-tenth of the horizontal hydraulic conductivity due to the absence of this parameter in the technical reports carried out by Autostrade per l'Italia.

Table 16. Summary matrix with indication of the classes for the two parameters taken into account in the proposed methodology – Subport Tunnel Genova

Class	T [°C]	Lithology around the tunnel
1	14-15	compact limestone with occasional levels of calcareous argillite $k_h = 5.5x10^{-7}$ m/s; $k_h = 5.5x10^{-8}$ m/s; $\lambda = 2.81$ W/mK; $c_p = 0.85$ MJ/m^{3}K; $\eta = 0.05$
2	15-16	clayey marl with the presence of layers of compact, overconsolidated clayey-sandy silt $k_h = 5.05x10^{-7}$ m/s; $k_v = 5.05x10^{-8}$ m/s $\lambda = 2.34$ W/mK; $c_p = 0.92$ MJ/m^{3}K; $\eta = 0.18$
3	16-17	weakly thickened silty sands, clayey sands and sandy clays

		$k_h = 5.05x10^{-4}$ m/s; $k_v = 5.05x10^{-5}$ m/s $\lambda = 0.89$ W/mK; $c_p = 0.83$ MJ/m^{3}K; $\eta = 0.53$
4	18-19	-
5	19-20	-

Table 17 outlines the seven homogeneous sections defined along the tunnel chainage, detailing their respective temperatures, lithologies and specific geothermal potentials. The submerged section is comprised within the sections highlighted with gray, where the surrounding lithology of the tunnel corresponds to clayey marls. The estimated specific heat power for the submerged section amounts to 0.84 MW and 0.36 MW in winter and summer, respectively. Subsequently, a geothermal potential equal to 7.56 MW for a single tunnel during the winter season was obtained while in summer a value of 1.05 MW was estimated. This variation can be attributed to the lower specific heat power that can be obtained at elevated ground temperatures during summer as illustrated in the nomograms in Figure 7.

Additionally, the previous computations were made for the case of the project of interest, namely a twin tunnel. Thus, a geothermal potential in winter equal to 15.09 MW was obtained. On the other hand, during the summer 2.1 MW of geothermal potential can be exploited along the entire chainage.

Table 17. Proposed homogeneous sections for the Subport Tunnel of Genova for a single tunnel

Progressive distance [m]	Proposed homogeneous section	T [°C]	Lithology	Geothermal potential [MW]	
0				Winter	Summer
50	1	18.3	Compact limestone	0.11	0.01
100		18.3		0.11	0.01
150		18.3		0.11	0.01
200		18.3		0.11	0.01
250		18.3		0.11	0.01
300		18.3		0.11	0.01
350		18.3		0.11	0.01
400		18.3		0.11	0.01
450		18.3		0.11	0.01
500		18.4		0.11	0.01

550		18.5		0.11	0.01
600		18.8		0.11	0.01
650		18.9		0.11	0.01
700		19.2		0.12	0.01
750		19.4		0.12	0.01
800		19.1		0.12	0.01
850	2	19.2		0.12	0.01
900		19.4		0.12	0.01
950		19.6		0.12	0.01
1000		19.4		0.12	0.01
1050		18.3		0.11	0.01
1100		18.3		0.11	0.01
1150		18.3		0.11	0.01
1200		18.3		0.11	0.01
1250		18.3		0.11	0.01
1300		18.3		0.11	0.01
1350		18.4		0.11	0.01
1400		18.3		0.11	0.01
1450		18.3		0.11	0.01
1500		18.3		0.11	0.01
1550		18.3		0.11	0.01
1600		18.3		0.11	0.01
1650	1	18.3		0.11	0.01
1700		18.3		0.11	0.01
1750		18.3		0.11	0.01
1800		18.3		0.11	0.01
1850		18.3		0.11	0.01
1900		18.3		0.11	0.01
1950		18.3		0.11	0.01
2000		18.3		0.11	0.01
2050		18.3		0.11	0.01
2100		18.3		0.11	0.01
2150		18.3		0.11	0.01
2200		18.3		0.11	0.01
2250		18.3		0.11	0.01
2300		18.3		0.11	0.01
2350	3	16.1	Clayey marl	0.09	0.02
2400	4	16.0		0.09	0.03
2450		15.1		0.09	0.03
2500	5	14.6		0.08	0.04

2550		14.4		0.08	0.04
2600		14.4		0.08	0.04
2650		14.4		0.08	0.04
2700		14.5		0.08	0.04
2750	3	16.0		0.09	0.02
2800	4	15.8		0.09	0.03
2850	6	18.3		0.11	0.01
2900		18.3		0.11	0.01
2950	7	18.3	Silty sands, clayey sands, sandy clays	0.11	0.01
3000		18.3		0.11	0.01
3050		18.3		0.11	0.01
3100		18.3		0.11	0.01
3150	1	18.3	Compact limestone	0.11	0.01
3200		18.3		0.11	0.01
3250		18.3		0.11	0.01
3300		18.3		0.11	0.01
3350		18.3		0.11	0.01
3400		18.3		0.11	0.01
3450		18.3		0.11	0.01
3491.7		18.3		0.11	0.01
			Total heat power =	7.56	1.05

Furthermore, Figure 37 illustrates the spatial distribution of geothermal potential along the tunnel chainage. The variation in geothermal potential is directly correlated with fluctuations in onshore and offshore temperatures, with the offshore section, located between km 2+350 and km 2+800, highlighted between the two vertical lines. As onshore ground temperature increases, the exploitable geothermal potential rises correspondingly, whereas it decreases during summer. Conversely, for the submerged section, the geothermal potential decreases in winter and increases in summer, which can be attributed to the lower temperatures estimated for the offshore section compared to the onshore section. A possible explanation for this phenomenon lies in the design nomograms (Figure 7), where the exploitable geothermal potential in winter increases with high temperatures, while the opposite occurs with high temperatures in summer.

Additionally, in the first kilometer of the chainage, a slight lag is observed between the rise in onshore temperature and its impact on geothermal potential. This is attributed to the fact that, up to a length of 600 m, the temperatures fall

within temperature class four which ranges from 18 to 19 °C, as defined in Table 16, resulting in a constant value of the geothermal potential.

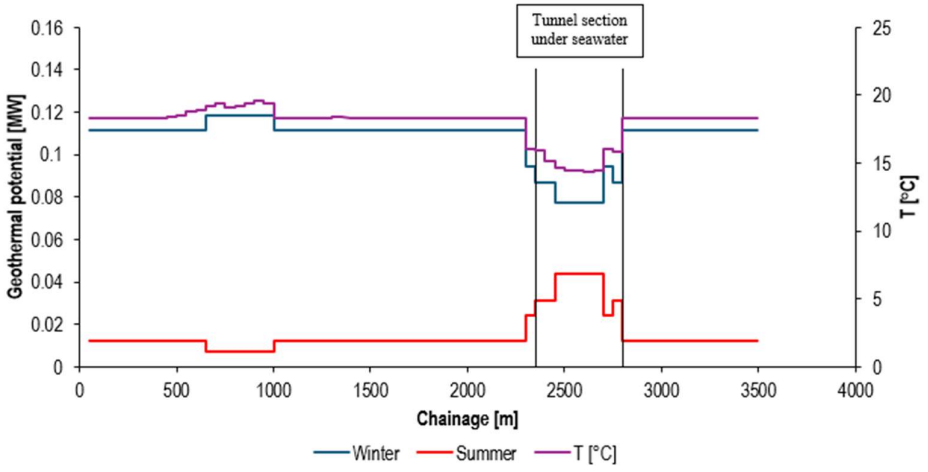

Figure 37. Spatial distribution of the geothermal potential along the chainage. Tunnel subportuale Genova

The properties listed in the Geothermal framework, such as thermal conductivity, specific heat conductivity and porosity are illustrated in Figure 38 through Figure 40. It is important to note that variations in each geothermal parameter correspond to changes in the surrounding lithology, as these properties are inherently dependent on the lithological composition of the tunnel surroundings.

Figure 38 shows the thermal conductivity and its variation with respect to the tunnel chainage. First, it can be noted that a constant value of 2.81 W/mK is obtained for the onshore section up to a length of 2350 m. Subsequently, the thermal conductivity slightly decreases along the offshore section, which can be arributed to the change of lithology surrounding the tunnel. For the remaining portion, the thermal conductivity fluctuates. Figure 39 depicts the variation of the specific heat conductivity along the chainage. The variations of this parameter can be destected in the same regions as for the thermal conductivity, concluding that these parameters as well as porosity illustrated in Figure 40 depend on the lithological composition of the soil.

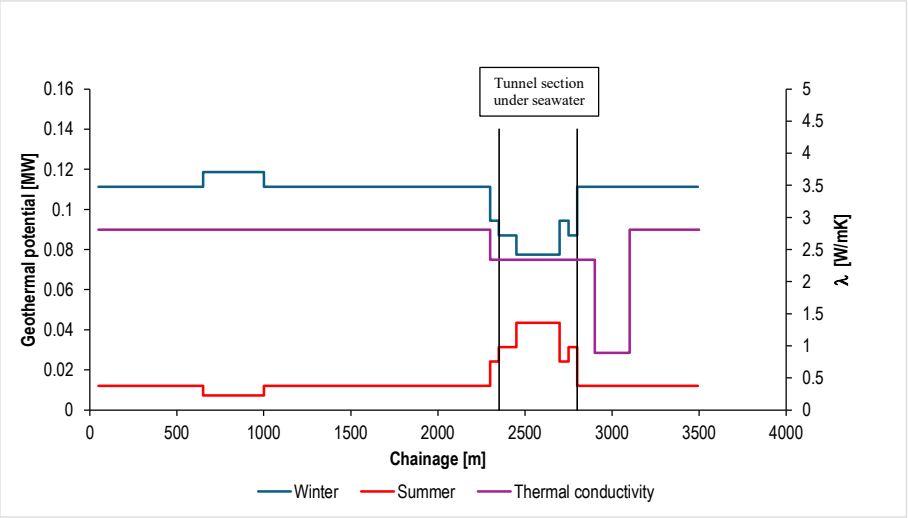

Figure 38. Spatial distribution of the thermal conductivity along the chainage. Subport Tunnel of Genova

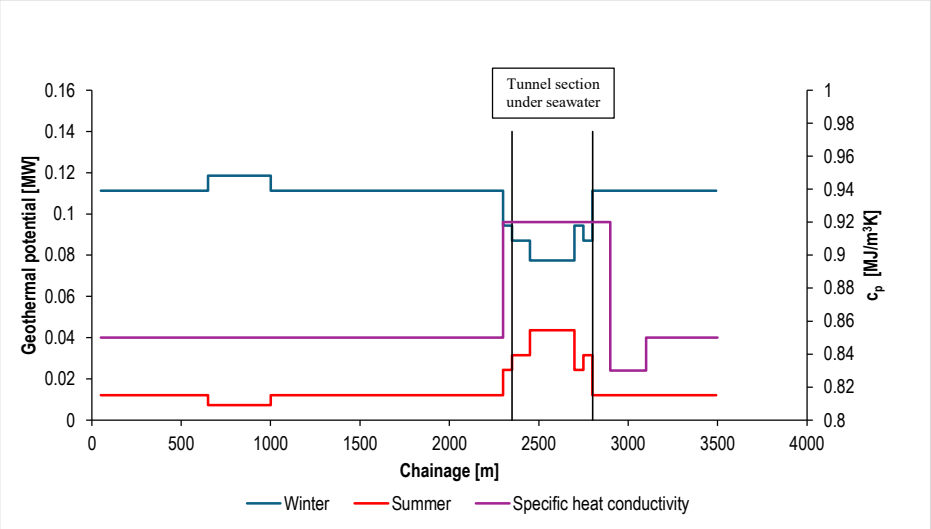

Figure 39. Spatial distribution of the specific heat conductivity along the chainage. Subport Tunnel of Genova

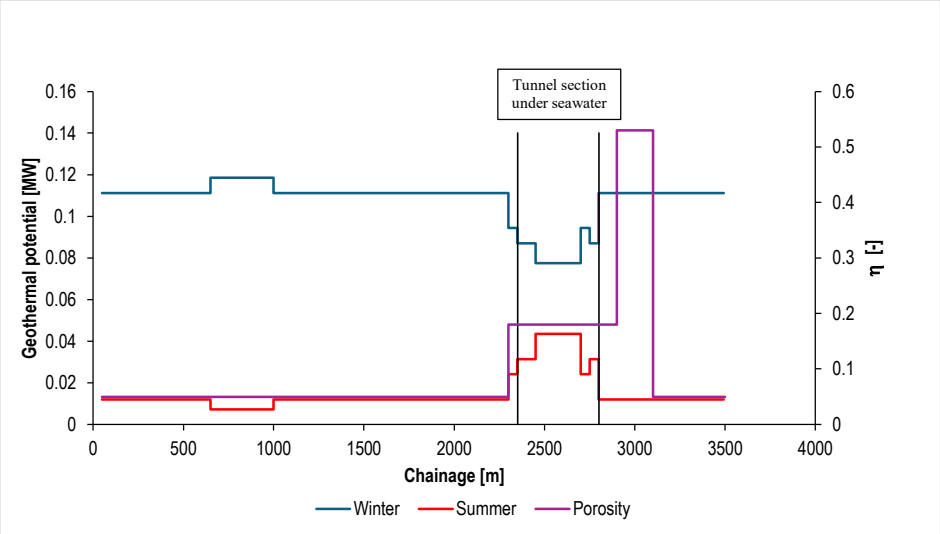

Figure 40. Spatial distribution of the porosity along the chainage. Subport Tunnel of Genova

Furthermore, the estimated geothermal potential per meter in winter and summer were calculated dividing the geothermal potential estimated with Eq. 14 by its corresponding length. As a result, Figure 41 and Figure 42 portray the geothermal potential per meter in a plan view of the tunnel chainage. At first glance, it can be noticed that regarless of the values, the region where the lowest geothermal potential can be extracted during winter corresponds to the offshore section, where the highest geothermal potential can be injected during summer and viceversa.

For the submerged section, the lowest potential along the chainage during winter can be extracted, which amounts to less than 1600 W/m. In contrast, the highesr geothermal potential (more than 800 W/m) can be injected during the summer season. This can be attributed to the use of the nomograms, which is explained in section 4.3, where the offshore temperatures ranging from 14 to 16 °C lead to a higher specific heat power in winter than in summer.

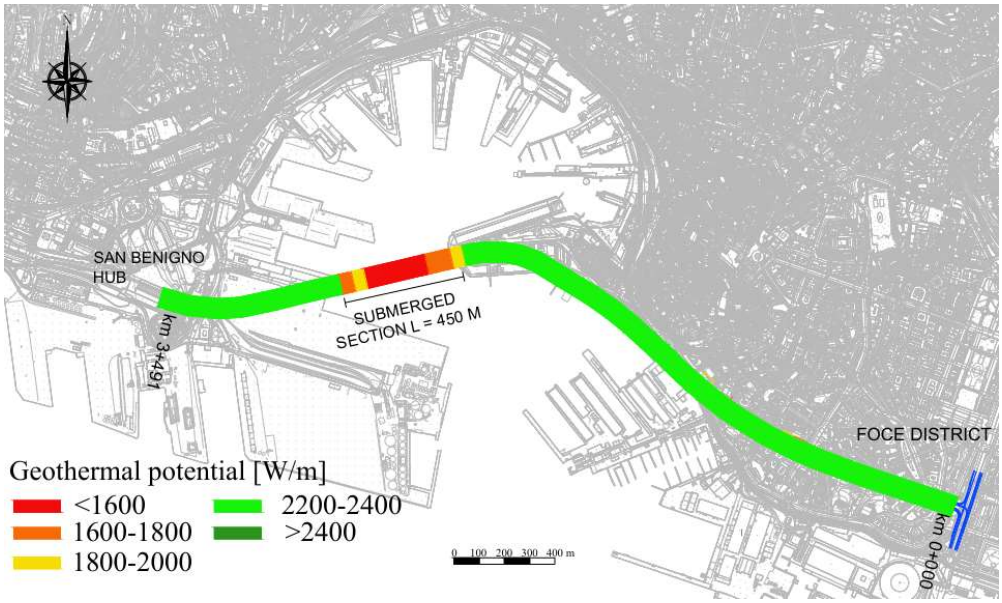

Figure 41. Estimated geothermal potential per meter in winter – Subport Tunnel Genova

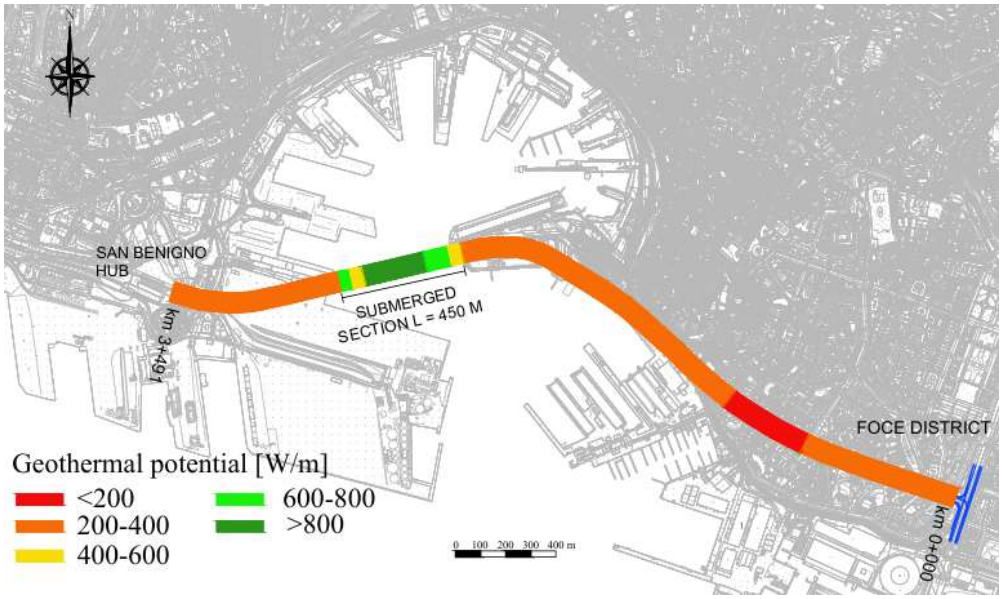

Figure 42. Estimated geothermal potential in summer – Subport Tunnel Genova

In order to have a better understanding of the results in Figure 41 and Figure 42, the temperature, lithology classes and location of the homogeneous sections along the chainage are provided in Figure 43, Figure 44 and Figure 45, respectively.

From Figure 43, it can be noted that the lowest temperatures belong to the offshore section of the tunnel. On the contrary, the onshore section is characterized by temperatures ranging from 18 to 20 °C. As explained in the beginning of this section, the temperature values of the tunnel onshore section depend on the annual average air temperature (18.33 °C) and the tunnel cover, which in the case of the Subport Tunnel of Genova does not exceed the 90 m, as per the geotechnical profile provided by Autostrade per l'Italia. Furthermore, making the comparison between Figure 42 and Figure 43, it can be concluded that if low temperature values are estimated, it will directly result in a low geothermal potential and viceversa. The opposite can be said for winter (Figure 41), where low temperatures are beneficial for the extraction of higher geothermal potential.

From Figure 44 it can be deduced that for the present analysis, at least, the lithology is not a key factor for estimating the geothermal potential since the nomograms do not take into account the thermal properties of the soils surrounding the tunnel. For this purpose, and to study the role of the seawater in the geothermal potential a 3D FEM model was carried out, which is further described in Chapter 5 of this Thesis.

Lastly, the distribution of the homogeneous sections along the tunnel chainage outlined in Table 17 is illustrated in Figure 45. It can be seen that the homogeneous sections of the submerged length and the largest portion of the onshore section were defined based on the different ground temperatures. On the other hand, the homogeneous sections near the San Benigno Hub were defined based on the change in lithology in that area.

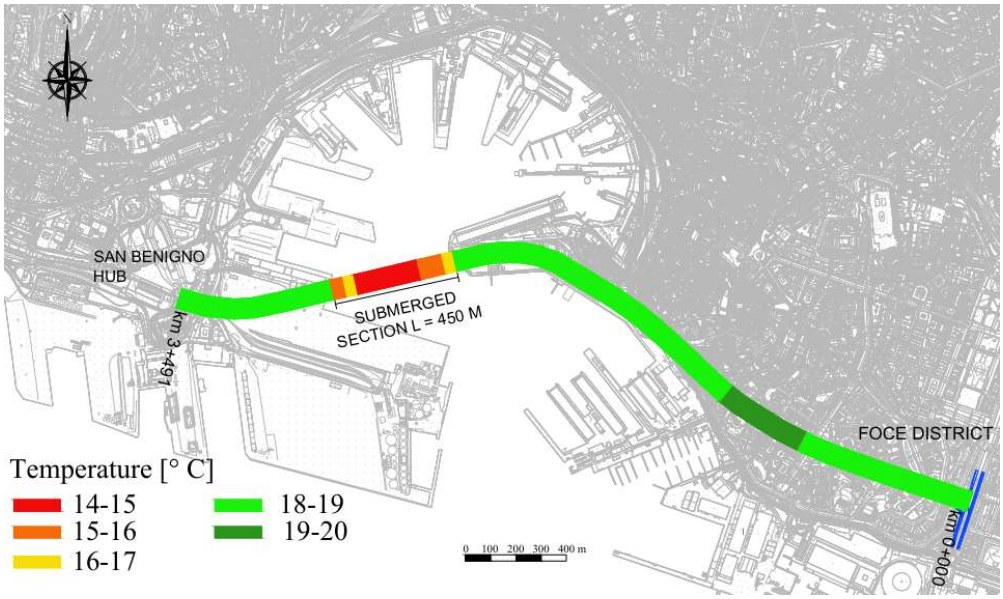

Figure 43. Plan view of the temperature classes along the tunnel chainage – Subport Tunnel of Genova

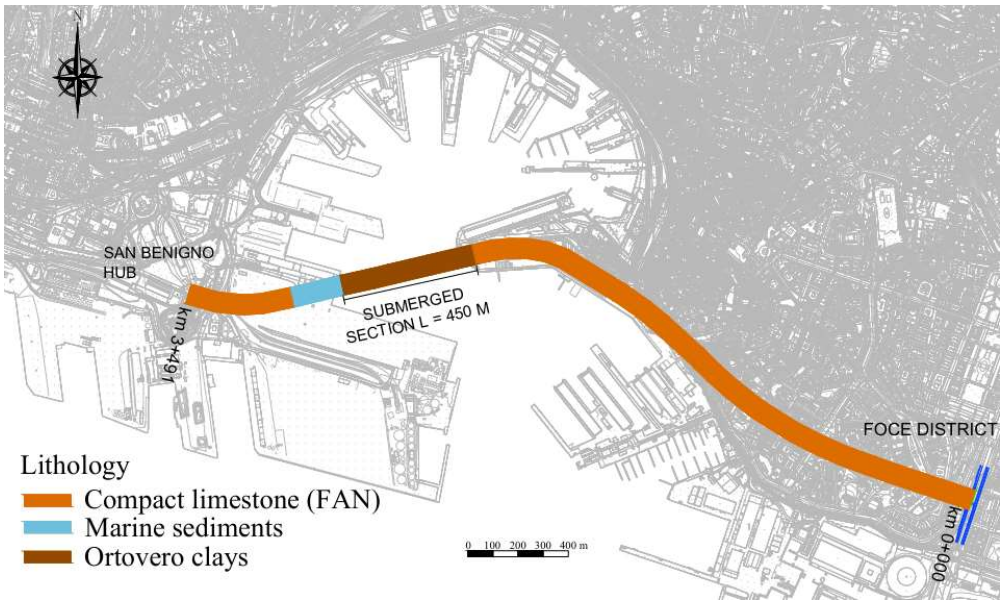

Figure 44. Plan view of the lithology classes along the tunnel chainage – Subport Tunnel of Genova

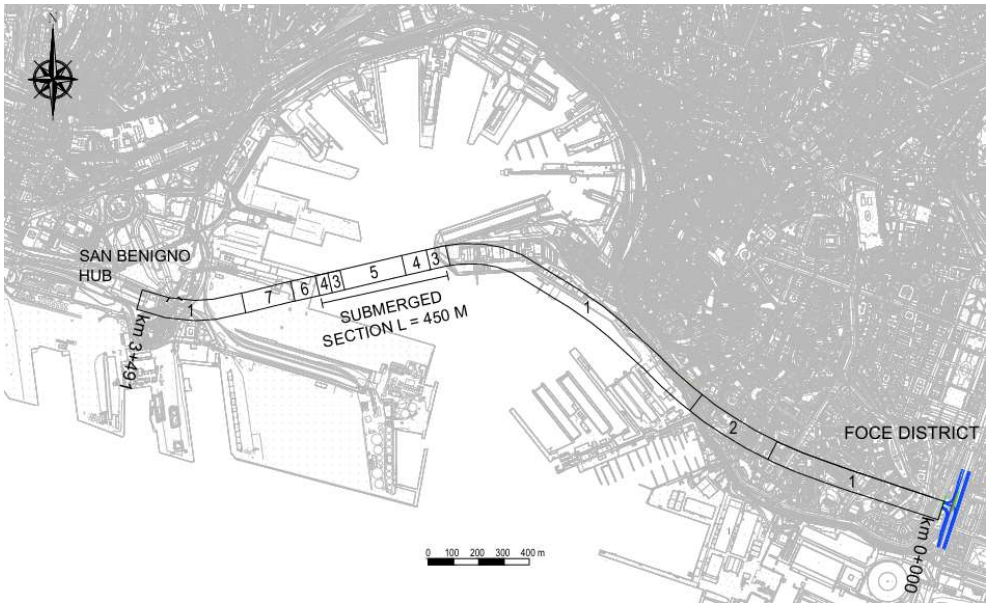

Figure 45. Plan view of the homogeneous sections along the tunnel chainage – Subport Tunnel of Genova

4.3 Trento tunnel

Based on a thorough analysis, it can be said that among the three case studies the Trento tunnel possesses the largest number of homogeneous sections with a total of 31 (Table 18) since there is explicit information along the geotechnical profile regarding the position of the piezometric surface with respect to the tunnel. It can be seen that only the first 350 meters of the tunnel chainage are characterized by a piezometric surface below the surface whereas the rest of the profile is constituted by a piezometric surface above the surface, meaning a fully saturated tunnel (refer to the geotechnical profile illustrated in Figure 23).

Furthermore, a yearly air average temperature equal to 13.75°C was derived from the database ARPA Trento and used for the creation of the different temperature classes following the criteria described in chapter 4.1. It must be highlighted that this temperature is assumed as constant throughout the year and thus, summer and winter temperatures are assumed to be represented by this value with the aim of obtaining the geothermal potential from the nomograms illustrated in Figure 7. The geothermal potential can be determined by knowing the values of the ground temperature and the groundwater flow velocity. For instance, with a soil temperature of 14 °C and a groundwater flow velocity equal to 0 m/s, as in the case of winter-heat extraction, a geothermal potential of 30 W/m^2 is obtained.

Furthermore, a few comments must be pointed out regarding the temperature classes. As described in paragraph 4.1, the soil temperature is increased by a temperature gradient of 3°C every 100 meters of depth since the maximum tunnel cover is approximately 245 m. However, the temperature classes listed in Table 18 surpass the temperature ranges considered in the nomograms (see Figure 7). Therefore, the proposed solution was to extrapolate the charts results by extending the lines using a drawing software such as AutoCAD in order to obtain the geothermal potential for temperature classes 6 and 7.

With respect to the lithology classes, some simplifications were made due to their geothermal properties. In this context, the following classes are composed of two of more lithological units, hence, reducing the number of homogeneous sections along the profile: class 2; class 3; class 5 and class 7. As for the Subport Tunnel in Genova, the geothermal parameters are listed together with the description of the lithology in Table 18 and were taken as the average values of the ranges listed in Table 8.

Table 18. Summary matrix with indication of the classes for the three parameters taken into account in the proposed methodology – Trento tunnel

Class	T [°C]	Lithology	Position of the piezometric surface with respect to the tunnel [m]
1	From 13 to 14	Polygenic gravels with sand and sandy, locally silty. $k_h = 1.62x10^{-3}$ m/s; $\lambda = 1.59$ W/mK; $c_p = 1.34$ MJ/m^{3}K; $\eta = 0.27$.	Above the crown
2	From 14 to 15	dark bituminous limestone (at the base), densely stratified limestone and marl, and possible clay layers. Limestone with local decimetric marl levels. Micritic limestones and calcareous marls with thin stratification. Micritic limestones densely stratified (5-15 cm) characterized by a red or brick red color red or brick red, flint in the lower part, with marly and marl interlayers.	Between the crown and the invert

		k_h = 2.35x10^{-3} m/s; λ = 2.58 W/mK; c_p = 0.85 MJ/m^{3}K; η = 0.17	
3	From 15 to 16	Light grey, yellowish dolomite with a very fine grain, in decimetric layers, separated by thin intercalations of greenish marl. Ossiliferous light stromatolitic dolomites. k_h= 3x10^{-6} m/s; λ = 3.17 W/mK; c_p = 0.88 MJ/m^{3}K; η = 0.26	Below the invert
4	From 16 to 17	Limestone and dolomite, interspersed with thin levels of pelites k_h = 2.35x10^{-3} m/s; λ = 2.99 W/mK; c_p = 0.88 MJ/m^{3}K; η = 0.29	-
5	From 17 to 18	Carbonate, terrigenous and mixed sediments. Alternations of limestone, dolomite, siltstone sandstone and marl. Yellowish-grey silty dolomites and dark grey silty limestones compact in predominantly nodular layers, alternating with grey sandstones and siltstones and marls with carbonaceous horizons. k_h = 9.64x10^{-4} m/s; λ = 2.91 W/mK; c_p = 0.90 MJ/m^{3}K; η = 0.25	-
6	From 18 to 19	Sandstones alternating with siltstones, marly siltstones and marls. k_h = 3.91x10^{-5} m/s; λ = 2.33 W/mK; c_p = 0.87 MJ/m^{3}K; η = 0.22	-
7	From 19 to 20	Grey, grey-green and reddish-grey rhyodatic tuff lapilli. Epilastites (dacytic and rhyodatic conglomerates). k_h = 5.05x10^{-10} m/s; λ = 2.96 W/mK; c_p = 0.99 MJ/m^{3}K; η = 0.26	-

8	-	Highly hydrothermalized, black, gray-green or violet-gray porphyritic andesitic lavas; Massive and pseudostratified lavas, associated with lavas with rounded and angular blocks cemented together. $k_h = 5.05x10^{-11}$ m/s; $\lambda = 2.75$ W/mK; $c_p = 0.85$ MJ/m^{3}K; $\eta = 0.08$	-
9	-	Quartzian fillades and phyllites [12] $k_h = 5.05x10^{-10}$ m/s; $\lambda = 2.42$ W/mK; $c_p = 0.60$ MJ/m^{3}K; $\eta = 0.01$	-
10	-	Limestone [13] $k_h = 4.70x10^{-3}$ m/s; $\lambda = 2.81$ W/mK; $c_p = 0.85$ MJ/m^{3}K; $\eta = 0.32$	-

Table 26 in the Appendix A section outlines the 30 homogeneous sections defined along the tunnel chainage, detailing their respective temperatures, lithologies and specific geothermal potentials. As a result, for a single tunnel a geothermal potential in winter equal to 12.03 MW was obtained, whereas the geothermal potential in summer was found equal to 3.8 MW. The significant contrast between the geothermal potential values in winter and summer can be primarily attributed to one factor, which is the lower value of geothermal potential (between 3 and 5 W/m^2) extracted from the nomogram corresponding to summer, for temperatures ranging between 17 and 19 °C. Conversely, considering the fact that this project is characterized by a twin tunnel, the geothermal potential in winter for both tunnels is equal to 24.1 MW while in summer a lower value equal to 7.6 MW is estimated.

Moreover, the spatial distribution of the geothermal potential along the tunnel's chainage is depicted in Figure 46. The same conclusion can be made as for the Subport Tunnel of Genova, where the variations in the ground temperature have a direct effect on the geothermal potential value. With every increment of soil temperature the geothermal potential in winter increases while a decrease in the geothermal potential in summer is noted. In the central section of the tunnel chainage the peak ground temperature was registered, due to the high depths of the tunnel cover (245 m). Consequently, the highest peak in the geothermal potential

during winter is observed while for summer, the geothermal potential reaches its lowest value. Contrary to the Subport Tunnel of Genova, the Trento ring road tunnel is characterized by several fluctuations of the geothermal potential along the tunnel chainage

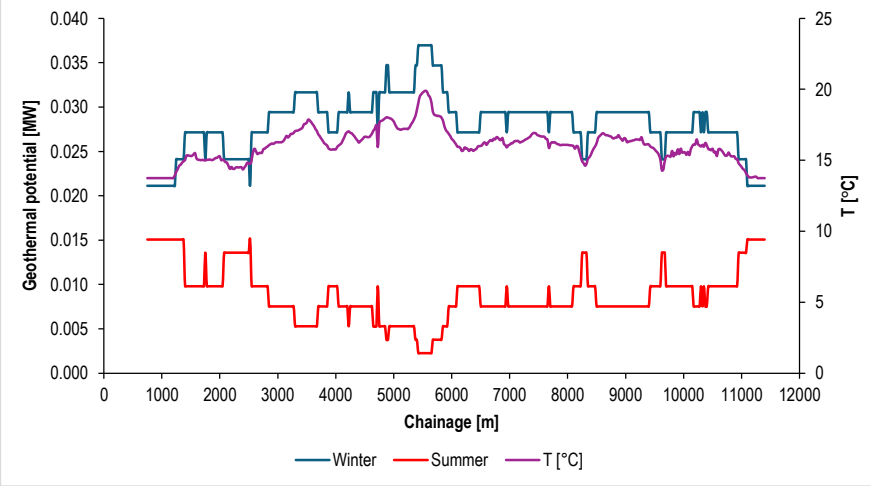

Figure 46. Spatial distribution of the geothermal potential along the chainage. Trento ring road tunnel

Figure 47 and Figure 48 illustrate the estimated geothermal potential per meter in winter and summer, respectively. As outlined before, the extracted geothermal potential during winter is greater than the injected geothermal potential in summer. The largest portion of the chainage is characterized by a geothermal potential ranging from 1100 to 1300 W/m in winter and from 200 to 400 W/m in summer. The lowest geothermal potential during winter and the highest potential in summer can be found in two regions: near km 0+000 and km 10+650, which correspond to the exits of the tunnel. This is compatible with the results from the Genova case study which highlight that for shallow depths of the tunnel cover will lead to low temperatures and thus, low geothermal potential in winter while the opposite occurs for summer. It must be remarked that this judgement was based on the interpretation of the nomograms described in the previous paragraphs of this section.

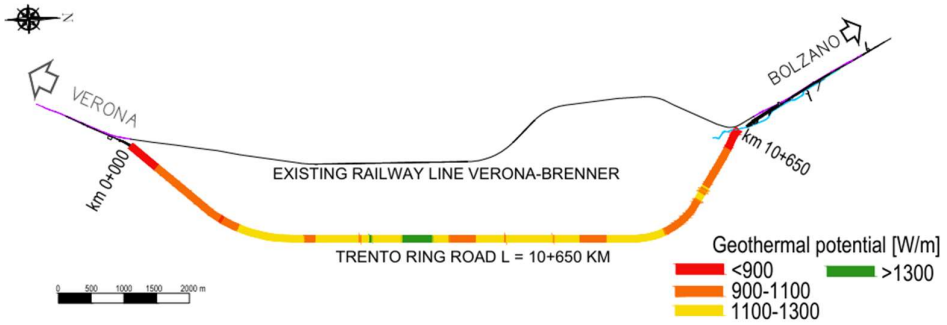

Figure 47. Estimated geothermal potential per meter in winter – Trento ring road tunnel

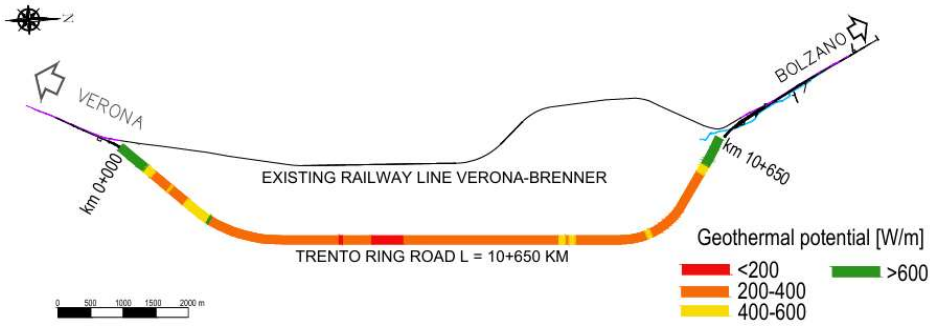

Figure 48. Estimated geothermal potential per meter in summer – Trento ring road tunnel

To better interpret the results shown in Figure 47 and Figure 48, the ground temperature classes, lithology and homogeneous sections were mapped in Figure 49, Figure 50, and Figure 51 respectively.

Figure 49 illustrates the distribution of the ground temperature along the chainage. There is a noticeable decrease of soil temperature from the central section towards the start and end of the chainage. A similar trend can be observed for the geothermal potential both in summer and winter, thus, reaching the conclusion once again that the ground temperature is the governing parameter at the moment of calculating the geothermal potential.

Furthermore, Figure 50 outlines the presence of the different lithology classes defined for the analysis, which amount to a total of 10. The portions of the tunnel chainage with the most critical values (highest and lowest) of the geothermal potential both for summer and winter can be identified. In the central portion of the chainage, class E can be distinguished whereas at the tunnel exits, the lithology

classes A, B and J are noted. Lastly, the distribution of the 30 homogeneous sections is given in Figure 51.

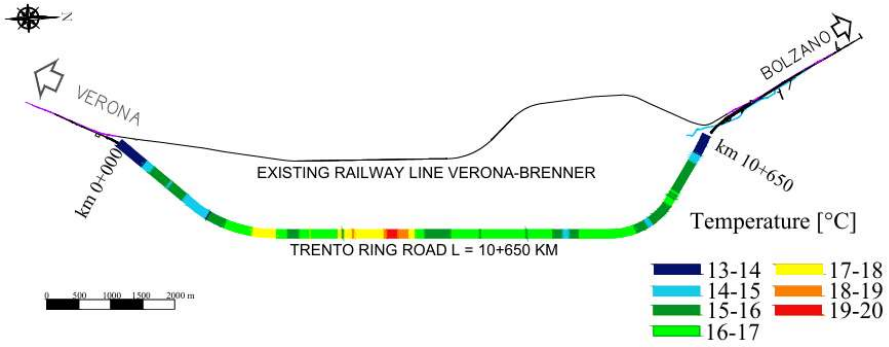

Figure 49. Plan view of the temperature classes along the tunnel chainage – Trento ring road tunnel

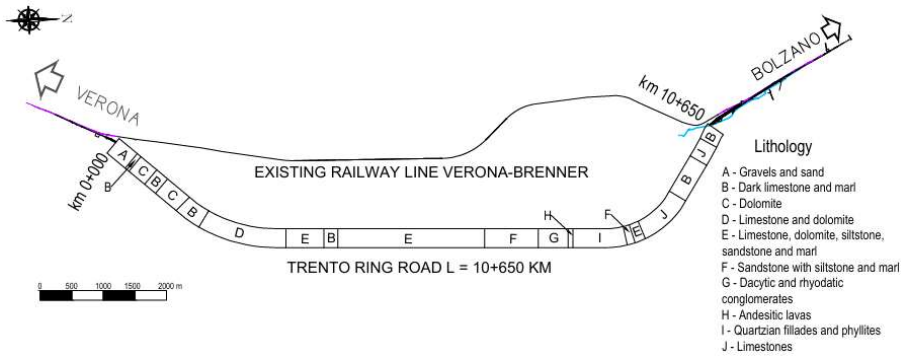

Figure 50. Plan view of the lithology classes along the tunnel chainage – Trento ring road tunnel

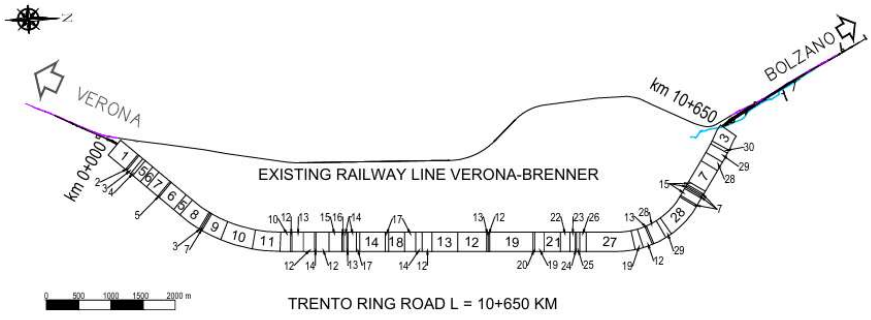

Figure 51. Plan view of the homogeneous sections along the tunnel chainage – Trento ring road tunnel

4.4 Cortina d'Ampezzo tunnel

Two of the main features of this project are its location due to the mountain environment in its surroundings and due to the depths of the tunnel cover, nearly 230 m. From the available documents the ground surface and tunnel elevation were only partly known. In particular, this data was not available between km 1+850 and km 3+700. In order to reconstruct both of them in this missing section, it was decided to georeference the chainage of the project with QGIS and subsequently, post-process it on Google Earth in order to obtain the ground elevation along the entire chainage and as a result, obtain the elevations enclosed within the red area in Figure 52. On the other hand, it was assumed that the project had a constant increase in elevation between km 1+850 and km 3+750 in order to avoid abrupt and unrealistic changes in elevation. As a result, gradual increments in the elevation of the tunnel of nearly 1.70 meters every 50 meters were computed. Accordingly, the interpretation of the hypothesis made is illustrated in Figure 52, where the area highlighted in red refers to the chainage where the previously methodology was adopted and where information about ground and tunnel elevation was missing.

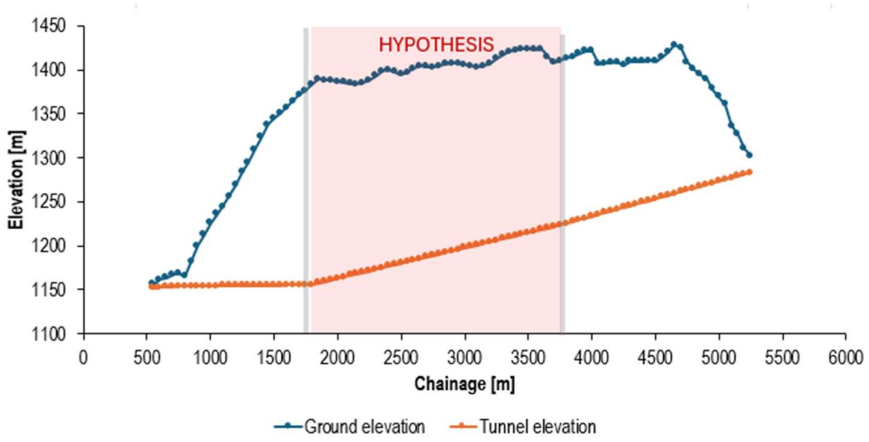

Figure 52. Hypothesis made for the tunnel and ground elevations – Cortina d'Ampezzo tunnel

It must be added that an air average temperature equal to 8°C was considered for the analysis and was derived from the database ARPA Veneto with the aim of creating the different temperature classes following the approach described in chapter 4.1, which involves applying the temperature gradient of 3 °C for every 100 meters of depth, while for the first 40 meters it is assumed that the ground temperature is equal to the annual average air temperature for the city of Cortina d'Ampezzo (8 °C) . It must be highlighted that this temperature is assumed to be

constant throughout the year and thus, both winter and summer are characterized by this value in order to obtain the geothermal potential from the nomograms given in Figure 7.

With regard to the lithology classes, a few simplifications were carried out due to their geothermal properties. In this framework, the only classes 1 and 2 are considered geothermally comparable, hence, reducing the number of homogeneous sections along the profile. As for the tunnel subportuale in Genova, the geothermal parameters are listed below Table 19 and were taken as the average values of the ranges listed in Table 8.

Table 19. Summary matrix with indication of the classes for the two parameters taken into account in the proposed methodology – Cortina D'Ampezzo tunnel

Class	T [°C]	Lithology
1	From 8 to 9	fine-grained silty clayey materials, with sometimes frequent inclusions of gravel, pebbles and blocks of dolomite and calcarenite nature. fine-grained silty clayey materials, with sometimes frequent gravel and sandy gravelly lenses. $k_h = 7.55x10^{-6}$ m/s; $\lambda = 1.71$ W/mK; $c_p = 1.2$ MJ/m^{3}K; $\eta = 0.82$.
2	From 9 to 10	coarse-grained materials, consisting of gravels, pebbles and blocks immersed in a sandy to sandy silty matrix. $k_h = 5.05x10^{-7}$ m/s; $\lambda = 1.59$ W/mK; $c_p = 1.34$ MJ/m^{3}K; $\eta = 0.27$
3	From 10 to 11	plastic clays with inclusions of various sizes, including dolomitic pebbles and cobbles $k_h = 7.81x10^{-6}$ m/s; $\lambda = 2.34$ W/mK; $c_p = 0.92$ MJ/m^{3}K; $\eta = 0.07$
4	From 11 to 12	mixed carbonate-siliciclastic succession, including shales, sandstones, and carbonates $k_h = 5.0x10^{-6}$ m/s; $\lambda = 3.17$ W/mK; $c_p = 0.88$ MJ/m^{3}K; $\eta = 0.04$
5	From 12 to 13	-
6	From 13 to 14	-
7	From 14 to 15	-

Table 27 in Appendix A section outlines the total number of 12 homogeneous sections that were weighed along the chainage detailing their respective temperatures, lithologies and specific geothermal potentials. As a result, for a single tunnel a geothermal potential in winter equal to 3.91 MW was estimated whereas in summer, 4.29 MW can be exploited. Alternatively, the geothermal potential for two tunnels must be calculated since the project consists of a twin tunnel. Hence, it can be concluded that 7.8 MW of geothermal potential during winter can be harnessed while during summer, a greater amount of geothermal potential can be exploited (8.6 MW).

It must be remarked that the Cortina d'Ampezzo tunnel is the only case from the three where the exploitable geothermal is higher during summer than in winter. This can be attributed to the low values of the ground temperature, which are dependent on the annual air average temperature of the city of Cortina d'Ampezzo (8 °C). Thus, with the criteria explained in Section 4.1, ground temperatures ranging from 8 to 15 °C were computed. For lower values of ground temperature, it can be seen that the geothermal potential that can be injected during summer is higher than the exploited geothermal potential during winter (refer to the nomograms shown in Figure 7). For instance, for a soil temperature of 11 °C with a groundwater flow velocity of 0 m/s, a geothermal potential of 30 W/m^2 in summer can be obtained, whereas for winter, the geothermal potential is equal to 20 W/m^2.

In addition, the analysis of the spatial distribution of the geothermal potential along the entire chainage is graphically carried out by means of Figure 53. The same trend as for the case studies of Genova and Trento can be observed regarding the influence of the temperature variations on the geothermal potential. Increase in temperature is followed by a drop in the geothermal potential in summer while the opposite occurs for the winter season.

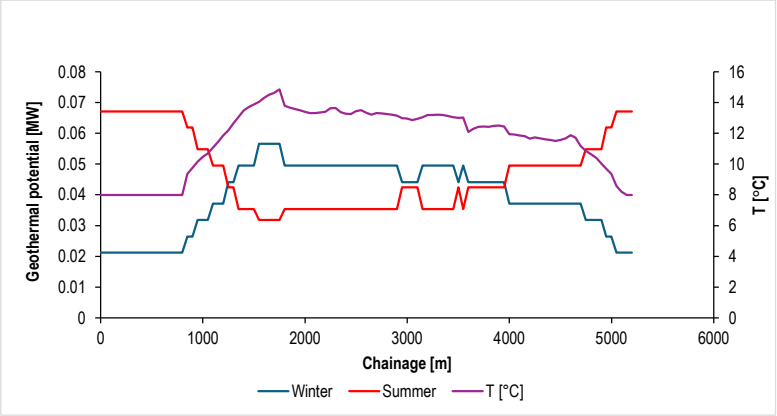

Figure 53. Spatial distribution of the geothermal potential along the chainage. Cortina d'Ampezzo tunnel

The estimated geothermal potential per meter along the tunnel chainage for winter and summer is illustrated in Figure 54 and Figure 55. Contrary to the previous two case studies, the geothermal potential values are comparable for both seasons, ranging from less than 500 W/m to more than 1300 W/m. It is repeatedly noted that the lowest geothermal potential during the winter season corresponds to the exits of the tunnel, which for this project correspond to km 5+550 and 5+250. In contrast, these areas are characterized by the greatest amount of geothermal potential in summer. Additionally, it can be seen that a geothermal potential lower than 500 W/m is absent along the tunnel chainage, since the total heat power estimated in the previous paragraphs is larger in summer than in winter.

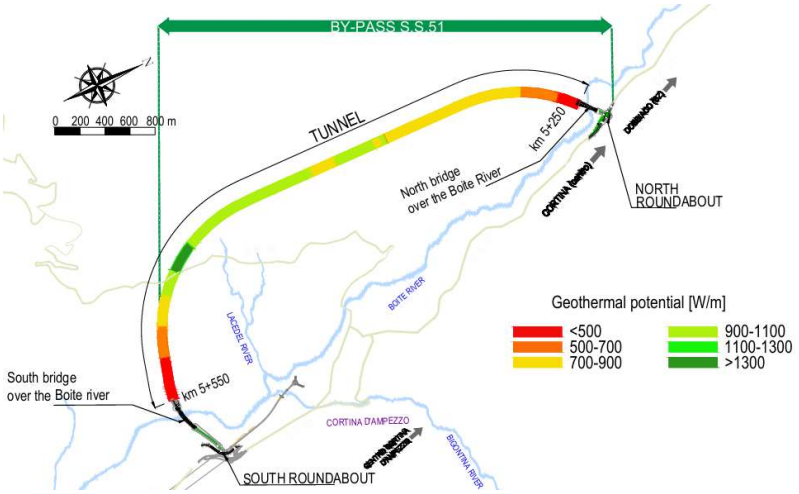

Figure 54. Estimated geothermal potential per meter in winter – Cortina d'Ampezzo tunnel

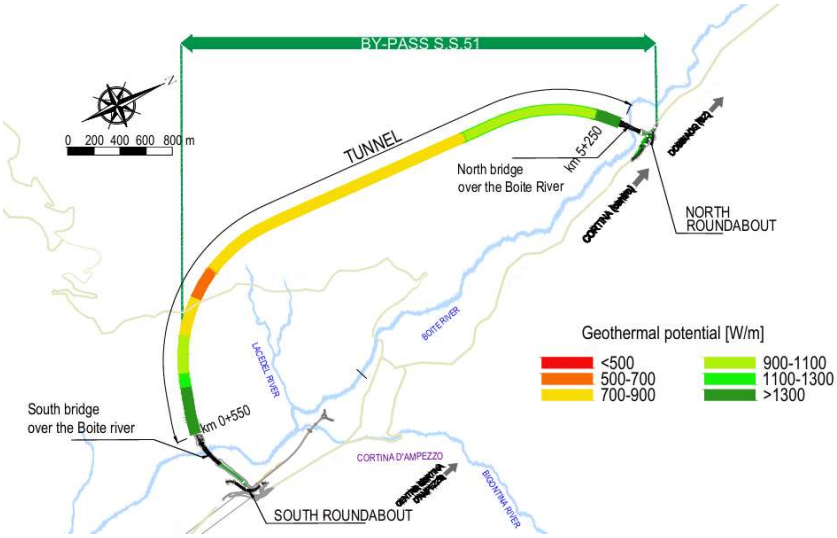

Figure 55. Estimated geothermal potential per meter in summer – Cortina d'Ampezzo tunnel

In order to carry out a thorough analysis as for the Genova and Trento case studies, the ground temperature and lithology classes as well as the homogeneous sections are illustrated in Figure 56, Figure 57 and Figure 58, respectively.

With respect to the temperature, the largest portion of the tunnel chainage is comprised within the ranges of 13 to 14 °C, mostly concentrated in the central section. This can be attributed to the nature of the project itself consisting of a mountainous environment and thus, large tunnel cover depths, which in turn translates for high soil temperatures after employing the temperature gradient previously described. Conversely, the lowest temperatures (8 to 9 °C) are found near km 0+550 and km 5+250, which are the tunnel exits. It can be seen that both conditions have a direct effect on the geothermal potential that can be extracted or injected along the chainage, where high temperatures lead to a low geothermal potential in summer and high potential in winter. The opposite can be said for low temperatures, which cause a large geothermal potential in summer and low in winter

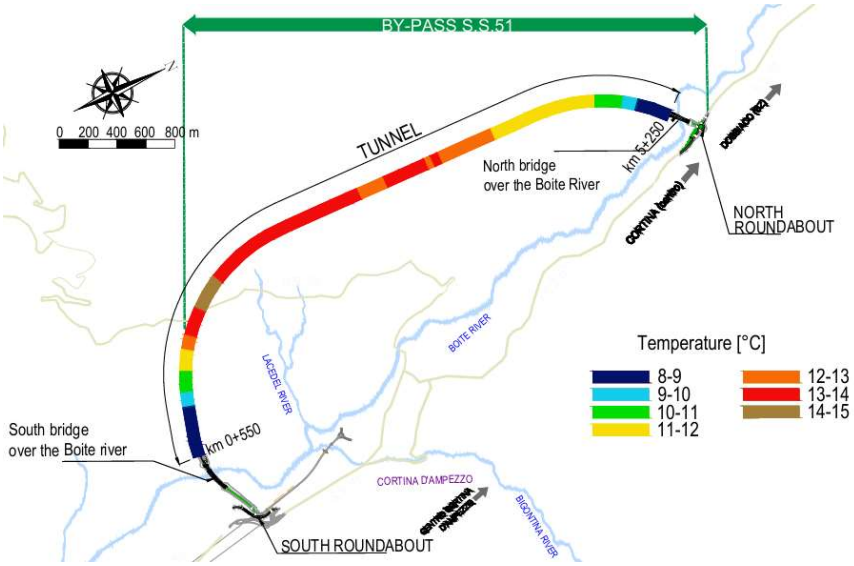

Figure 56. Plan view of the temperature classes along the tunnel chainage – Cortina d'Ampezzo tunnel

Figure 57 illustrates the four different lithology classes surrounding the tunnel. Clays with dolomitic pebbles and cobbles as well as shales, sandstones and carbonates are the two predominant lithologies along the chainage with temperatures between 10 and 15 °C. Fine and coarse-grained soils are present near the tunnel exits, at km 0+550 and 5+250, and are characterized by temperatures within the ranges of 8 to 9 °C. Interestingly, these two lithology classes display the highest geothermal potential in winter and the lowest geothermal potential in summer. However, it must be remarked that lithology classes are only employed in the creation of the homogeneous sections, which contain similar features in terms of ground temperature, lithology and geothermal properties in order to assign a uniform value of the geothermal potential to each section with a certain length. Such homogeneous sections are included in Figure 58 for the Cortina d'Ampezzo tunnel. A total of 12 were found, with sections number 5 and 6 being the most concurrent along the plan view. It is possible to refer to Table 27 in order to review further details regarding the homogeneous sections for this case study.

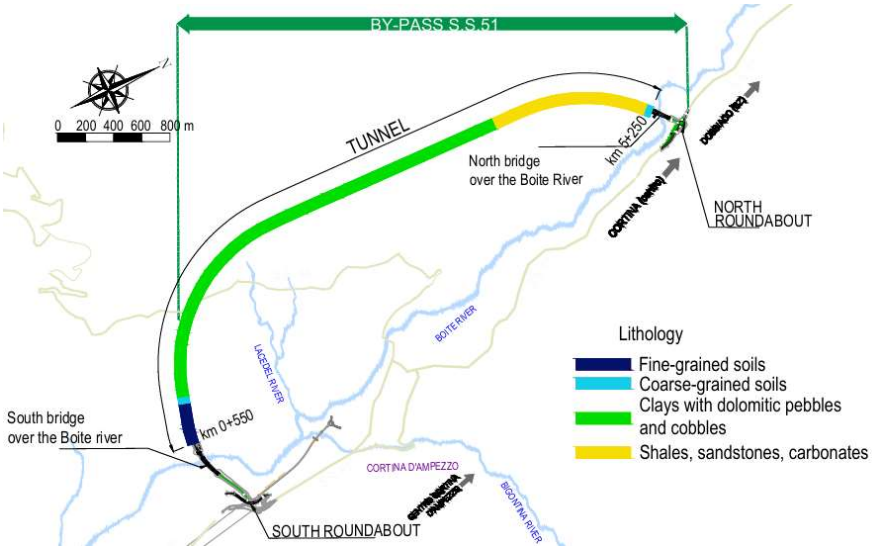

Figure 57. Plan view of the lithology classes along the tunnel chainage – Cortina d'Ampezzo tunnel

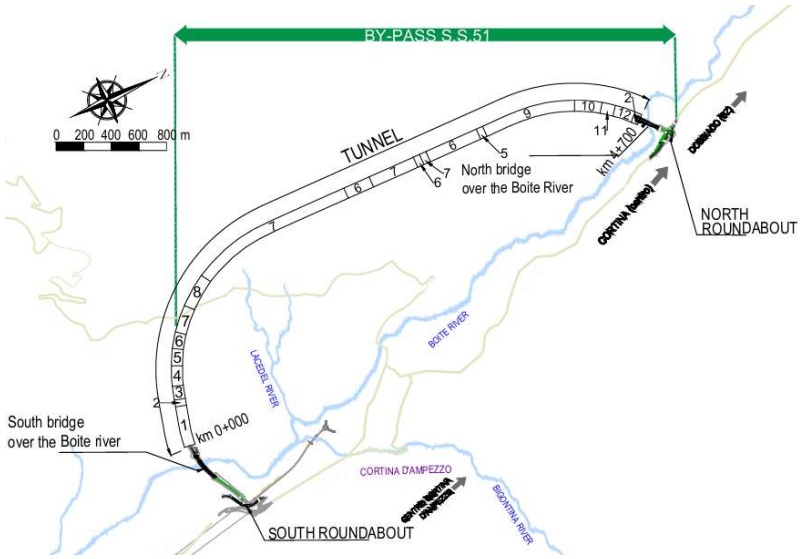

Figure 58. Plan view of the homogeneous sections along the tunnel chainage – Cortina d'Ampezzo tunnel

Chapter 5

Numerical modeling of the Subport Tunnel of Genova

5.1 Introduction

The present chapter has the purpose to describe the methodology employed for the numerical modeling of the Subport Tunnel of Genova. In addition, it provides a detailed justification for each decision made regarding the model setup, including domain assembly, mesh selection, application of initial and boundary conditions, and the material properties assigned to all model elements. Each aspect is motivated and exhaustively discussed.

The principal motivations for developing the 3D finite element model can be summarized in three key points. First, the Subport Tunnel of Genova includes a submerged section beneath the sea, approximately 450 m in length. A deeper investigation into the effects of seawater temperature on the tunnel's geothermal behavior is crucial. Therefore, the section selected for modeling using the "Finite Element subsurface FLOW simulation system" (FEFLOW), corresponds to chainage km 2+550, where the seawater level reaches 19 m as detailed in Figure 59. This location was selected because it represents the greatest depth along the submerged section of the tunnel.

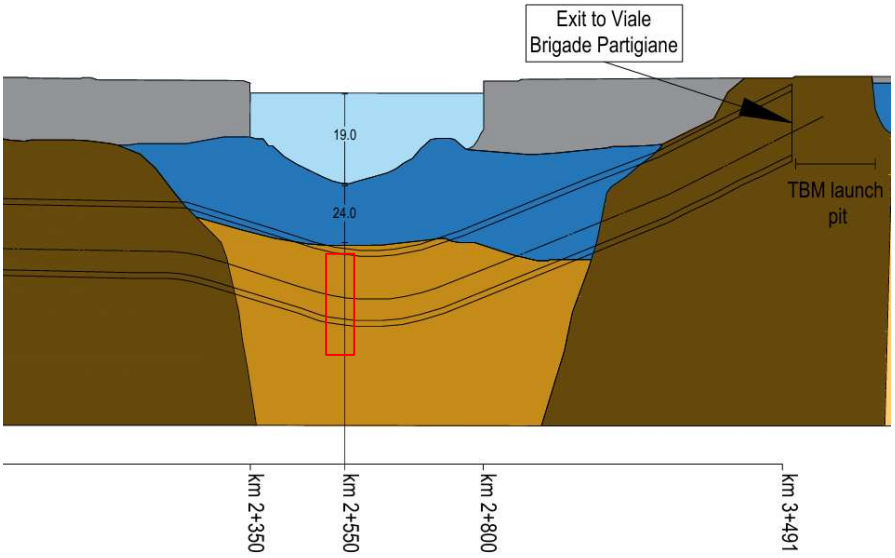

Figure 59. Submerged section of the tunnel to be modelled on FEFLOW (km 2+550)

Second, the nomograms employed to evaluate the geothermal potential along the tunnel chainage, as portrayed in Figure 7, are ideal for projects with similar characteristics and dimensions like the Turin Metro Line 1, which has a diameter of 7.48 m. Conversely, the diameter of the Subport Tunnel of Genova is 15.4 m, more than twice that of the Turin Metro. This difference considerably influenced the decision to build a 3D model. With respect to the case studies of Trento and Cortina d'Ampezzo, the tunnel diameters consist of 8.4 m and 11.25 m, respectively.

Additionally, the soil temperature surrounding the Subport Tunnel of Genova exceeds the range covered by the nomogram, potentially leading to inaccuracies in the calculations. Hence, the comparison between the geothermal potential computed with the nomograms and the one estimated with the numerical model is made whereas the outputs of the numerical model are thoroughly discussed and motivated.

5.2 Geometry of the model and Problem Settings

The model geometry was created by means of an AutoCAD DXF file, which was subsequently imported into FEFLOW as illustrated in (Figure 60). The size of the model consists of a total width of 323.40 m and a height of 152.3 m. The lateral

boundaries were placed at a distance equal to 10 times the diameter of the tunnel in order to avoid the influence of the boundary conditions in the analysis.

In contrast, the total height of the model is determined by three factors: the seawater level at the section under evaluation, as explained in Section 5.1, the thickness of the marine sediments and the Ortovero clays, all derived from the original geotechnical profile (Figure 60). The top boundary was set at the seawater level (19 m), whereas the bottom boundary was positioned at a distance of six times the tunnel diameter to prevent boundary conditions from being placed too far from the tunnel. Additionally, it was assumed that the stratigraphy remains consistent at these depths, as no further stratigraphic information is available from the original geotechnical profile. Thus, the Ortovero clays layer was extended up to the bottom boundary.

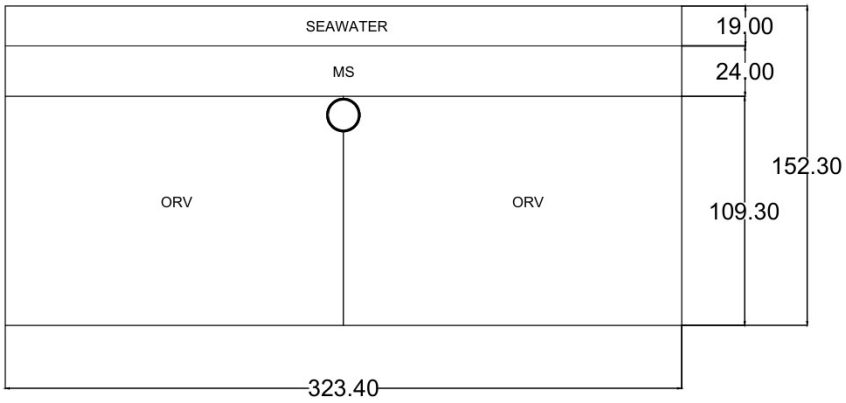

Figure 60. Dimensions of the FEFLOW model in 2D - DXF format

In particular, the tunnel lining, the grout and the heat carrier pipes are illustrated in Figure 61. Since FEFLOW does not support the creation of circular elements, a polygon with 72 sides was designed on AutoCAD in order to approximate the tunnel circumference as accurately as possible.

The heat carrier pipes were positioned at a distance of 6 cm from the extrados of the tunnel lining, indicating a Ground configuration as heat exchange with the surrounding ground predominates, as discussed in Section 2.3.2.9. The pipes are distributed across nine segments of the tunnel, as outlined in the design provided by Autostrade per l'Italia (refer to Figure 14). Moreover, the thicknesses of the tunnel lining and grout were determined based on the project specifications detailed in Section 3.2.1 and are shown in Figure 61.

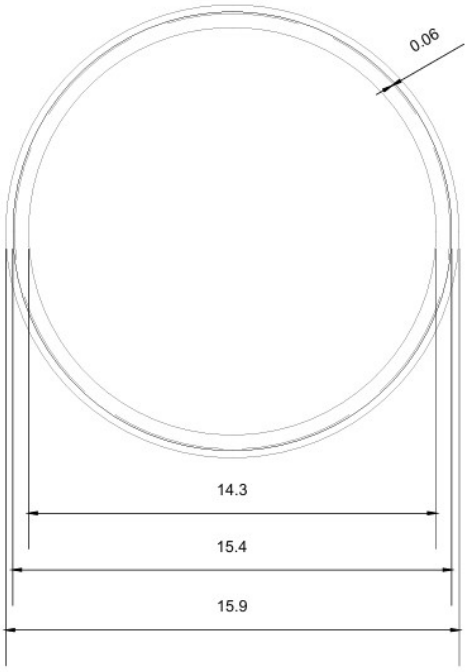

Figure 61. Imported cross section of the tunnel. GROUND configuration (dimensions in meters)

The DXF file is subsequently imported into FEFLOW, where points, lines and polygons from the drawing file are recognized to from the "Supermesh". This feature serves as the basis for generating the finite-element mesh, supplying all essential geometric data required by the mesh generation algorithm. For this reason, it is crucial to model the heat exchanger pipes as lines, while elements such as the tunnel lining, the grout, and lithology must be designed as polygons within the DXF file. This approach ensures accurate mesh construction and facilitates the selection of these elements for future steps in the creation of the model. Figure 62 portrays the Supermesh view of the tunnel circumference following the import of the DXF file into FEFLOW.

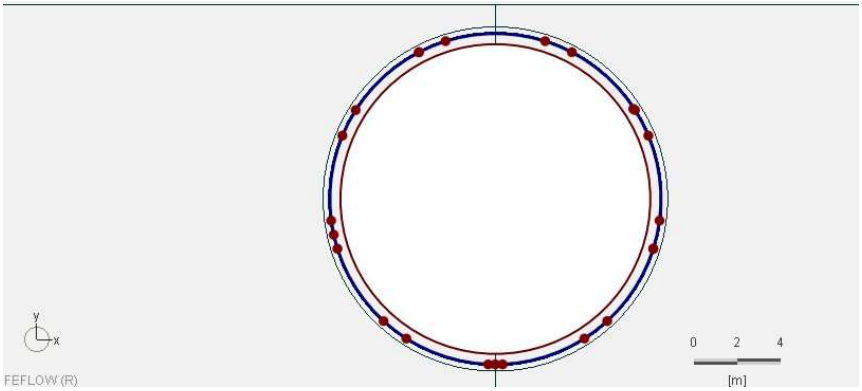

Figure 62. Supermesh view of the tunnel circumference on FEFLOW

The "Problem settings" window, shown in Figure 63, is used to define the type of analysis. The first modification involves selecting the type of exchange for the analysis. Specifically, the checkbox corresponding to heat exchange must be enabled, whereas the remaining options can remain at their default settings, as the medium is saturated and will be simulated using the standard groundwater-flow equation. On the other hand, both fluid flow and transport are set to transient conditions.

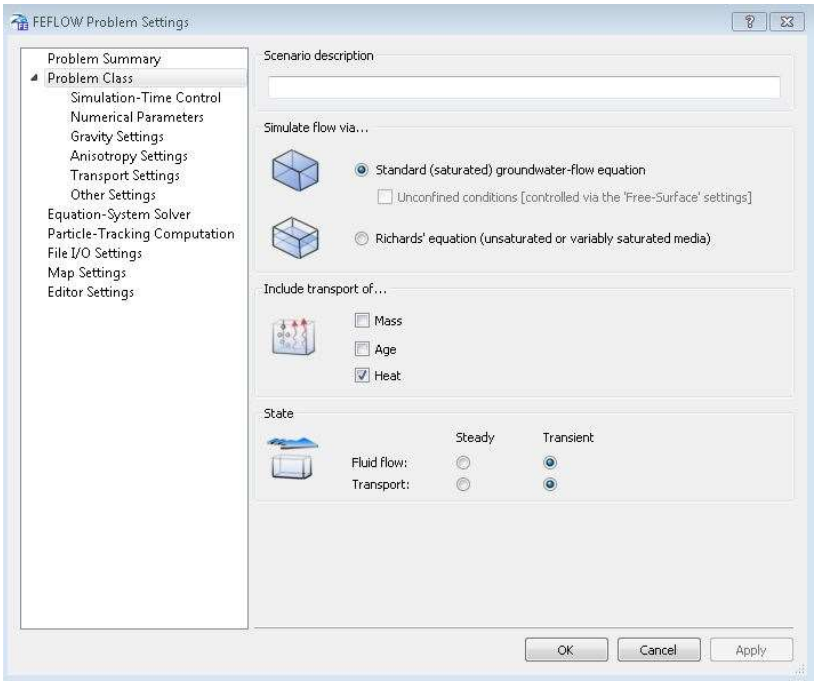

Figure 63. Problem Settings window - FEFLOW

The second adjustment to be made is connected with the direction of the gravity, since we want to be in the x-y-z plane and thus, a negative-y direction is chosen as illustrated in Figure 64.

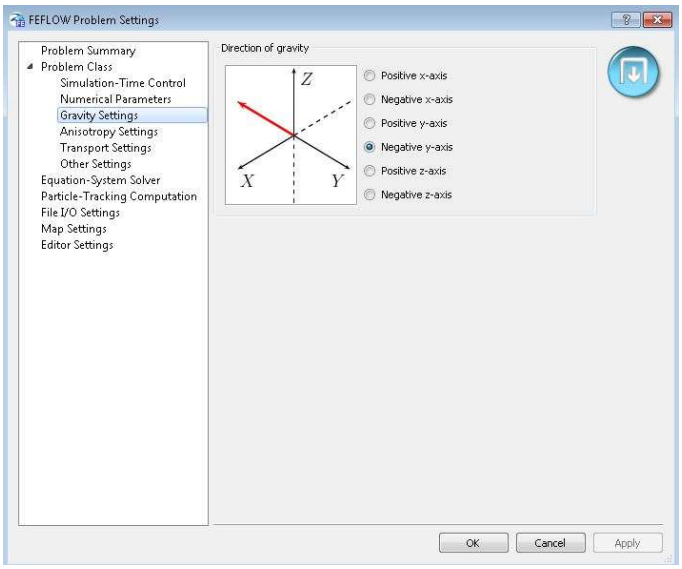

Figure 64. Gravity settings on FEFLOW

The third and last adjustment concerns the simulation duration. A total period of 5 years (1825 days) was selected for the analysis, with time steps set at 5-days intervals. The principal motiviation for this choice is to effectively monitor the outputs and their temporal evolution. To implement this, a POW format file must be created and imported, specifying the desired time steps in the appropriate time units. In addition, as indicated in Figure 65, the “Defines output times if DAC-file recording is enabled” checkbox must be activated, ensuring that the specified time steps are appriopriately considered by the software.

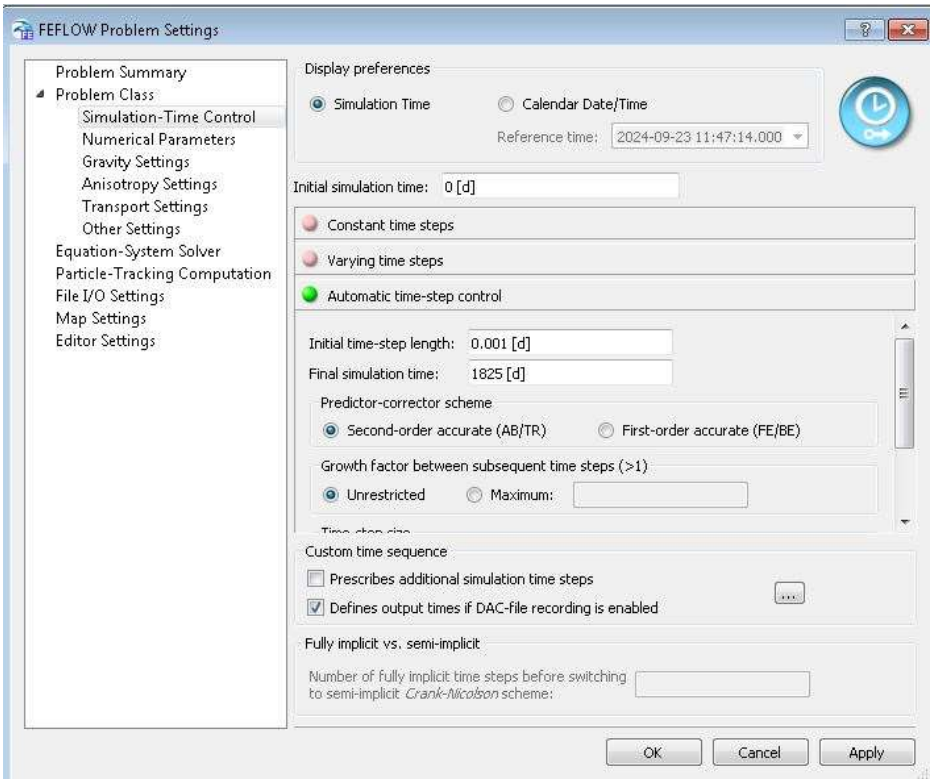

Figure 65. Simulation-Time Control window

The mesh is then generated using the "Mesh Generator" panel. The Triangle mesh was selected based on the information and characteristics provided by DHI-Wasy (2013), the software developer. According to the user manual of the company, this mesh type is extremely fast, supports very complex combinations of polygons, lines and points in the supermesh, allows a minimum angle to be specified for all finite elements to be created, and provides the means for local mesh refinement with a maximum element size at lines or points of the supermesh.

In this context, the mesh is refined in regions requiring higher accuracy, particularly around the intrados and extrados of the tunnel lining, as well as near the top boundary of the model. The latter is crucial in order to apply a boundary condition related to air temperature that will be introduced in the subsequent paragraphs. Figure 66 illustrates the dimensions of the mesh elements, withparticular emphasis on the line target size, which is a critical factor in defining the total number of elements in the model. For computational efficiency, the target for the total number of elements was set to not exceed 40,000. This objective was

met by applying a line target size of 0.15 m, resulting in a total number of 33,363 elements within the model.

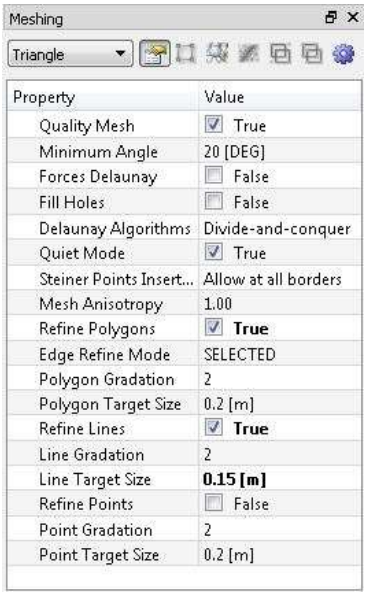

Figure 66. Mesh settings on FEFLOW

Furthermore, the mesh along the entire domain is depicted in Figure 67, where it is evident that element size gradually decreases as near the tunnel edge. Additionally, a line was positioned along the top boundary in order to carry out the mesh refinement in that zone with the objective of applying an air temperature boundary condition and ensuring the highest possible accuracy in the results. Consequently, the density of the elements increased at the top boundary.

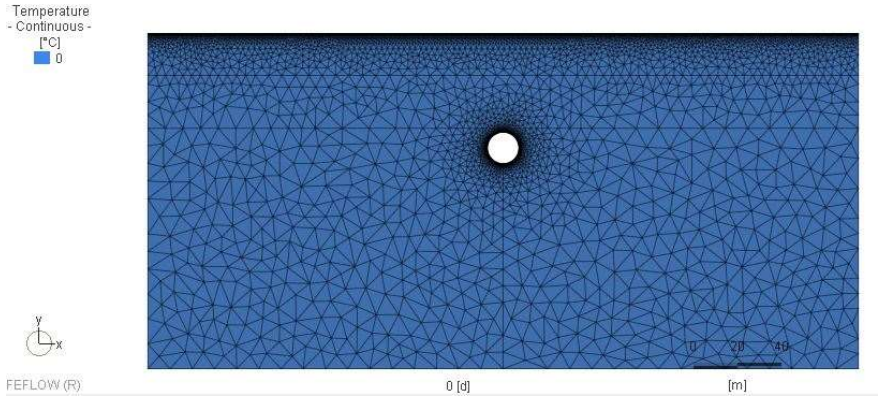

Figure 67. Model discretization

The details of the mesh refinement near the tunnel boundary are provided in Figure 68. This was achieved by incorporating the heat carrier pipes as lines within the Supermesh. A finer mesh in this region is vital for capturing significant temperature variations in this type of analysis, where heat transfer and thermal gradients occur.

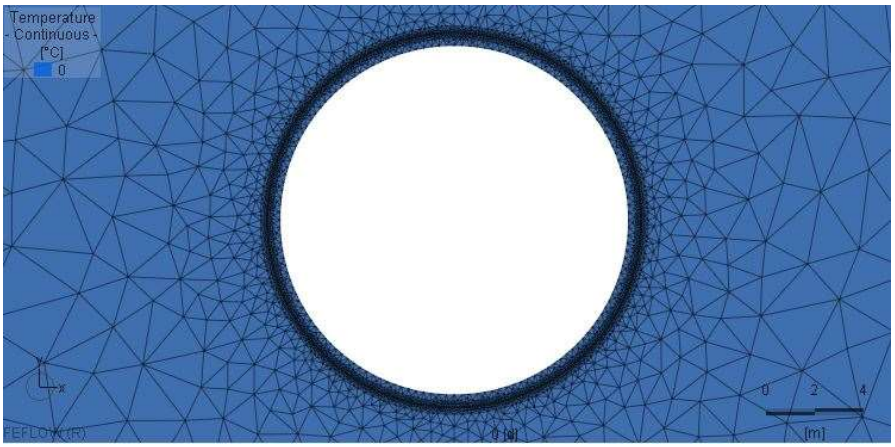

Figure 68. Discretization near the tunnel edge

Afterwards, it is possible to proceed with the extrusion of the model into 3D through the "3D Layer Configuration" menu. The number and thickness of the slices must be determined a priori, based on the number and dimensions of the rings in the out-of-plane direction, as well as the configuration and spacing of the heat carrier pipes. For the latter, an odd number must be selected to ensure proper alignment and connection of the pipes between the rings. In the model, five pipes with a 20 cm external diameter and a 2 cm thickness, were positioned per ring with the spacing detailed in Figure 69. The spacing of the pipes is a function of their spacing, thus, enough distance must be provided among them in order to prevent breakage. Consequently, the outer pipes were placed 20 cm from the ring, while the internal pipes maintained a uniform spacing of 40 cm between them. The longitudinal section, shown in Figure 60, illustrates the correlation between the placement of the heat carrier pipes and the arrangement of the precast concrete tunnel segments, of which there are nine in total (refer to Figure 14).

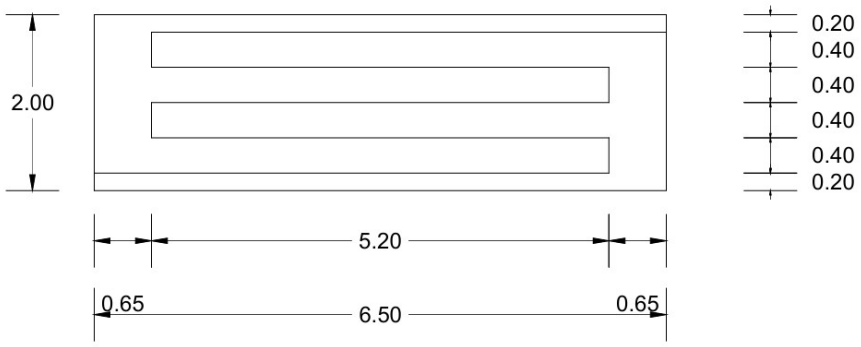

Figure 69. Plan view of the pipe configuration for a single ring

With reference to the tunnel rings, a total of five rings were selected, as shown in Figure 69. The primary motivation for this choice is based on the findings of Barla & Insana (2022), which demonstrate that using five rings in series minimizes the cost of the circuitry components and the costs for pumping the heat carrier fluid through the primary circuit. This conclusion was derived from the hydraulic optimisation analysis of the Turin Metro Line 1 case study. Subsequently, a ring thickness of 2 m was adopted, inspired by the Sparvo tunnel case study (Bandini et al., 2017), which has a comparable diameter to that of the Subport Tunnel of Genova. This decision was made due to the absence of specific data regarding the ring thickness in the technical reports prepared by Autostrade per l'Italie.

In summary, the model is formed by five parallel rings, each with a thickness of 2 m, resulting in a total elevation of 10 m, as depicted in Figure 70. This configuration generates a total of 31 slices, including the slices designated for the placement of piping systems. With respect to the classification of the slices, the Movable class was applied to the slices delineating the initial and final sections of each tunnel ring. In contrast, the Fixed condition was assigned to the slices designated for pipe installation. In this class, the slices maintain a constant elevation throughout the analysis.

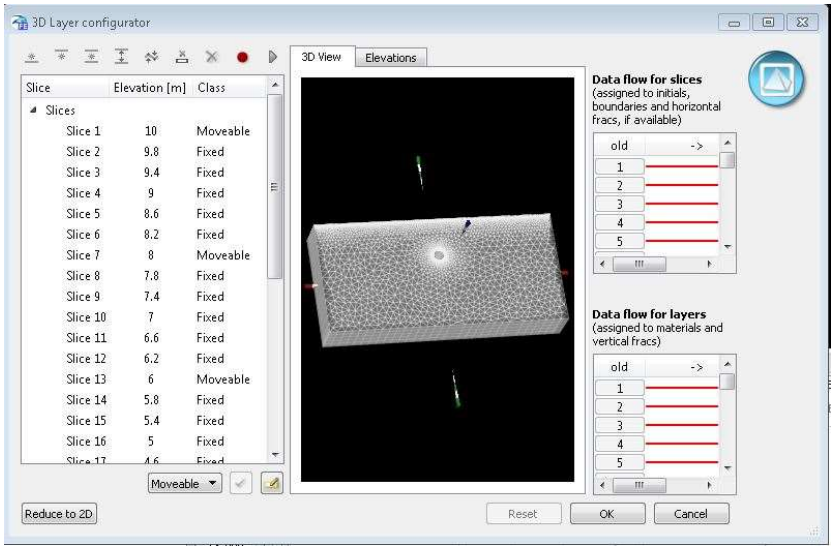

Figure 70. 3D Layer configuration of the Subport Tunnel of Genova

Prior to the creation of the pipes within FEFLOW, it is crucial to verify the dimensions of the 2D mesh elements as illustrated in Figure 71. In the region where the pipes are located, a single 2D element is selected, and the length of its three sides are measured. The ratio between any side of the selected element and the extruded out-of-plane dimension once extruded (corresponding to the 40 cm spacing of the pipes in this case) must be greater than 1/10 to prevent excessive elongation in the third dimension. The element in Figure 69 has a length of 6 cm, thus it can be concluded that the verification is satisfied, as the resulting ratio is 8/40 = 2/10.

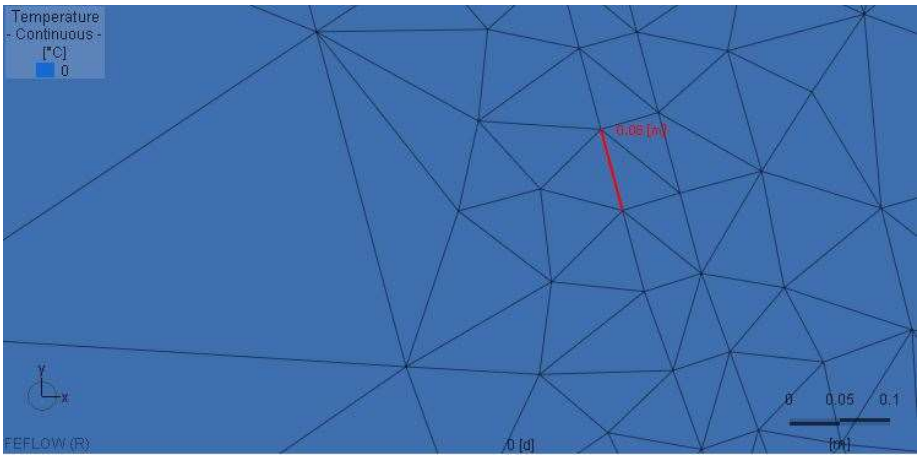

Figure 71. Verification of the elongation of a single 2D element

The pipes, configured as depicted in Figure 69 are then modeled in 3D model for the entire tunnel section of interest. Once the pipe circuit is defined, the "Discrete Features" must be assigned, which, as per the instructions manual, are finite-element objects of lower dimension than the existing model and represent one- or two-dimensional discrete features such as tunnels, pipes, drains, faults or fractures.

FEFLOW allows the application of three different flow laws which govern the convection-diffusion problem: Darcy, Hagen-Pouseville and Manning-Strickler. According to Alvi (2021), for pipes with a small diameter, such as those used in this study (20 mm), the Hagen-Pouseville law is most appropriate. However, it neglects the thermal properties of the pipe material. Despite this limitation, the resulting error is minimal due to the small dimensions of the pipe under consideration. Figure 72 illustrates the 3D arrangement of the pipes throughout the entire section of interest.

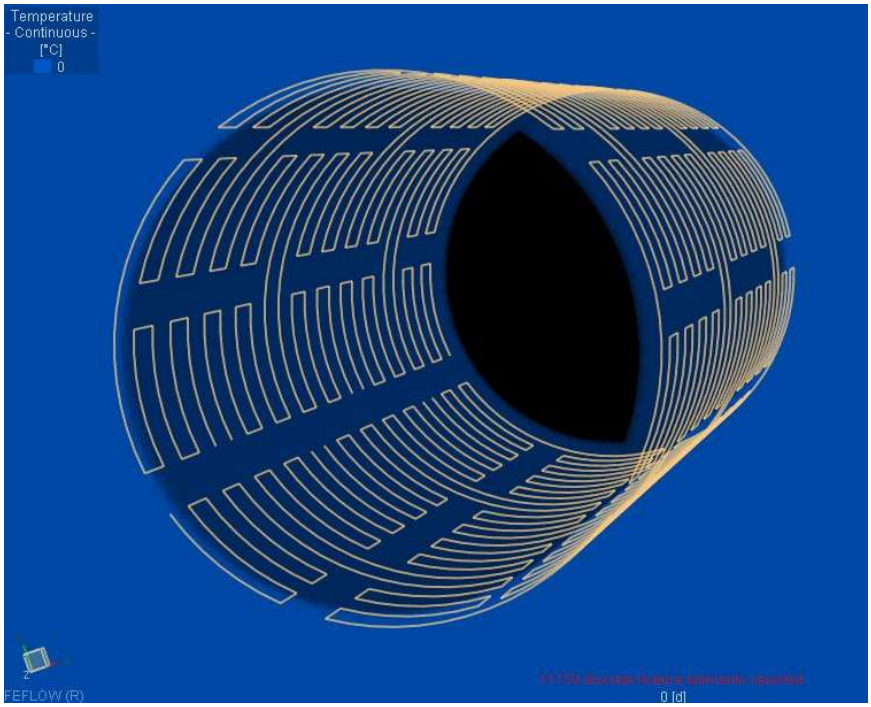

Figure 72. 3D Configuration of the heat exchange pipes and subsequent creation of the Discrete Features

5.3 Material properties

To facilitate the assignment of geothermal parameters to the lithology of interest, as well as to seawater and concrete (tunnel lining and grout), Element Groups must be created in FEFLOW. The geothermal properties listed in Table 16 are employed as inputs in FEFLOW for the two lithological units of interest: Ortovero Clays and Marine Sediments. In contrast, the parameters used for concrete were derived from the values used by Insana (2020) in the study of the Turin Metro Line 1. It is important to note that FEFLOW categorizes geothermal properties into three main groups: heat transport, conductivity, and dispersivity.

Table 20 provides a summary of the parameters used in the model. Values for thermal conductivity (λ_w) and specific heat ($c_{p,w}$) of the fluid phase were obtained from literature, with both properties being influenced by the salinity of the water. For the Ligurian sea, mean salinity values recorded from 2002 to 2018 ranged between 35 and 38.5 g/kg (Parodi, 2018). As per Spalding & Taborek (1983), the thermal conductivity of seawater with a salinity of 35 g/kg at 20 °C is 0.60 W/mK. Based on data from Nayar et al. (2016) the specific heat capacity of seawater at the same salinity and temperature is 3.97 kJ/kg·K. Similarly, longitudinal and transversal dispersivity values were adopted from the study by Barla et al. (2016) for the case study of the Turin Metro Line 1, as they are typically calibrated through continuous monitoring. For this reason, these values were assumed equal for the case study of the Subport Tunnel of Genova.

With respect to the porosity, values of 1 and 0 were employed for the seawater layer and the concrete elements, including the tunnel lining and grout, respectively. In this framework, concrete is considered to have no voids within its structure as it does not have any voids within the material, while the seawater naturally possesses a full porosity. Lastly, the assumption made in Chapter 4 regarding vertical hydraulic conductivity being one-tenth of the horizontal hydraulic conductivity applies to the concrete elements as well. For the seawater, the default values provided by FEFLOW were considered.

Table 20. Material properties used during the numerical analysis on FEFLOW

	Property	Symbol	Unit	Value
SEAWATER	Horizontal hydraulic conductivity	k_{xx}	m/s	Default
	Vertical hydraulic conductivity	k_{yy}	m/s	Default
	Porosity	η	-	1
	Fluid-phase thermal conductivity	λ_w	W/mK	0.60
	Solid-phase thermal conductivity	λ_s	W/mK	Default
	Fluid-phase volumetric thermal capacity	$c_{p,w}$	MJ/m^3K	3.97
	Solid-phase volumetric thermal capacity	$c_{p,s}$	MJ/m^3K	Default
	Transverse dispersivity	α_T	m	0.3
	Longitudinal dispersivity	α_L	m	3.1
MARINE SEDIMENTS	Horizontal hydraulic conductivity	k_{xx}	m/s	$5.05x10^{-4}$
	Vertical hydraulic conductivity	k_{yy}	m/s	$5.05x10^{-5}$
	Porosity	η	-	0.53
	Fluid-phase thermal conductivity	λ_w	W/mK	0.60
	Solid-phase thermal conductivity	λ_s	W/mK	0.89
	Fluid-phase volumetric thermal capacity	$c_{p,w}$	MJ/m^3K	3.97
	Solid-phase volumetric thermal capacity	$c_{p,s}$	MJ/m^3K	0.83
	Transverse dispersivity	α_T	m	0.3
	Longitudinal dispersivity	α_L	m	3.1
ORTOVERO CLAYS	Horizontal hydraulic conductivity	k_{xx}	m/s	$5.05x10^{-7}$
	Vertical hydraulic conductivity	k_{yy}	m/s	$5.05x10^{-8}$
	Porosity	η	-	0.18
	Fluid-phase thermal conductivity	λ_w	W/mK	0.60
	Solid-phase thermal conductivity	λ_s	W/mK	2.34
	Fluid-phase volumetric thermal capacity	$c_{p,w}$	MJ/m^3K	3.97
	Solid-phase volumetric thermal capacity	$c_{p,s}$	MJ/m^3K	0.92
	Transverse dispersivity	α_T	m	0.3
	Longitudinal dispersivity	α_L	m	3.1
TUNNEL LINING	Horizontal hydraulic conductivity	k_{xx}	m/s	$1.00x10^{-16}$
	Vertical hydraulic conductivity	k_{yy}	m/s	$1.00x10^{-17}$
	Porosity	η	-	0
	Fluid-phase thermal conductivity	λ_w	W/mK	3.97
	Solid-phase thermal conductivity	λ_s	W/mK	1.12
	Fluid-phase volumetric thermal capacity	$c_{p,w}$	MJ/m^3K	3.97

	Solid-phase volumetric thermal capacity	$c_{p,s}$	MJ/m^3K	2.19
	Transverse dispersivity	α_T	m	0.3
	Longitudinal dispersivity	α_L	m	3.1
GROUT	Horizontal hydraulic conductivity	k_{xx}	m/s	$1.00x10^{-16}$
	Vertical hydraulic conductivity	k_{yy}	m/s	$1.00x10^{-17}$
	Porosity	η	-	0
	Fluid-phase thermal conductivity	λ_w	W/mK	0.60
	Solid-phase thermal conductivity	λ_s	W/mK	1.734
	Fluid-phase volumetric thermal capacity	$c_{p,w}$	MJ/m^3K	3.97
	Solid-phase volumetric thermal capacity	$c_{p,s}$	MJ/m^3K	2.19
	Transverse dispersivity	α_T	m	0.3
	Longitudinal dispersivity	α_L	m	3.1

5.4 Boundary conditions

Given that the analysis conducted involves a coupled thermo-hydraulic assessment, two types of boundary conditions can be established: hydraulic and thermal. Assigning these conditions to certain nodes will ensure that certain parameters remain constant throughout the simulation. For the Subport Tunnel of Genova, two thermal boundary conditions were initially implemented: at the top and bottom boundaries of the model while the hydraulic boundary condition was applied to the lateral boundaries.

At the top boundary, a time series representing the air temperature for the past five years, from January 1st 2019 to December 31st 2023, in the city of Genova was applied. For this purpose, the same meteorological station, Genova – Centro Funzionale (refer to Figure 18), was consulted to extract the numerical data. The temperature values were then imported as a time series into FEFLOW as illustrated in Figure 73. As explained in Section 5.2, the densification of the mesh at the top boundary must be carried out in advance in order to increase the precision of the results.

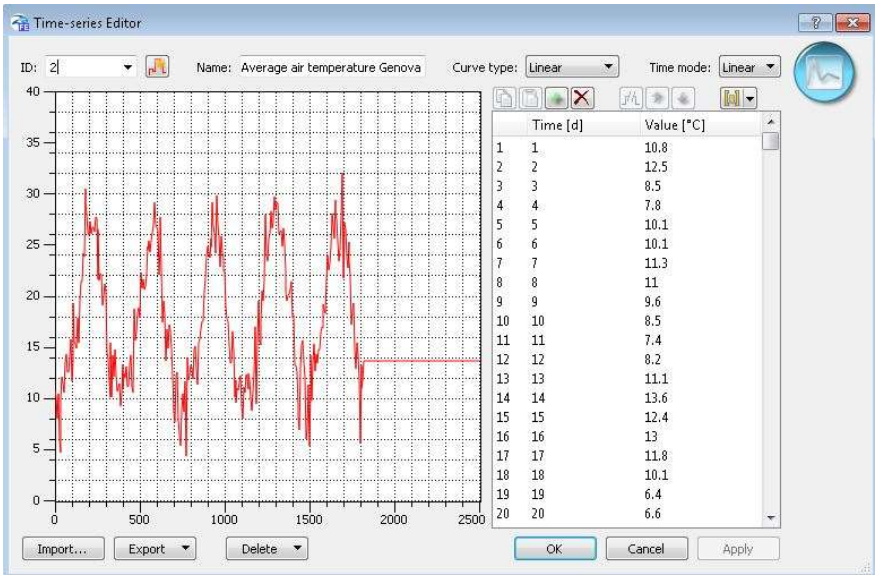

Figure 73. Time series of the air temperature for the years 2019 to 2023 in the city of Genova

Subsequently, a fixed temperature was imposed at the bottom boundary. The temperature assigned for the Dirichlet-type boundary condition was set constant to the annual air average temperature of 18.3 °C in the city of Genova, as shown in Figure 19. The final representation of the thermal boundary conditions across the 3D model is displayed in Figure 74.

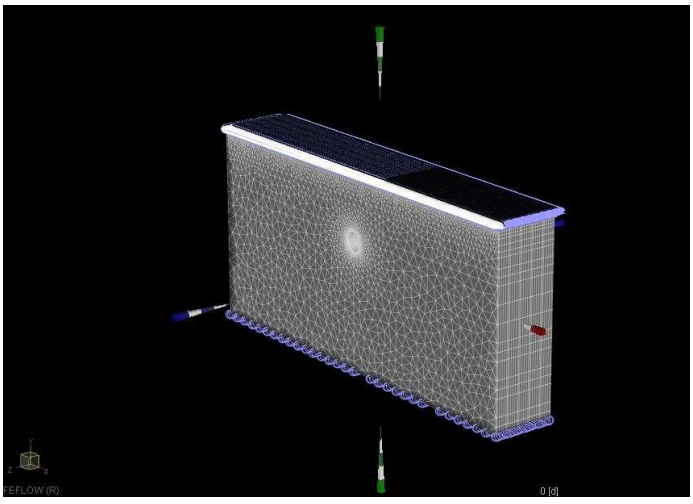

Figure 74. Thermal boundary conditions – 3D view

Additionally, in line with the thermal boundary conditions, a Dirichlet-type boundary condition was implemented as a hydraulic boundary condition, where a constant hydraulic head is established at the lateral sides of the model representing a fixed water level. To determine the value of the hydraulic head for this case, one can refer to Figure 60. The hydraulic head was defined as the sum of the seawater level (19 m), the thickness of the marine sediment layer (24 m), the tunnel radius (7.7 m) and the offset between the extrados and the marine sediment layer (nearly 1.26 m). Consequently, the fixed hydraulic head boundary condition was set at 51.96 m. Figure 75 illustrates the final representation of the hydraulic boundary condition across the 3D model.

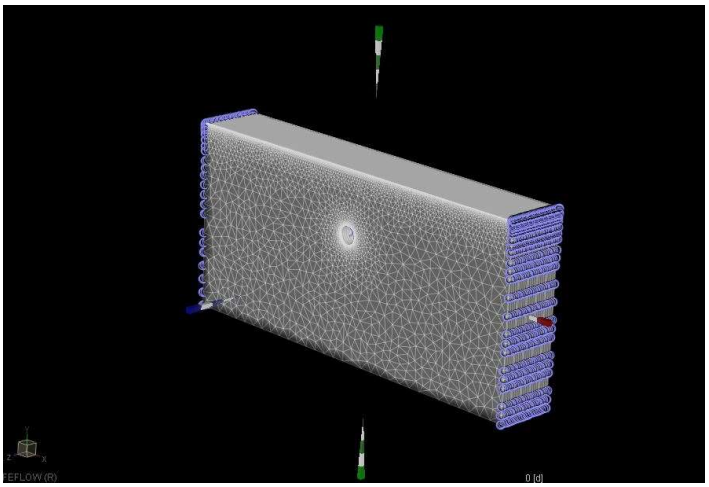

Figure 75. Hydraulic head boundary condition – 3D view

5.5 Initial conditions

Two distinct initial conditions need to be assigned to all nodes in the model: fluid flow (hydraulic head) and heat transport (temperature). For the latter, an initial temperature of 18.3 °C, corresponding to the annual average air temperature for the city of Genova, is applied to all the nodes. Since this is an initial condition, the temperature profile will evolve over the course of the simulation. It is expected that, ultimately, the temperature at the edges of the model will remain unchanged.

The second initial condition relates to the hydraulic head to be imposed, equal to 51.96 m throughout the domain. Due to the boundary conditions imposed on the left and right edges of the domain, no variation in the seawater level is expected during the analysis.

For this purpose, FEFLOW allows the creation of observation points, which are employed to monitor primary process variables (hydraulic head, temperature) at specified locations in the model domain. These points can either be positioned at nodal locations or freely placed. In this project, observation points were created in a separate DXF file, ensuring alignment with the reference system of the original file used to create the model. A total of 54 points were defined and converted into observation points in FEFLOW. They were placed 30 m away from the tunnel center and extended to the bottom of the model, with a spacing gradually increasing toward the bottom, as illustrated in Figure 76.

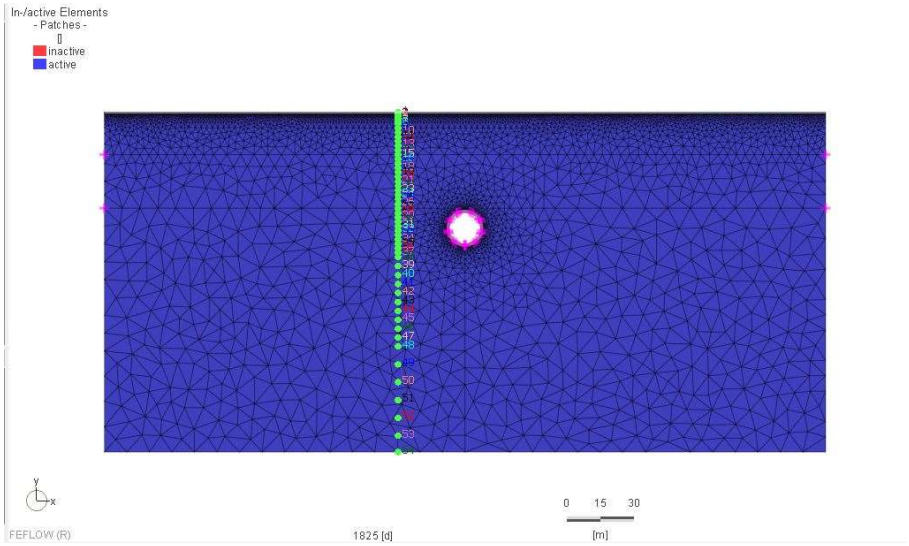

Figure 76. Observation points along the model – Slice view

Regarding the area near the top boundary, where the temperature boundary condition is applied as a time series, it was determined that the spacing between the observation points for the first 5 meters would be arranged as detailed in Table 21 in order to obtain a good representation of the ground temperature values. This table also shows the spacing of observation points at greater depths within model.

Table 21. Configuration of the observation points

Obs. Point ID	Depth [m]	Spacing [m]
1 - 5	0 - 2	0.5
5 - 8	2 - 5	1
8 - 38	5-65	2
38 - 48	65 - 105	4
48 - 54	105 – 152.3	8

5.6 Temperature initialization analysis

A preliminary step for the thermal activation of the tunnel consists of defining he initial thermal field of the ground. In this analysis, the temperature initialization phase was conducted without considering the presence of the heat exchange pipes in the tunnel lining modeled as discrete features on FEFLOW.

To initialize the model and define a representative thermo-hydraulic state, the initial time considered for this stage was set on January 1st 2019 where a temperature of 10.8 °C was registered as shown in Figure 73. It must be remarked that the temperature values were derived from the ARPA Liguria database as described in Section 5.4. The temperature initialization was carried out over a 5-year span until December 31st 2023, resulting in a total of 1825 days. The decision was based on the necessity for obtaining a long-term thermal equilibrium in order to simulate the thermal activation of the tunnel lining in a more effective was as will be described in Section 5.7.

Prior to the start of the simulation of the model, the Simulation Time-Control settings on the Problem Configuration menu (see Figure 77) must be adjusted according to the initial simulation time, the desired initial time-step length and the final simulation time, corresponding to 1825 days. The output times were established at every 5 days.

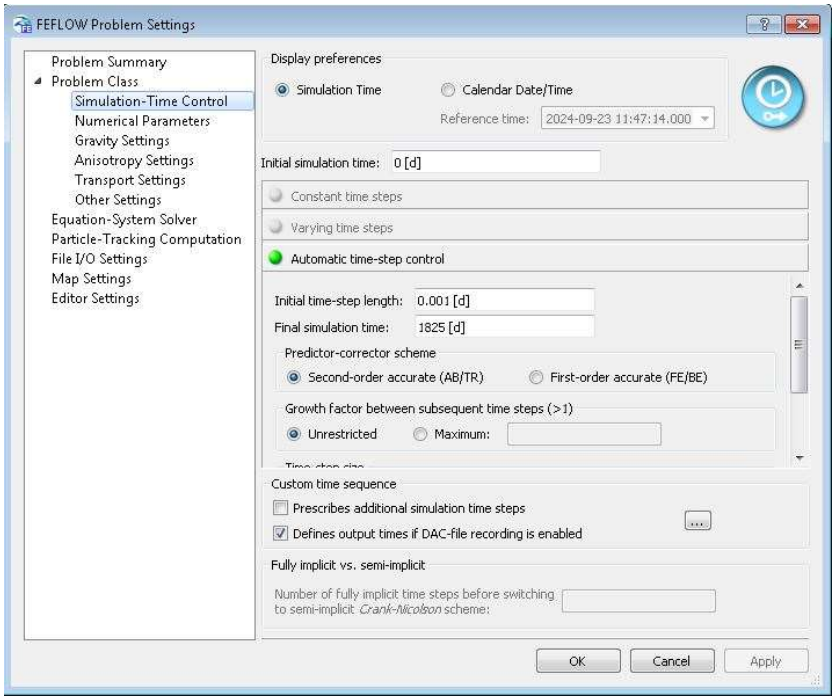

Figure 77. Simulation-Time Control settings on FEFLOW

Afterwards, the simulation can be initialized and simultaneously, monitor the local ground temperature history which provides the evolution of the temperature over time at the observation points location. Figure 78 depicts the trend of the ground temperature over time. The air temperature applied as a boundary condition at the top boundary shown in Figure 73 can be identified with the thick blue line, where observation point number 1 is located. Shallower depths display fluctuations in temperature over time up to nearly 13 m, where observation point number 12 is located. Such fluctuations can be detected in Figure 78 by analyzing the rest of the temperature curves, which indicate higher ground temperatures during winter and lower values during summer. Then, from a depth of 13 m it can be seen that the temperature displays constant values as illustrated in Figure 79 until the bottom boundary of the model was reached.

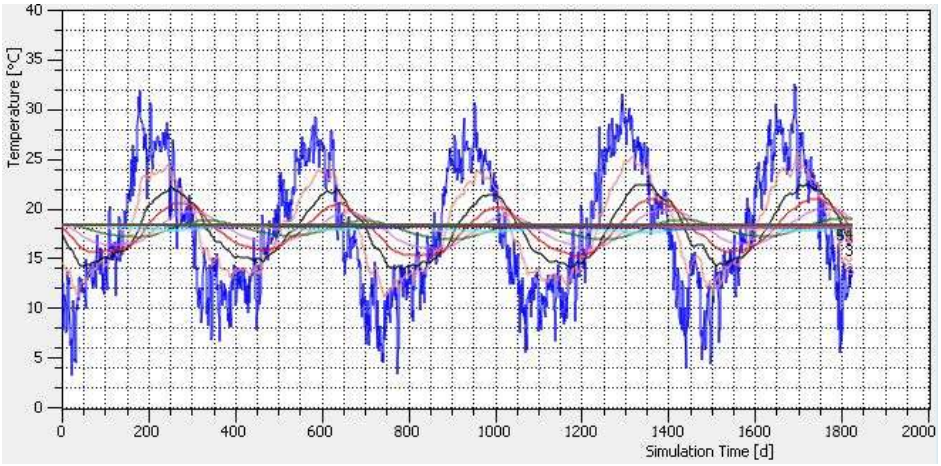

Figure 78. Plot of the local temperature history at the end of the simulation (1825 days)

5.7 Thermal activation of the tunnel lining

The primary objective of the thermal activation of the tunnel lining for this case study is to monitor the outlet temperature over time, which is a function of the heat transfer that is reproduced numerically during the simulation. As described in Section 2.3.3, the temperature difference between the inlet and outlet in the circuits together with the flow mass rate, m, (in kg/s) and the heat carrier fluid heat capacity, c, (in J/kg°C) lead to the calculation of the heat power, Q, in Watts as per Eq. 5. This parameter is of sum importance so a comparison can be established between the heat power calculated with FEFLOW through the correlation outlined in Eq. 5 and the total heat power calculated for the submerged section of the Subport Tunnel of Genova in Section 4.2 through the use of the nomograms depicted in Figure 7.

$$Q = mc(T_{out} - T_{in}) \qquad \textit{Eq. 15}$$

Firstly, the properties and dimensions of the heat carrier pipes included as discrete features in FEFLOW were defined based on the pipes employed in the Turin Metro Line 1 case study conducted by Barla & Insana (2020). Additionally, the type of heat transfer fluid and its properties, such as thermal and volumetric heat conductivity (λ_w and $c_{p,w}$, respectively) were assumed equal as the ones proposed by Barla et. al (2019), who employed a mix of 30% of propylene and 70% of water. Table 22 includes the summary and list of parameters considered for the thermal activation of the offshore section of the Subport Tunnel of Genova.

Table 22. Parameters used for the heat exchange pipes

Property	Symbol	Unit	Value
External diameter	d	mm	20
Pipe thickness	t	mm	2
Hydraulic radius	r	mm	8
Cross section area	A	mm^2	201.06
Fluid-phase thermal conductivity	λ_w	W/mK	0.423
Fluid-phase volumetric thermal capacity	$c_{p,w}$	MJ/m^3K	3.801

The second input is associated with the time series of the thermal activation phase during winter and summer. In order to define the winter time series, the system was assumed under operating conditions from November 1st to April 15th for every year, which corresponds to a typical heating period for the city of Genova since it falls under the climate zone B according to the Presidential Decree 16/04/13 n. 74. On the other hand, the summer time series were hypothesized from June 1st to August 31st for every year. With respect to the total thermal activation timeframe it was decided to carry out the simulations for a medium term (3 years) starting from November 1st, 2023 until August 31st, 2026. Figure 79 illustrates the temperature values across the domain for day 1675 of the thermal initialization, corresponding to November 1st, 2023, which will be considered as the initial date of the winter season as previously described.

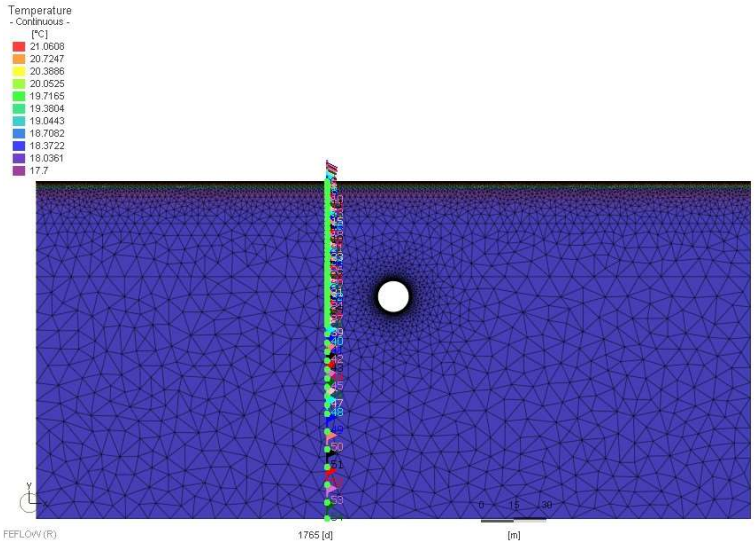

Figure 79. Thermal field of the model on November 1st, 2023

Thereafter, three aditional time series were created in order to apply the inlet temperature as well as the inlet and outlet velocity. The inlet temperature values were extracted from the ranges proposed by Barla & Insana (2022). An inlet temperature of 28 °C is considered for summer when excess heat is dispersed in the ground. Conversely, inlet temperature in winter was set at 4 °C, when heat extraction from the ground occurs. In order to neglect the timeframes where the system is not in operating conditions, the "gap" function in FEFLOW can be activated as Figure 80 suggests. On the other hand, inlet and outlet velocities were considered as -0.9 and 0.9 m/s, respectively, and were also derived from Barla & Insana (2022). Lastly, observation points were inserted at the pipe outlets with the aim of monitoring the temperature, T_{out}, that will be employed to calculate the heat power, Q, in Eq. 5.

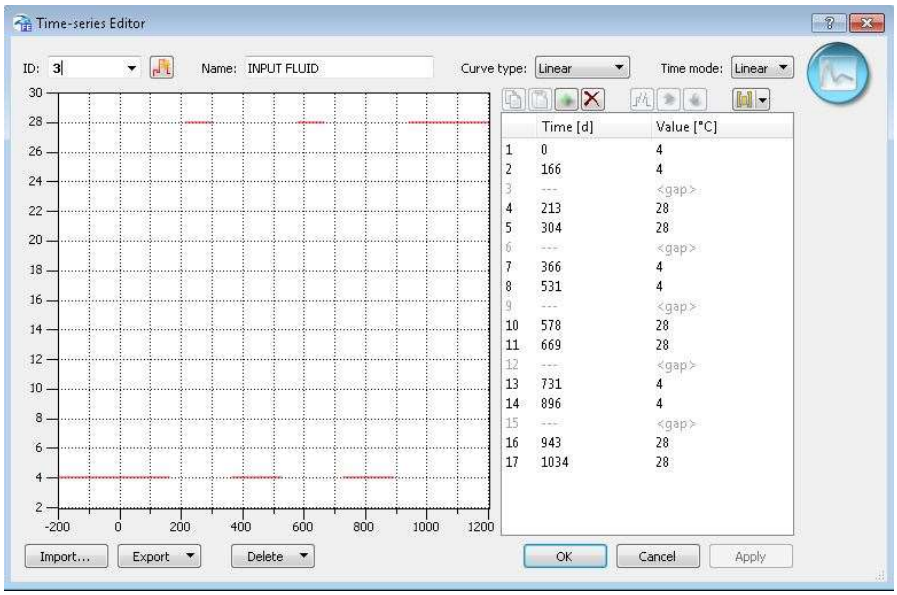

Figure 80. Time series of the input fluid

It must also be remarked that the time series of the air temperature boundary condition applied at the top, illustrated in Figure 73 was modified in order to make it coincident with the starting date of the thermal activation which is November 1st, 2023. For simulations in the future, namely from January 1st, 2024 and onwards, the last available time series was repeated cyclically. Nevertheless, one relevant aspect to take into account is that in the nomograms, winter and summer seasons are simulated separately. Thus, in the present Thesis two different conditions are reproduced:

- Condition A: The tunnel was considered adiabatic, therefore, no heat exchange occurs and winter and summer seasons are simulated simultaneously.
- Condition B: The tunnel was considered diabatic and winter and summer seasons were simulated separately. Therefore, two models were created:
    - B.1: The model was simulated starting from the first winter season on November 1st, 2023.
    - B.2: The model was simulated starting from the summer season (June 1st, 2024) without considering the initial winter season.

To ensure heat exchange within the tunnel, an additional Dirichlet-type thermal boundary condition was applied at the intrados nodes fixing the tunnel temperature as the ground temperature equal to 18.3 °C. In addition, a heat transfer coefficient of 5.3 W/m^2K was assigned to the intrados based on the study conducted by Barla & Insana (2020).

5.8 Interpretation of the results

The models were run and output times were defined for each day of the considered timeframe. However, it is important to note that the nomograms depicted in Figure 7 comprise values of the heat flux, q (in W/m^2), after 30 days of simulation. For this purpose, Table 23 contains the results from each numerical model, A, B.1 and B.2, after 30 days of simulation and at the outlet located in the central ring of the tunnel, where:

- ΔT is the temperature difference between the outlet and the inlet, expressed in °C.
- Q, the heat power expressed in kW, is calculated according to Eq. 5, and depends on ΔT, the mass flow rate (m) equal to 0.19 kg/s computed as per Eq. 16 , and the heat capacity of the heat carrier fluid (c) equal to 3801 J/kg°C for 70%-30% water-propylene glycol mix.

$$m = \rho \cdot A \cdot v \qquad \textit{Eq. 16}$$

with:

ρ as the density of the water-propylene glycol mix in equal to 1035.93 kg/m^3.

A as the internal cross section area of the heat exchange pipe in m^2.

v as the inlet velocity applied to the pipes, equal to 0.9 m/s.

- q is the heat flux, expressed in W/m^2, and calculated according to Eq. 17.

$$q = \frac{Q}{2 \cdot \pi \cdot R \cdot L_{ring}} \qquad Eq.\ 17$$

where:

Q is the heat power calculated with Eq. 5.

R is the radius of the ring, equal to 7.7 m.

L_{ring} is the length of the ring, equal to 2 m since the rings are all connected in parallel.

- The last column, Q, expressed in MW, corresponds to the total heat power exploited along the total length of the offshore section (450 m).

Table 23. Comparative analysis of the results after 30 days of the numerical simulation

Condition	Year	Timeframe	ΔT [°C]		Q [kW]		q [W/m²]		Q [MW]	
			Winter	Summer	Winter	Summer	Winter	Summer	Winter	Summer
A	1	01/11/23 - 31/08/24	1.51	1.79	1.08	1.28	11.13	13.20	0.24	0.35
	2	01/11/24 - 31/08/25	1.69	1.81	1.21	1.29	12.47	13.29	0.27	0.35
	3	01/11/25 - 31/08/26	1.70	1.82	1.21	1.29	12.52	13.37	0.27	0.36
B.1	1	01/11/23 - 31/08/24	4.53	3.34	3.23	2.38	33.37	24.61	0.73	0.54
	2	01/11/24 - 31/08/25	4.57	3.35	3.25	2.39	33.62	24.67	0.73	0.54
	3	01/11/25 - 31/08/26	4.57	3.36	3.26	2.40	33.67	24.75	0.73	0.54
B.2	1	01/06/24 - 15/04/25	4.67	3.08	3.33	2.19	34.40	22.65	0.75	0.49
	2	01/06/25 - 15/04/26	4.60	3.33	3.28	2.37	33.87	24.51	0.74	0.53
	3	01/06/26 - 31/08/26	-	3.36	-	2.39	-	24.73	0.73	0.54

Furthermore, Table 24 provides the heat flux values derived from the interpretation of the nomograms in order to make the comparisons with the results obtained from the numerical analysis. Temperature classes 1, 2 and 3 are applicable to the submerged section of the tunnel as described in Section 4.2. It is also worth recalling that the total heat power along the submerged section resulted in 0.84 MW for winter and 0.36 MW during summer employing the nomograms.

Table 24. Heat flux, q, derived from the nomograms applicable to the tunnel section under the sealevel

Class	T [°C]	q [W/m^2]	
		Winter	Summer
1	14-15	32	18
2	15-16	36	13
3	16-17	39	10

Subsequently, a few comments can be made regarding the different results obtained for each parameter in Table 23. As expected, the results show that considering the tunnel adiabatic (condition A), lower values for each parameter are expected in comparison with a diabatic tunnel where heat exchange occurs. Interestingly, it can be noted that for the summer season, the heat flux obtained falls within the range derived from the nomograms (10 to 18 W/m^2) as presented in Table 24. In contrast, the computed heat flux during winter in Table 23 falls short of the range established from the nomograms equal to 32 to 39 W/m^2.

With respect to the evolution in time for the case of an adiabatic tunnel, it can be seen that the parameters increase especially in winter, where for the third year a temperature difference, ΔT, increased by 0.19 °C from the first year, resulted in the largest temperature difference computed in winter among the three case studies.

When considering a diabatic tunnel, as in case B.1, it is evident that the results for the winter season are enhanced up to 33 W/m^2 now coinciding with the range of the heat flux derived from the nomograms. In this context, a large portion of the heat in winter can be mostly attributed to the internal air of the tunnel after applying the boundary condition at the intrados. Nevertheless, the heat fluxed obtained for the summer season were also affected, falling outside of the range employed during the nomograms interpretation by nearly 7 W/m^2 On the other hand, looking at the results from simulation B.2, which started on June 1st, 2024, the results do not vary considerably for the winter season while a slight improvement is observed for the

first year of the thermal activation during summer, reaching a heat flux equal to 22.65 W/m^2. However, the heat flux still differs by more than 6 W/m^2 of the largest value used for summer in Table 23. The higher value in summer can be attributed to the lower temperature value of the tunnel that was applied as a Dirichlet-type boundary condition at the tunnel intrados for summer. Such value was considered equal to the ground temperature (18.3 °C), while in the design of the nomograms a tunnel temperature of 29.7 °C in summer was assumed for a ground temperature of 18°C with the aim of reducing heat. Consequently, results during summer are expected to decrease if further simulations are carried out considering the same value as the one assumed for the nomograms.

Furthermore, with regard to the total heat power along the offshore section, a few comments can be made. For case B.1 and B.2, the power calculated in winter as a result of the simulations and postprocessing, slightly differs with the value calculated employing the nomograms. This can be attributed to the heat flux, q, since in the nomograms a range is considered depending on the ground temperature of the offshore section and in the numerical simulation a unique value is derived from the outputs with the use of Eq. 17. In summer, a considerable difference of the power is obtained from the simulations in comparison with the value obtained from the nomograms for the reasons aforementioned.

Finally, the estimated geothermal potential per meter for the section of interest during winter and summer for the conditions listed in Table 23 is shown in Figure 81, Figure 82, Figure 83 and Figure 84 in the Appendix A section. These values were subsequently compared to Figure 41 and Figure 42, which correspond to the estimated potential computed employing the design nomograms. Condition B.1 and B.2 display nearly identical values in the geothermal potential per meter as outlined in the figures and Table 25 since they both consider the tunnel diabatic and winter and summer seasons are simulated separately. Conversely, condition A displays a geothermal potential in the same range as Figure 42 for the summer season whereas for winter, the potential is clearly low in comparison.

Table 25. Values of the geothermal potential per meter as a result of the numerical simulations

	Q [W/m]	
Condition	**Winter**	**Summer**
A	582.7	785.7
B.1	1623.4	1193.8
B.2	1644.6	1159.3

Conclusion

This Thesis was devoted on the feasibility of the integration of geothermal energy systems within tunnel infrastructures, addressing their potential for sustainable heating and cooling applications through the interpretation of design charts and numerical simulations. As the title suggests, the present Thesis outlines and compares three different Italian underground projects, namely: the Subport Tunnel of Genova, the Trento Ring road tunnel and the Cortina d'Ampezzo tunnel. Each project is characterized by distinct unique features that are described in the geothermal, geotechnical and hydrogeological sections. The adopted methodology, which encompassed theoretical research, quantitative and numerical analysis, offers notable contributions to the energy geostructures field especially in the case of the Subport Tunnel of Genova, since little or no information could be found regarding the thermal activation of a tunnel lining in a submerged section of the tunnel.

The geothermal potential of each tunnel was firstly estimated by dividing the tunnel chainage into homogeneous sections characterized by similar lithology, ground temperature, and groundwater conditions. This method allowed to calculate the specific heat power, which was assumed homogeneous for the aforementioned sections. The total heat power along the chainage was estimated as the sum of the specific heat power of each section along the chainage. To achieve this, the nomograms depicted in Figure 7 were critical to estimate the specific heat power for each section during both summer and winter. The most conservative approach was followed in this Thesis at the moment of estimating the geothermal potential for the three case studies. The most critical conditions such as a null groundwater flow and parallel to the tunnel axis were assumed due to the lack of available data gathered from the technical reports. Thus, the results found in this Thesis may increase if future in-situ tests are conducted in order to obtain the characteristics of the flow.

In summary, the geothermal potential was higher in winter than in summer for the three tunnels except for the Cortina d'Ampezzo case study, which exhibited a 0.385 MW higher total heat power in summer. This phenomenon was attributed to the low ground temperature at the site, which ranged between 8 °C and 15 °C. From the results obtained, a trend was clearly identified for the three tunnels when the temperature becomes the governing parameter, since a steady state of the

groundwater is considered. As ground temperature rises, the extracted geothermal potential in winter is higher whereas for decreasing temperatures, the geothermal potential results in lower values. For the summer season, the opposite can be concluded since the primary goal is to inject heat into the ground. Thus, larger ground temperatures lead to lower values of the geothermal potential that can be exploited while lower values of temperature translate into a high geothermal potential.

Another interesting finding derived from the nomograms interpretation in the case of the Subport Tunnel of Genova is the proportion of heat power that the offshore section provides to the total chainage during summer since 0.36 of the 1.05 MW are estimated for the offshore section, which amounts to slightly over one-third of the total heat power in winter. It must be remarked that only 450 m of the nearly 3.5 km chainage are located beneath the seawater level. Thus, significant benefits can be expected if the tunnel lining of the Genova case study is thermally activated along the specified section. With respect to the Trento ring road, the key finding consisted of the largest number of homogeneous sections (30) along the 10.65 km chainage among the three projects and the largest geothermal potential that can be extracted during winter. In addition, the largest temperature difference between the tunnel portals and the central section of the chainage is observed for this tunnel due to its high depths, where the ground temperature varies from 13 to 20 °C. Such elevated temperatures lead to extreme heat fluxes both in summer and winter, where heat fluxes ranging from 46 to 49 W/m^2 are expected for ground temperatures higher than 18 °C in winter. On the other hand, heat fluxes between 3 and 5 W/m^2 are expected in summer.

Finally, a thorough analysis of the Subport Tunnel of Genova was carried out through numerical simulations in the finite element software FEFLOW. The primary motivation was to compare the geothermal potential obtained from numerical calculations with that derived from the nomograms, in order to assess their validity for case studies that differ from those they were originally designed for. In particular, compared to the Turin Metro Line 1, the Subport Tunnel of Genova has slightly twice the diameter and includes a submerged section beneath the seawater. For this purpose, two conditions were modeled and compared: a) condiering an adiabatic tunnel and winter and summer seasons simulated simultaneously and b) considering a diabatic tunnel and simulating winter and summer seasons separately as was carried out for the design nomograms. It must be added that the results are only applicable to the section where similar conditions are expected, thus, along the 450 m submerged section.

The results for case a) show some discrepancy with the findings employing the nomograms during the winter season as a lower geothermal potential is obtained. Conversely, the values in summer demonstrate good correlation with the findings from the nomogram. On the other hand,the results for condition b) are practically identical to the nomogram estimates during winter, whereas for summer, a higher geothermal potential is observed. The primary motive for the higher summer values is related to the thermal boundary condition applied at the tunnel intrados. This choice of boundary condition significantly influenced the summer results, leading to the elevated geothermal potential estimates compared to the predictions from the nomograms.

Based on the results obtained it was possible to prove the efficiency of the design nomograms for a preliminary estimation of the geothermal potential, even when applied to case studies quite different from the geothermal and geotechnical point of view as well as dimensions of the Turin Metro Line. However, it is relevant to pay careful attention to key factors, such as the thermal boundary conditions, as these charts were developed based on certain assumptions. For instance, the charts were constructed by hypothesizing specific tunnel temperatures (29.7 °C) relative to a ground temperature equal to (18.3 °C). Therefore, while nomograms provide a reliable preliminary estimate, site-specific conditions must always be carefully considered, if available, to ensure precision and accuracy.

In conclusion, the present Thesis demonstrates that considerable energy exploitation can be fulfilled for all three case studies, in spite of significant differences in location, geology and climate. For instance, the Subport Tunnel of Genova, which is located in a densely populated area, may be beneficial for employing the geothermal energy harnessed at the tunnel portals in order to supply surrounding buildings or contribute to a district heating network, as described in paragraph 2.3.4. On the other hand, the Cortina D'Ampezzo tunnel, situated in a mountainous region, offers the opportunity to exploit the geothermal energy for deicing bridges such as the North and South bridges over the Boite river or roads at the tunnel portals, especially during the winter, when the geothermal potential is the highest. Lastly, the Trento ring road tunnel, with close proximity to the city center of Trento, could also be used for harvesting geothermal energy and serve as a steady source of heating and cooling for nearby infrastructure.

References

Adam, D., & Markiewicz, R. (2009). Energy from earth-coupled structures, foundations, tunnels and sewers. *Géotechnique*, 229–236. doi:10.1680/geot.2009.59.3.229

Almousa, N., Alotaibi, M., Alsohybani, M., Radziszewski, D., Ainoman, S., Aiotaibi, B., & Khayyat, M. (2021). Paraffin Wax [As a Phase Changing Material (PCM)] Based Composites Containing Multi-Walled Carbon Nanotubes for Thermal Energy Storage (TES) Development. *Crystals, 11*. doi:10.3390/cryst11080951

Alvi, M. R. (2021). *Valutazione delle potenzialita' geotermiche della galleria di base della Torino-Lione.* Torino: Master's degree thesis. Politecnico di Torino.

Alvi, M. R., Barla, M., & Insana, A. (2022). Thermal performance assessment of an energy lining for the Lyon-Turin base tunnel. *International Journal of Geotechnical and Geoenvironmental Engineering*, 1-12. doi:https://doi.org/10.28927/SR.2022.000722

Amiri, M., Dehghani, M., & Papi, M. (2022). Microstructural Evaluation of Thermal Stabilization of Marl Soils Considering Permeability Variations. *Research Square*. doi:https://doi.org/10.21203/rs.3.rs-311733/v1

Anas Gruppo FS Italiane. (2021). *Progetto Stradale. Relazione di elaborati generali.* S.S 51 - Variante di Cortina. Profetto Definitivo.

Anas Gruppo FS Italiane. (2023). *Lotto 2 - Studi e indagini. Geologia e idrogeologia: carta idrogeologica.* S.S 51 Variante di Cortina. Progetto di fattibilita' tecnico economica.

Anas Gruppo FS Italiane. (2023). *Lotto 2 - Studi e indagini: Geotecnica. .* S.S.51 - Variante di Cortina: Progetto di Fattibilita' tecnico economica.

Anas Gruppo FS Italiane. (2023). *Parte generale. Inquadramento - Relazione generale.* Progetto di fattibilita' tecnico economica "S.S 51 Variante di Cortina".

Andújar Márquez, J. M., Martínez Bohórquez, M. Á., & Gómez Melgar, S. (2016). Ground Thermal Diffusivity Calculation by Direct Soil Temperature Measurement. Application to very Low Enthalpy Geothermal Energy Systems. *Sensors (Basel, Switzerland), 16*. doi:https://doi.org/10.3390/s16030306

ASTM. (2014). *Standard Test Method for Determination of Thermal Conductivity of Soil and Soft Rock by Thermal Needle Probe Procedure.* West Conshohocken: ASTM International.

Autostrade per l'Italia. (2021). *Tunnel Subportuale Urbano di attraversamento della citta' di Genova. "Relazione geomeccanica galleria naturale".*

Autostrade per l'Italia. (2021). *Tunnel subportuale urbano di attraversamento della citta' Genova. Lotto 1- Tunnel Subportuale. Progetto definitivo "Tunnel - Galleria principale".* Ministero delle infrastrutture e dei trasporti.

Autostrade per l'Italia. (2021). *Tunnel subportuale urbano di attraversamento della citta' Genova. Progetto di fattibilita' tecnico-economica. "Relazione di caraterizzazione geotecnica Imbocco S. Benigno (Ovest)".* Ministero delle infrastrutture e dei trasporti.

Autostrade per l'Italia. (2021). *Tunnel Subportuale Urbano di Attraversamento della Citta' Genova. Progetto Definitivo - Galleria principale. "Relazione tecnica preliminare e di calcolo paratie imbocco e strutture provvisionali".* Ministero delle Infrastrutture e dei trasporti.

Autostrade per l'Italia. (2021). *Tunnel Subportuale Urbano di Attraversamento della Citta' Genova. Progetto di Fattibilita' Tecnico-economica. "Relazione generale".* Ministero delle Infrastrutture e dei Trasporti.

Autostrade per l'Italia. (2021). *Tunnel Subportuale Urbano di Attraversamento della Citta' Genova. Progetto di Fattibilita' Tecnico-economica. "Relazione tecnica".* Ministero delle Infrastrutture e dei transporti.

Autostrade per l'Italia. (2021). *Tunnel subportuale urbano di attraversamento. Progetto di fattibilita' tecnico-economica. "Relazione tecnica architettonica".* Ministero delle infrastrutture e dei trasporti.

Autostrade per l'Italia. (2022). *Profili longitudinali. Profilo geotecnico galleria naturale principale - Asse Nord.* Tunnel subportuale urbano di attraversamento della citta' di Genova: Progetto definitivo.

Autostrade per l'Italia. (2022). *Profilo geotecnico galleria naturale - Rampa Madre di Dio verso centro.* Tunnel subportuale urbano di attraversamento della citta' di Genova: Progetto definitivo.

Autostrade per l'Italia. (2022). *Profilo geotecnico galleria naturale principale - Asse Sud.* Tunnel subportuale urbano di attraversamento della citta' di Genova: Progetto definitivo.

Bandini, A., Berry, P., Cormio, C., Colaiori, M., & Lisardi, A. (2017). Safe excavation of large section tunnels with Earth Pressure Balance Tunnel Boring Machine in gassy rock masses: The Sparvo tunnel case study. *Tunnelling and Underground Space Technology, 67*, 85-97.

Baralis, M., Barla, M., & Insana , A. (2020). Energy Tunnels for Deicing of a Bridge Deck in Alpine Region. *Challenges and innovation in Geomechanics, Proc. of the 16th International Conference of IACMAG 2020*, 1061-1068.

Baralis, M., Barla, M., Bogusz, W., Di Donna, A., Ryżyński, G., & Żeruń, M. (2018). Geothermal Potential of the NE Extension Warsaw Metro Tunnels. *Environmental Geotechnics, 7*, 1-37. Retrieved from 10.1680/jenge.18.00042

Barla, G. B., Barla, M., Bonini, M., Debernardi , D., Perino, A., Antolini, F., & Gilardi, M. (2015). 3D thermo-hydro modeling and real-time monitoring for a geothermal system in Torino, Italy. *Intervento presentato al convegno XVI ECSMGE tenutosi a Edinburgh nel 13-17 September 2015*, 2481-2486. doi:10.1680/ecsmge.60678

Barla, M., & Di Donna, A. (2016). Editorial. *Environmental Geotechnics*, 188-189. doi:http://dx.doi.org/10.1680/jenge.2016.3.4.188

Barla, M., & Insana, A. (2020). Experimental and numerical investigations on the energy performance of a thermo-active tunnel. *Renewable Energy*, 781-792. doi:https://doi.org/10.1016/j.renene.2020.01.086

Barla, M., & Insana, A. (2022). Energy tunnels as an opportunity for sustainable development of urban areas. *Tunneling and Underground Space Technology*, 1-16. doi:https://doi.org/10.1016/j.tust.2022.104902

Barla, M., Baralis, M., Insana, A., Aiassa, S., Antolini, F., Azzarone , F., & Marchetti, P. (2019). Feasibility study for the thermal activation of Turin Metro Line 2. *Tunnels and Underground Cities: Engineering and Innovation meet Archaeology, Architecture and Art– Peila, Viggiani & Celestino*, 231-240.

Barla, M., Di Donna, A., & Insana, A. (2019). A novel real-scale experimental prototype of energy tunnel. *Tunnelling and Underground Space Technology*, 1-14. doi:https://doi.org/10.1016/j.tust.2019.01.024

Barla, M., Di Donna, A., & Perino, A. (2016). Application of energy tunnels to an urban environment. *Geothermics, 61*, 104-113. doi:10.1016/j.geothermics.2016.01.014

Bidarmaghz, A., Makasis, N., Fei, W., & Narsilio, G. (2023). An efficient and sustainable approach for cooling underground substations. *Tunnelling and Underground Space Technology*, 1-10. doi:https://doi.org/10.1016/j.tust.2021.103986

Bossi, G. (2015). *Statistical analysis of the error associated with the simplification of the stratigraphy in geotechnical models.* Bologna: PhD thesis in civil, environmental and material engineering. University of Bologna.

Brandl, H. (2006). Energy foundations and other thermo-active ground structures. *Géotechnique*, 81-122.

Brandl, H. (2013). Thermo-Active Ground-Source Structures for Heating and Cooling. *11th International Conference on Modern Building Materials, Structures and Techniques*, 9-18. doi:10.1016/j.proeng.2013.04.005

Bryant, W. R. (2003). Permeability of Clays, Silty-Clays and Clayey-Silts". In E. D. Scott, B. A. H., & W. R. Bryant, *Siltstones, Mudstones and Shales: Depositional Processes and Characteristics.* SEPM Society for Sedimentary Geology. doi:https://doi.org/10.2110/sepmmisc.01

Bunton, D. (2002). Generic moves in PhD thesis introductions. In J. Flowerdew, *Academic discourse* (pp. 57-75). London: Pearson Education Limited.

Cousin, B., Rotta Loria, A., Bourget, A., Rognon, F., & Laloui, L. (2019). Energy performance and economic feasibility of energy segmental linings for subway tunnels. *Tunnelling and Underground Space Technology*, 1-13. doi:https://doi.org/10.1016/j.tust.2019.102997

Dalla Santa, G., Galgaro, A., Sassi, R., Cultrera, M., Scotton, P., Mueller, J., . . . Cassiani, G. (2020). An updated ground thermal properties database for GSHP applications. *Geothermics, 85*. doi:https://doi.org/10.1016/j.geothermics.2019.101758

Dalla Santa, G., Peron, F., Galgaro, A., Cultrera, M., Bertermann, D., Müller, J., & Bernardi, A. (2017). Laboratory Measurements of Gravel Thermal Conductivity: An Update Methodological Approach. *Energy Procedia, 125*, 671-677. doi:10.1016/j.egypro.2017.08.287

Delage, P. (2013). On the thermal impact on the excavation damaged zone around deep radioactive waste disposal. *Journal of Rock Mechanics and Geotechnical Engineering*, 179-190. doi:http://dx.doi.org/10.1016/j.jrmge.2013.04.002

DHI-Wasy. (2013). *Finite Element Subsurface Flow & Transport Simulation System. User Manual.* Retrieved from https://aquaknow.jrc.ec.europa.eu/system/files/DHI-WASY%20-%202013%20-%20Feflow%206.2%20user%20manual.pdf

Di Donna, A., & Barla, M. (2016). The role of ground conditions on energy tunnels' heat exchange. *Environmental Geotechnics*, 214-224. doi:https://doi.org/10.1680/jenge.15.00030

Duffield, G. M. (2019, November 23). *Representative Values of Hydraulic Properties*. Retrieved from http://www.aqtesolv.com/aquifer-tests/aquifer_properties.htm

Eswara, R., Labani, R. T., & Ravi, G. (2022). Thermal conductivity, density and porosity of sedimentary and metamorphic rocks from the Lower and Higher Himalaya, Western Himalaya, India. *Geophysical Journal International, 231*, 459–473. doi:https://doi.org/10.1093/gji/ggac176

European Union. (2016). Overview of support activities and projects of the European Union on energy efficiency and renewable energy in the heating and cooling sector. *Publications Office of the European Union*, 3-4.

Franzius, J. N., & Pralle, N. (2011). Turning segmental tunnels into sources of renewable energy. *ICE Proceedings Civil Engineering*, 35-40. doi:10.1680/cien.2011.164.1.35

Frisia Bruni, S., & Wenk, H. R. (1985). Replacement of aragonite by calcite in sediments from the San Cassiano Formation (Italy). *Journal of Sedimentary Research*, 159–170. doi:https://doi.org/10.1306/212F8652-2B24-11D7-8648000102C1865D

Frodl, S., Franzius, J. N., & Bartl, T. (2010). Design and construction of the tunnel geothermal system in Jenbach. *Tunnel Engineering*, 2-11. doi:10.1002/geot.201000037

Gattolin, G., Breda, A., & Preto, N. (2013). Demise of Late Triassic carbonate platforms triggered the onset of a tide-dominated depositional system in the Dolomites, Northern Italy. *Sedimentary Geology, 297*, 38-49. doi:https://doi.org/10.1016/j.sedgeo.2013.09.005.

Georgieva, M. (2016). Effective porosity and mineral composition of marl from the Sumer Formation. *Geological Institute, Bulgarian Academy of Sciences*, 147-148.

Geotechdata.info. (2013, October 7). *Soil permeability coefficient*. Retrieved from https://www.geotechdata.info/parameter/permeability

Geotechdata.info. (2013, November 18). *Soil porosity*. Retrieved May 1, 2024, from https://www.geotesting.info/parameter/soil-porosity.html

Goto, S., & Matsubayashi, O. (2009). Relations between the thermal properties and porosity of sediments in the eastern flank of the Juan de Fuca Ridge. *Earth Planets and Space, 61*, 863-870. doi:10.1186/BF03353197

Gregg, J. (1987). Classification of Dolomite Rock Textures. *Journal of Sedimentary Research, 57*. doi:10.1306/212F8CBA-2B24-11D7-8648000102C1865D

Guo, H., Lin, Y., Sun, C., Mao, X., & Li, J. (2023). Effect of temperature on the dynamic parameters of silty clay in a seasonally frozen region. *Scientific Reports, 13*. doi:10.1038/s41598-023-40261-y

Hailemariam, H., & Wuttke, F. (2022). An Experimental Study on the Effect of Temperature on the Shear Strength Behavior of a Silty Clay Soil. *Geotechnics, 2*. doi:10.3390/geotechnics2010011

Heap, M., Russell, J., & Kennedy, L. (2016). Mechanical behaviour of dacite from Mount St. Helens (USA): A link between porosity and lava dome extrusion mechanism (dome or spine)? *Journal of Volcanology and Geothermal Research, 328*. doi:https://doi.org/10.1016/j.jvolgeores.2016.10.015

Insana, A. (2020). *Thermal and Structural Performance of Energy Tunnels.* Torino: Politecnico di Torino.

Insana, A., & Barla, M. (2020). Experimental and numerical investigations on the energy performance of a thermo-active tunnel. *Renewable Energy*, 781-792. doi:https://doi.org/10.1016/j.renene.2020.01.086

Integrated Environmental Solutions Limited. (2021). *Table 6 Thermal Conductivity, Specific Heat Capacity and Density*. Retrieved May 1, 2024, from https://help.iesve.com/ve2021/table_6_thermal_conductivity__specific_heat_capacity_and_density.htm

Islam, S., Fukuhara, T., Watanabe , H., & Nakamura, A. (2006). Horizontal U-Tube Road Heating System using Tunnel Ground Heat. *Journal of Snow Engineering of Japan*, 229-234.

Italferr. (2021). *Galleria Trento-Profilo geotecnico.* Progetto di fattibilita' tecnica ed economica. Lotto 3A: Circonvallazione di Trento.

Italferr. (2021). *Gallerie naturali - Scavo meccanizzato - Sezione tipo di avanzamento e carpenteria anello.*

Jong van Lier, Q. d., & Durigon, A. (2013). Soil thermal diffusivity estimated from data of soil temperature and single soil component properties. *Revista Brasileira de Ciência do Solo, 37*. doi:10.1590/S0100-06832013000100011

Karu, V. (2012). Potential Usage of Underground Mined Areas in Estonian Oil Shale Deposit. *Thesis for: PhD, Energy and geotechnology*.

Kumar, A. (2007). *Temperature inside the landfill: effects of liquid injection and ambient temperature.* Orlando, Florida: College of Engineering and Computer Science at the University of Central Florida. Retrieved April 25, 2024

Kwan, B. S. (2009). Reading in preparation for writing a PhD thesis: Case studies of experiences. *Journal of English for Academic Purposes*, pages 180-191.

LaRowe, D., Burwicz-Galerne, E., Arndt, S., Dale, A., & Amend, J. (2017). Temperature and volume of global marine sediments. *Geology, 45*. doi:10.1130/G38601.1

Lee, C., Park, S., Won, J., Jeoung, J., Sohn, B., & Choi, H. (2012). Evaluation of thermal performance of energy textile installed in Tunnel. *Renewable Energy*, 11-22. doi:http://dx.doi.org/10.1016/j.renene.2011.09.031

Lintao, Y., Marshall, A. M., & Wanatowski, D. (2017). Effect of high temperatures on sandstone – a computed tomography scan. *International Journal of Physical Modelling in Geotechnics*, 75-90. doi:https://doi.org/10.1680/jphmg.15.00031

López-Acosta, N. P., Portillo-Arreguín, D. M., Barba-Galdámez, D. F., & Singh, R. M. (2022). Thermal properties of soft clayey soils from the former Lake Texcoco in Mexico. *Geomechanics for Energy and the Environment, 32*. doi:https://doi.org/10.1016/j.gete.2022.100376

Lund, J., & Boyd, T. (2015). Direct utilization of geothermal energy 2015 worldwide review. *Geothermics*, 66-93. doi:http://dx.doi.org/10.1016/j.geothermics.2015.11.004

Meibodi, S. S., & Loveridge, F. (2022). The future role of energy geostructures in fifth generation district heating and cooling networks. *Energy*, 1-16. doi:https://doi.org/10.1016/j.energy.2021.122481

Menegoni, N., Inama, R., Crozi, M., & Perotti, C. (2022). Early deformation structures connected to the progradation of a carbonate platform: The case of the Nuvolau Cassian platform (Dolomites - Italy). *Marine and Petroleum Geology, 138*, 1-24. doi:https://doi.org/10.1016/j.marpetgeo.2022.105574.

Meng, Q.-B., Wang, C.-K., Liu, J.-F., Zhang, M.-W., Lu, M.-M., & Wu, Y. (2020). Physical and micro-structural characteristics of limestone after high temperature exposure. *Bulletin of Engineering Geology and the Environment, 79*, 1259–1274. doi:https://doi.org/10.1007/s10064-019-01620-0

Mingyi, Z., Jianguo, L., Yuanming, L., & Xiyin, Z. (2018). Variation of the thermal conductivity of a silty clay during a freezing-thawing process. *International Journal of Heat and Mass Transfer, 124*, 1059-1067. doi:https://doi.org/10.1016/j.ijheatmasstransfer.2018.02.118

Mitchell, J. K. (1993). *Fundamentals of Soil Behavior.* Wiley, Hoboken. Retrieved April 2, 2024, from https://books.google.dk/books?id=aw_Gpm_SWJAC

Moormann, C., & Schneider, M. (2010). GeoTU6 – a Geothermal Research Project for Tunnels. *Tunnel*, 14-21.

Municipality of Trento. (2021, March 29). *La circonvallazione ferroviaria - Interramento*. Retrieved April 21, 2024, from https://www.comune.trento.it/Aree-tematiche/TrentoLab/Progetto-integrato/Domande-e-risposte/La-circonvallazione-ferroviaria-Interramento

Municipality of Trento. (2021). *Progetto integrato*. Retrieved April 21, 2024, from https://www.comune.trento.it/Aree-tematiche/TrentoLab/Progetto-integrato

Nayar, K. G., Sharqawy, M. H., Banchik, L. D., & Lienhard, J. H. (2016). Thermophysical properties of seawater: A review and new correlations that include pressure dependence. *Desalination, 390*, 1-24. doi:10.1016/j.desal.2016.02.024.

Nicholson, D., Chen, Q., de Silva, M., Winter, A., & Winterling , R. (2015). The design of thermal tunnel energy segments for Crossrail, UK. *Engineering Sustainability*, 118-134. doi:http://dx.doi.org/10.1680/ensu.13.00014

Nidal H., A.-H. (2003). Thermal Properties of Soils as affected by Density and Water Content. *Biosystems Engineering, 86*, 97-102. doi:https://doi.org/10.1016/S1537-5110(03)00112-0

Ogunleye, O., Singh, R. M., Cecinato, F., & Choi, J. C. (2020). Effect of intermittent operation on the thermal efficiency of energy tunnels under varying tunnel air temperature. *Renewable Energy*, 2646-2658. doi:https://doi.org/10.1016/j.renene.2019.08.088

Opreanu, G. (2003). Porosity density and other physical properties of deep-sea sediments from the black sea. *National Institute of Marine Geology and Geo-ecology*.

Ozcoban, M. &., Türkoğlu Demirkol, G., Celik, S., & Tufekci, N. (2018). Evaluation of clay soils' permeability: A comparative study between the natural, compacted, and consolidated clay soils. *Journal of Advances in Technology and Engineering Studies*, 184-191. doi:10.20474/jater-3.5.3

Parodi, V. (2018). *Salinità superficiale del mare Regione Liguria*. Retrieved October 3, 2024, from https://climadat.isprambiente.it/dati-e-indicatori/indicatori-di-impatto-dei-cambiamenti-climatici/salinita-superficiale-del-mare-liguria/

Pimienta, L., Klitzsch, N., & Clauser, C. (2018). Comparison of thermal and elastic properties of sandstones: Experiments and theoretical insights. *Geothermics, 76*, 60-73. doi:https://doi.org/10.1016/j.geothermics.2018.06.005.

Ponomaryov, A., & Zakharov, A. (2021). Investigations of Soil Body Temperature Fields. *Proceedings of EECE 2020* (pp. 13-22). Springer International Publishing. doi:https://doi.org/10.1007/978-3-030-72404-7_2

Preene, M., & Powrie, W. (2008). Ground energy systems: from analysis to geotechnical design. *Géotechnique*, 261-171.

Rao, S. E., Ray, L., Khan, T., & Ravi, G. (2022). Thermal conductivity, density and porosity of sedimentary and metamorphic rocks from the Lower and Higher Himalaya, Western Himalaya, India. *Geophysical Journal International, 231*. doi:10.1093/gji/ggac176

Rete Ferroviaria Italiana. (2021). *Progetto di fattibilita' tecnica ed economica - Lotto 3A Circonvallazione di Trento. Relazione geotecnica generale* .

Rete Ferroviaria Italiana. (2021). *Progetto di fattibilita' tecnica ed economica. Lotto 3A: Circonvallazione di Trento. Relazione geologica ed idrogeologica.* Ministero delle infrastrutture e dei trasporti.

Rete Ferroviaria Italiana. (2022). *Dibbatito Publico. Circonvallazione ferroviaria Trento. Relazione conclusiva.*

RFI S.p.a. Direzione investimenti Area Nord Est. (2022). *Parere n. 1 del 29 aprile 2022* . Ministero della Transizione Ecologica.

Robertson, E. C. (1988). *Thermal properties of rocks.* Reston, Virginia: United States Department of the Interior Geological Survey.

Roghi, G., Kustatscher, E., Bernardi, M., Dal Corso, J., Forte, G., Franz, M., . . . Gianolla, P. (2014). Field trip to Permo-Triassic Palaeobotanical and Palynological sites of the Southern Alps. *Geo-Alp*, 29-84.

Rosso, E., Insana, A., Vesipa, R., & Barla , M. (2021). Optimization of the hydraulic circuit for energy tunnels. *International Conference on Computational Methods and Information Models in Tunneling (EURO:TUN)*, (pp. 27-29). Bochum.

Rotta Loria, A. (2019). Performance-based Design of Energy Pile Foundations. *The Journal of the Deep Foundations Institute*, 94-107. doi:https://doi.org/10.1080/19375247.2018.1562600

Rotta Loria, A., Di Donna, A., & Zhang, M. (2022). Stresses and deformations induced by geothermal operations of energy tunnels. *Tunnelling and Underground Space Technology*, 1-15. doi:https://doi.org/10.1016/j.tust.2022.104438

Saltwork Consultores. (2024). *Skill Objective: Why reservoir characterization is more complicated in carbonates than in sandstones*. Retrieved from https://www.saltworkconsultants.com/carbonate-porosity-sandstone-vs-carbonate/

Shrestha, P. &. (2014). Groundwater Effect on Faulted Rock Mass: An Evaluation of Modi Khola Pressure Tunnel in the Nepal Himalaya. *Rock Mechanics and Rock Engineering, 47*. doi:10.1007/s00603-013-0467-7

Soussi, C., Fouché, O., Bracq, G., & Minec, S. (2016). Tunnels, a new potential for sensible heat storage in rock: 3D numerical modelling of a reversible exchanger within tunnel. *Comsol Conference Munich 2016.* Munich.

Spalding, B. D., & Taborek, J. (1983). *Heat Exchanger Design Handbook.* Hemisphere Publishing Corporation.

Tansel, B. (2023). Thermal properties of municipal solid waste components and their relative significance for heat retention, conduction, and thermal diffusion in landfills. *Journal of Environmental Management*, 1-10. doi:https://doi.org/10.1016/j.jenvman.2022.116651

Tinti, F., Boldini, D., Ferrari, M., Lanconelli, M., Kasmaee, S., Bruno, R., . . . Zurlo, R. (2017). Exploitation of geothermal energy using tunnel lining technology in a mountain environment. A feasibility study for the Brenner Base tunnel–BBT. *Tunnelling and Underground Space Technology*, 182-203. doi:http://dx.doi.org/10.1016/j.tust.2017.07.011

Vieira, A., Alberdi-Pagola, M., Barla, M., Christodoulides, P., Florides, G., Insana, A., . . . Salciarini, D. (2022). Site characterization for the design of thermoactive geostructures. *International Journal of Geotechnical and Geoenvironmental Engineering*, 1-15. doi:https://doi.org/10.28927/SR.2022.001022

Vieira, A., Alberdi-Pagola, M., Christodoulides, P., Javed, S., Loveridge, F., Nguyen, F., . . . Radioti, G. (2017). Characterisation of Ground Thermal and Thermo-Mechanical Behaviour for Shallow Geothermal Energy Applications. *Energies*, 1-51. doi:http://dx.doi.org/10.3390/en10122044

Vivas, C., Hu, Z., & Salehi, S. (2023). Texture-dependent thermal properties of sandstone rocks examined by scanning electron microscopy for thermal energy storage applications. *ASME Open Journal of Engineering, 2*.

Wisconsin Geological and Natural History Survey. (2024). *Understanding Porosity and Density*. Retrieved from https://home.wgnhs.wisc.edu/water/wisconsin-aquifers/understanding-porosity-density/

You, Z., Ma, Y., Wang, Z., & Ma, J. (2021). Tensile strength variation of a silty clay under different temperature and moisture conditions. *Cold Regions Science and Technology, 189*. doi:10.1016/j.coldregions.2021.103314

Zeng, G., Liu, L., Xue, Q., Wan, Y., Ma, J., & Zhao, Y. (2017). Experimental study of the porosity and permeability of municipal solid waste. *Environmental Progress & Sustainable Energy*, 1-6. doi:10.1002/ep.12632

Zhang, G., Caichu, X., Yang, Y., Sun, M., & Zou, Y. (2014). Experimental study on the thermal performance of tunnel lining ground heat exchangers. *Energy and Buildings*, 149-157. doi:http://dx.doi.org/10.1016/j.enbuild.2014.03.043

Appendix A

Table 26. Proposed homogeneous sections for the Trento ring road tunnel

Progressive distance [m]	Proposed homogeneous section	T [°C]	Lithology	Geothermal potential [MW]	
				Winter	Summer
0	1	13.75	PTG	0.02	0.02
25		13.75		0.02	0.02
50		13.75		0.02	0.02
75		13.75		0.02	0.02
100		13.75		0.02	0.02
125		13.75		0.02	0.02
150		13.75		0.02	0.02
175		13.75		0.02	0.02
200		13.75		0.02	0.02
225		13.75		0.02	0.02
250		13.75		0.02	0.02
275		13.75		0.02	0.02
300		13.75		0.02	0.02
325		13.75		0.02	0.02
350	2	13.75		0.02	0.02
375	3	13.75	ZW	0.02	0.02
400		13.75		0.02	0.02
425		13.75		0.02	0.02
450	4	13.75	TVZ	0.02	0.02
475		13.94		0.02	0.02
500	5	14.18	DPR	0.02	0.02
525		14.37		0.02	0.02
550		14.62		0.02	0.02
575		14.70		0.02	0.02
600		14.84		0.02	0.02
625		14.93		0.02	0.02
650	6	15.03		0.03	0.01
675		15.33		0.03	0.01
700		15.35		0.03	0.01

725		15.33		0.03	0.01
750		15.30		0.03	0.01
775		15.32		0.03	0.01
800		15.43		0.03	0.01
825		15.50		0.03	0.01
850		15.11		0.03	0.01
875	7	15.04	ZW	0.03	0.01
900		15.03		0.03	0.01
925		15.01		0.03	0.01
950		15.03		0.03	0.01
975		15.00		0.03	0.01
1000	5	14.99		0.02	0.01
1025		15.04		0.03	0.01
1050		15.04		0.03	0.01
1075		15.06		0.03	0.01
1100		15.02		0.03	0.01
1125		15.03		0.03	0.01
1150	6	15.06		0.03	0.01
1175		15.16		0.03	0.01
1200		15.17	TVZ	0.03	0.01
1225		15.25		0.03	0.01
1250		15.28		0.03	0.01
1275		15.00		0.03	0.01
1300		15.05		0.03	0.01
1325		14.98		0.02	0.01
1350		14.87		0.02	0.01
1375	5	14.84		0.02	0.01
1400		14.59		0.02	0.01
1425		14.39		0.02	0.01
1450		14.53		0.02	0.01
1475		14.39		0.02	0.01
1500		14.41		0.02	0.01
1525		14.49		0.02	0.01
1550	8	14.52	ZW	0.02	0.01
1575		14.49		0.02	0.01
1600		14.52		0.02	0.01
1625		14.51		0.02	0.01
1650		14.35		0.02	0.01
1675		14.49		0.02	0.01

1700		14.65		0.02	0.01
1725		14.83		0.02	0.01
1750		14.80		0.02	0.01
1775	3	14.74		0.02	0.02
1800	7	15.02		0.03	0.01
1825		15.64		0.03	0.01
1850		15.82		0.03	0.01
1875		15.61		0.03	0.01
1900		15.45		0.03	0.01
1925		15.51		0.03	0.01
1950	9	15.53		0.03	0.01
1975		15.52		0.03	0.01
2000		15.76		0.03	0.01
2025		15.82		0.03	0.01
2050		15.91		0.03	0.01
2075		15.98		0.03	0.01
2100		16.07		0.03	0.01
2125		16.13		0.03	0.01
2150		16.18		0.03	0.01
2175		16.16		0.03	0.01
2200		16.22		0.03	0.01
2225		16.28		0.03	0.01
2250		16.27	GIV3	0.03	0.01
2275		16.27		0.03	0.01
2300		16.28		0.03	0.01
2325	10	16.29		0.03	0.01
2350		16.38		0.03	0.01
2375		16.53		0.03	0.01
2400		16.72		0.03	0.01
2425		16.62		0.03	0.01
2450		16.71		0.03	0.01
2475		16.86		0.03	0.01
2500		16.86		0.03	0.01
2525		16.93		0.03	0.01
2550		17.06		0.03	0.01
2575		17.08		0.03	0.01
2600	11	17.11		0.03	0.01
2625		17.15		0.03	0.01
2650		17.22		0.03	0.01

2675		17.30		0.03	0.01
2700		17.53		0.03	0.01
2725		17.58		0.03	0.01
2750		17.65		0.03	0.01
2775		17.87		0.03	0.01
2800		17.82		0.03	0.01
2825		17.70		0.03	0.01
2850		17.55		0.03	0.01
2875		17.40		0.03	0.01
2900		17.22		0.03	0.01
2925		17.06		0.03	0.01
2950		16.84		0.03	0.01
2975		16.69		0.03	0.01
3000	10	16.54		0.03	0.01
3025		16.38		0.03	0.01
3050		16.23		0.03	0.01
3075		16.12		0.03	0.01
3100	12	16.03		0.03	0.01
3125		15.84		0.03	0.01
3150		15.76		0.03	0.01
3175		15.74		0.03	0.01
3200	13	15.76		0.03	0.01
3225		15.76		0.03	0.01
3250		15.77		0.03	0.01
3275		15.94		0.03	0.01
3300		16.04		0.03	0.01
3325		16.11		0.03	0.01
3350		16.23	WER	0.03	0.01
3375	12	16.42		0.03	0.01
3400		16.64		0.03	0.01
3425		16.87		0.03	0.01
3450		16.99		0.03	0.01
3475	14	17.04		0.03	0.01
3500		16.95		0.03	0.01
3525		16.89		0.03	0.01
3550	12	16.80		0.03	0.01
3575		16.64		0.03	0.01
3600		16.52		0.03	0.01
3625		16.38		0.03	0.01

3650		16.25		0.03	0.01
3675		16.36		0.03	0.01
3700		16.44		0.03	0.01
3725		16.56		0.03	0.01
3750		16.66		0.03	0.01
3775	15	16.66		0.03	0.01
3800		16.63	ZW	0.03	0.01
3825		16.64		0.03	0.01
3850		16.72		0.03	0.01
3875		16.89		0.03	0.01
3900	16	17.08		0.03	0.01
3925	14	17.24		0.03	0.01
3950		17.46		0.03	0.01
3975	13	15.93		0.03	0.01
4000		17.65		0.03	0.01
4025		17.76		0.03	0.01
4050	14	17.81		0.03	0.01
4075		17.86		0.03	0.01
4100		17.97		0.03	0.01
4125	17	18.02		0.03	0.00
4150		18.01		0.03	0.00
4175		17.98		0.03	0.01
4200		17.93		0.03	0.01
4225		17.86		0.03	0.01
4250		17.73		0.03	0.01
4275		17.54	WER	0.03	0.01
4300		17.34		0.03	0.01
4325		17.21		0.03	0.01
4350		17.18		0.03	0.01
4375	14	17.14		0.03	0.01
4400		17.20		0.03	0.01
4425		17.21		0.03	0.01
4450		17.21		0.03	0.01
4475		17.21		0.03	0.01
4500		17.21		0.03	0.01
4525		17.35		0.03	0.01
4550		17.52		0.03	0.01
4575		17.69		0.03	0.01
4600		17.87		0.03	0.01

4625	17	18.15		0.03	0.00
4650		18.51		0.03	0.00
4675	18	19.07		0.04	0.00
4700		19.48		0.04	0.00
4725		19.66		0.04	0.00
4750		19.75		0.04	0.00
4775		19.85		0.04	0.00
4800		19.90		0.04	0.00
4825		19.81		0.04	0.00
4850		19.57		0.04	0.00
4875		19.45		0.04	0.00
4900		19.05		0.04	0.00
4925	17	18.44		0.03	0.00
4950		18.20		0.03	0.00
4975		18.17		0.03	0.00
5000		18.13		0.03	0.00
5025		18.13		0.03	0.00
5050		18.08		0.03	0.00
5075		18.01		0.03	0.00
5100	14	17.77		0.03	0.01
5125		17.41		0.03	0.01
5150		17.12		0.03	0.01
5175		17.00		0.03	0.01
5200	12	16.86		0.03	0.01
5225		16.70		0.03	0.01
5250		16.51		0.03	0.01
5275		16.41		0.03	0.01
5300		16.26		0.03	0.01
5325		16.12		0.03	0.01
5350	13	15.95		0.03	0.01
5375		15.95		0.03	0.01
5400		15.87		0.03	0.01
5425		15.66		0.03	0.01
5450		15.71		0.03	0.01
5475		15.92		0.03	0.01
5500		15.83		0.03	0.01
5525		15.80		0.03	0.01
5550		15.65		0.03	0.01
5575		15.77		0.03	0.01

5600		15.75		0.03	0.01
5625		15.67		0.03	0.01
5650		15.75		0.03	0.01
5675		15.81		0.03	0.01
5700		15.97		0.03	0.01
5725		16.00		0.03	0.01
5750		16.02		0.03	0.01
5775		16.07		0.03	0.01
5800		16.23		0.03	0.01
5825		16.25		0.03	0.01
5850		16.10		0.03	0.01
5875		16.23		0.03	0.01
5900		16.35		0.03	0.01
5925		16.43		0.03	0.01
5950	12	16.36	BEL	0.03	0.01
5975		16.52		0.03	0.01
6000		16.47		0.03	0.01
6025		16.64		0.03	0.01
6050		16.58		0.03	0.01
6075		16.44		0.03	0.01
6100		16.42		0.03	0.01
6125		16.56		0.03	0.01
6150		16.17		0.03	0.01
6175		16.07		0.03	0.01
6200	13	15.90		0.03	0.01
6225	12	16.07		0.03	0.01
6250		16.08		0.03	0.01
6275		16.21		0.03	0.01
6300		16.20		0.03	0.01
6325		16.33		0.03	0.01
6350		16.35		0.03	0.01
6375		16.36		0.03	0.01
6400	19	16.35	GAR	0.03	0.01
6425		16.25		0.03	0.01
6450		16.29		0.03	0.01
6475		16.33		0.03	0.01
6500		16.40		0.03	0.01
6525		16.46		0.03	0.01
6550		16.53		0.03	0.01

6575		16.59		0.03	0.01
6600		16.65		0.03	0.01
6625		16.79		0.03	0.01
6650		16.89		0.03	0.01
6675		16.93		0.03	0.01
6700		16.90		0.03	0.01
6725		16.78		0.03	0.01
6750		16.75		0.03	0.01
6775		16.71		0.03	0.01
6800		16.68		0.03	0.01
6825		16.67		0.03	0.01
6850		16.66		0.03	0.01
6875		16.52		0.03	0.01
6900		16.46		0.03	0.01
6925	20	15.87		0.03	0.01
6950		16.14		0.03	0.01
6975		16.28		0.03	0.01
7000	19	16.25		0.03	0.01
7025		16.28		0.03	0.01
7050		16.20		0.03	0.01
7075		16.14		0.03	0.01
7100		16.11		0.03	0.01
7125		16.06		0.03	0.01
7150		16.08		0.03	0.01
7175		16.09		0.03	0.01
7200	21	16.08	ICTc	0.03	0.01
7225		16.08		0.03	0.01
7250		16.08		0.03	0.01
7275		16.07		0.03	0.01
7300		16.05		0.03	0.01
7325		16.05		0.03	0.01
7350		15.99		0.03	0.01
7375		15.82		0.03	0.01
7400	22	15.99		0.03	0.01
7425		15.99	ICT	0.03	0.01
7450		15.60		0.03	0.01
7475		15.27		0.03	0.01
7500	23	14.91		0.02	0.01
7525		14.80		0.02	0.01

7550		14.62		0.02	0.01
7575	24	14.74		0.02	0.01
7600	25	15.10	LUB	0.03	0.01
7625		15.22		0.03	0.01
7650	26	15.40		0.03	0.01
7675		15.62		0.03	0.01
7700		15.84		0.03	0.01
7725		15.97		0.03	0.01
7750	27	16.21		0.03	0.01
7775		16.59		0.03	0.01
7800		16.71		0.03	0.01
7825		16.80		0.03	0.01
7850		16.90		0.03	0.01
7875		16.88		0.03	0.01
7900		16.79		0.03	0.01
7925		16.76		0.03	0.01
7950		16.75		0.03	0.01
7975		16.70		0.03	0.01
8000		16.67		0.03	0.01
8025		16.56	VFS	0.03	0.01
8050		16.55		0.03	0.01
8075		16.60		0.03	0.01
8100		16.61		0.03	0.01
8125		16.78		0.03	0.01
8150		16.63		0.03	0.01
8175		16.49		0.03	0.01
8200		16.38		0.03	0.01
8225		16.56		0.03	0.01
8250		16.49		0.03	0.01
8275		16.28		0.03	0.01
8300		16.32		0.03	0.01
8325		16.35		0.03	0.01
8350		16.37		0.03	0.01
8375		16.39		0.03	0.01
8400		16.43		0.03	0.01
8425		16.46		0.03	0.01
8450	19	16.48	GAR	0.03	0.01
8475		16.46		0.03	0.01
8500		16.45		0.03	0.01

8525		16.63		0.03	0.01
8550	12	16.30	BEL	0.03	0.01
8575		16.11		0.03	0.01
8600		16.12	WER	0.03	0.01
8625		16.13		0.03	0.01
8650		16.11		0.03	0.01
8675	13	15.97		0.03	0.01
8700	28	15.92	ARV	0.03	0.01
8725		15.87		0.03	0.01
8750		15.77		0.03	0.01
8775		15.65		0.03	0.01
8800		15.55		0.03	0.01
8825		15.35		0.03	0.01
8850		15.04		0.03	0.01
8875	29	14.29		0.02	0.01
8900		14.33		0.02	0.01
8925		14.94		0.02	0.01
8950	28	15.25		0.03	0.01
8975		15.32		0.03	0.01
9000		15.30		0.03	0.01
9025		15.26		0.03	0.01
9050		15.67		0.03	0.01
9075		15.28		0.03	0.01
9100		15.54		0.03	0.01
9125		15.41		0.03	0.01
9150		15.77		0.03	0.01
9175		15.43		0.03	0.01
9200		15.83		0.03	0.01
9225		15.54		0.03	0.01
9250		15.57		0.03	0.01
9275		15.55		0.03	0.01
9300		15.39		0.03	0.01
9325		15.60		0.03	0.01
9350		15.38		0.03	0.01
9375		15.76		0.03	0.01
9400	7	15.99	RTZ	0.03	0.01
9425	15	16.12		0.03	0.01
9450		16.11		0.03	0.01
9475		16.48		0.03	0.01

9500		16.14		0.03	0.01
9525		16.05		0.03	0.01
9550	7	15.97		0.03	0.01
9575	15	16.09		0.03	0.01
9600	7	15.96		0.03	0.01
9625	15	16.24		0.03	0.01
9650	15	16.07		0.03	0.01
9675		15.81		0.03	0.01
9700		15.77		0.03	0.01
9725		15.71		0.03	0.01
9750		15.83		0.03	0.01
9775		15.56		0.03	0.01
9800		15.60		0.03	0.01
9825		15.31		0.03	0.01
9850	7	15.75		0.03	0.01
9875		15.81		0.03	0.01
9900		15.70		0.03	0.01
9925		15.59		0.03	0.01
9950		15.42		0.03	0.01
9975		15.32		0.03	0.01
10000		15.36		0.03	0.01
10025		15.54		0.03	0.01
10050		15.37		0.03	0.01
10075		15.27		0.03	0.01
10100	28	15.28		0.03	0.01
10125		15.28		0.03	0.01
10150		15.10		0.03	0.01
10175		15.07		0.03	0.01
10200		14.78	ARV	0.02	0.01
10225		14.67		0.02	0.01
10250	29	14.53		0.02	0.01
10275		14.39		0.02	0.01
10300		14.31		0.02	0.01
10325		14.09		0.02	0.01
10350	30	13.95		0.02	0.02
10375		13.80		0.02	0.02
10400		13.80		0.02	0.02
10425	3	13.79	SAA	0.02	0.02
10450		13.82		0.02	0.02

10475		13.83		0.02	0.02
10500		13.85		0.02	0.02
10525		13.75		0.02	0.02
10550		13.75		0.02	0.02
10575		13.75		0.02	0.02
10600		13.75	CHI	0.02	0.02
10625		13.75		0.02	0.02
10650		13.75		0.02	0.02
			Total =	12.03	3.80

Table 27. Proposed homogeneous sections for the Cortina d'Ampezzo tunnel

Progressive distance [m]	Proposed homogeneous section	T [°C]	Lithology	Geothermal potential [MW]	
				Winter	Summer
550	1	8.00	Fine-grained silty clayey materials	0.02	0.07
600		8.00		0.02	0.07
650		8.00		0.02	0.07
700		8.00		0.02	0.07
750		8.00		0.02	0.07
800		8.00		0.02	0.07
850	2	8.00	Coarse-grained materials (gravels, pebbles)	0.02	0.07
900	3	9.37	Plastic clays with inclusions of dolomitic pebbles and cobbles	0.03	0.06
950		9.76		0.03	0.06
1000	4	10.15		0.03	0.05
1050		10.47		0.03	0.05
1100		10.70		0.03	0.05
1150	5	11.07		0.04	0.05
1200		11.43		0.04	0.05
1250		11.87		0.04	0.05
1300	6	12.19		0.04	0.04
1350		12.65		0.04	0.04

1400	7	13.07		0.05	0.04
1450		13.49		0.05	0.04
1500		13.71		0.05	0.04
1550		13.86		0.05	0.04
1600	8	14.05		0.06	0.03
1650		14.29		0.06	0.03
1700		14.50		0.06	0.03
1750		14.63		0.06	0.03
1800		14.85		0.06	0.03
1850	7	13.77		0.05	0.04
1900		13.66		0.05	0.04
1950		13.58		0.05	0.04
2000		13.50		0.05	0.04
2050		13.39		0.05	0.04
2100		13.30		0.05	0.04
2150		13.31		0.05	0.04
2200		13.35		0.05	0.04
2250		13.39		0.05	0.04
2300		13.64		0.05	0.04
2350		13.65		0.05	0.04
2400		13.38		0.05	0.04
2450		13.27		0.05	0.04
2500		13.25		0.05	0.04
2550		13.44		0.05	0.04
2600		13.51		0.05	0.04
2650		13.33		0.05	0.04
2700		13.22		0.05	0.04
2750		13.32		0.05	0.04
2800		13.30		0.05	0.04
2850		13.25		0.05	0.04
2900		13.22		0.05	0.04
2950		13.14		0.05	0.04
3000	6	12.97		0.04	0.04
3050		12.95		0.04	0.04
3100		12.87		0.04	0.04
3150		12.93		0.04	0.04
3200	7	13.03		0.05	0.04
3250		13.19		0.05	0.04
3300		13.20		0.05	0.04

3350		13.21		0.05	0.04
3400		13.18		0.05	0.04
3450		13.13		0.05	0.04
3500		13.05		0.05	0.04
3550	6	13.00		0.04	0.04
3600	7	13.01		0.05	0.04
3650		12.08		0.04	0.04
3700		12.29		0.04	0.04
3750		12.42		0.04	0.04
3800	6	12.44		0.04	0.04
3850		12.42		0.04	0.04
3900		12.49		0.04	0.04
3950		12.51		0.04	0.04
4000		12.44		0.04	0.04
4050	5	11.95		0.04	0.05
4100		11.91		0.04	0.05
4150		11.86		0.04	0.05
4200		11.82		0.04	0.05
4250		11.66		0.04	0.05
4300		11.73		0.04	0.05
4350		11.68		0.04	0.05
4400	9	11.62		0.04	0.05
4450		11.56		0.04	0.05
4500		11.50		0.04	0.05
4550		11.57		0.04	0.05
4600		11.68	Shales,	0.04	0.05
4650		11.87	sandstones, and	0.04	0.05
4700		11.72	carbonates	0.04	0.05
4750		11.16		0.04	0.05
4800		10.86		0.03	0.05
4850	10	10.63		0.03	0.05
4900		10.41		0.03	0.05
4950		10.02		0.03	0.05
5000	11	9.70		0.03	0.06
5050		9.37		0.03	0.06
5100		8.58		0.02	0.07
5150	12	8.21		0.02	0.07
5200		8.00		0.02	0.07

5250	2	8.00	Coarse-grained materials (gravels, pebbles)	0.02	0.07
				3.91	4.29

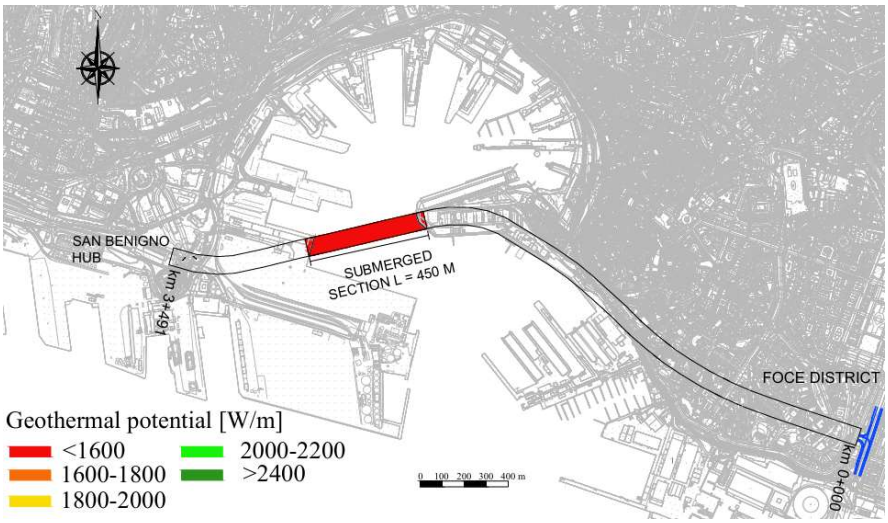

Figure 81. Estimated geothermal potential per meter in winter for condition A – Subport Tunnel of Genova

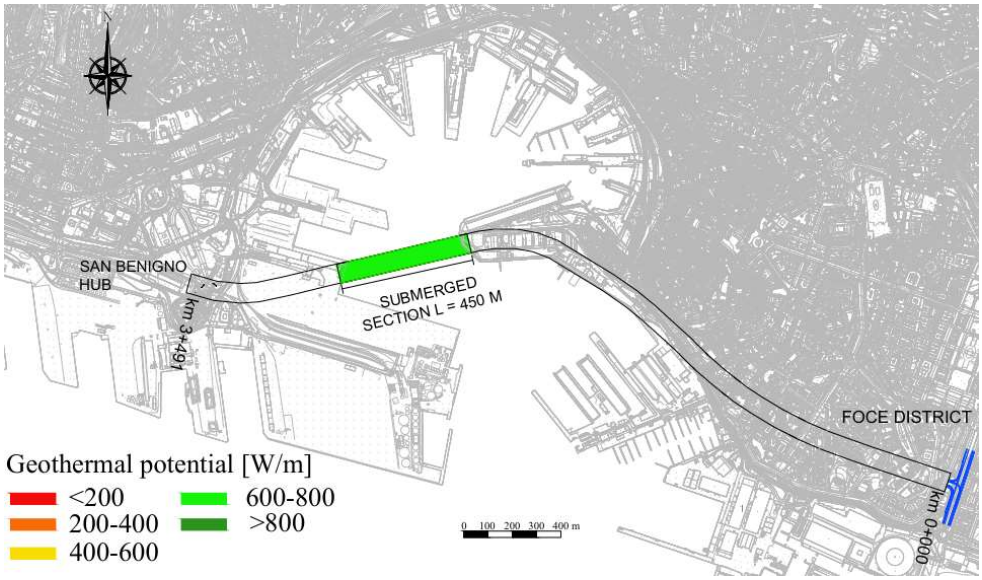

Figure 82. Estimated geothermal potential per meter in summer for condition A – Subport Tunnel of Genova

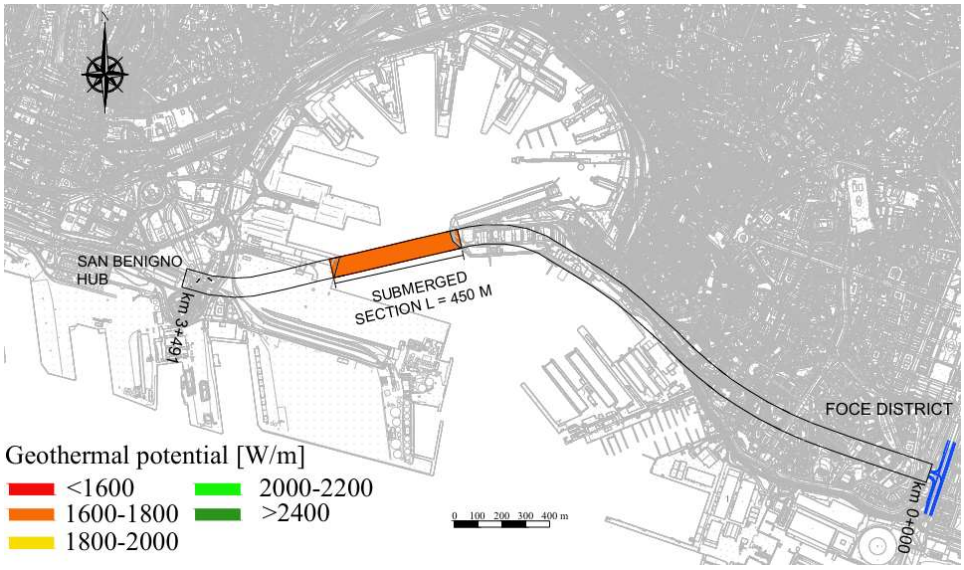

Figure 83. Estimated geothermal potential per meter in winter for condition B.1 and B.2 – Subport Tunnel of Genova

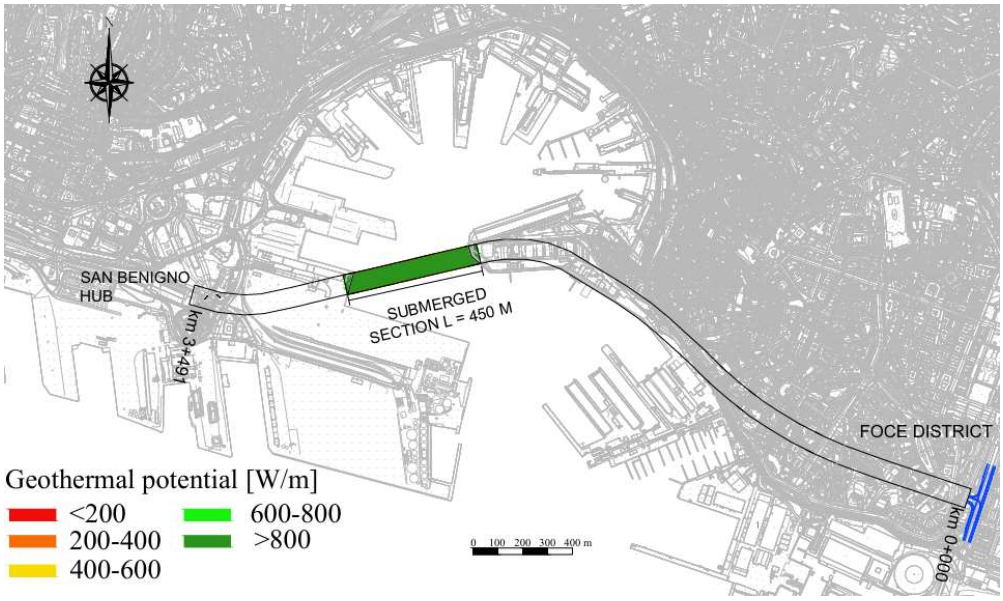

Figure 84. Estimated geothermal potential per meter in summer for condition B.1 and B.2 – Subport Tunnel of Genova